Dissertation

submitted to the

Combined Faculty of Mathematics, Engineering and Natural Sciences

of Heidelberg University, Germany

for the degree of

Doctor of Natural Sciences

Put forward by

M.Sc. Margareta Metzner

born in: Leonberg, Germany

Oral examination: December 9th, 2025

As amended on September 19, 2025

Typeset: PDF-LaTeX 2$_\varepsilon$

Detection, quantification and 3D localization of anatomical changes with a helium-beam radiography system based on thin pixelated detectors

Referees: Prof. Dr. Mark E. Ladd,
Prof. Dr. Oliver Jäkel

The work presented in this thesis is original to the author, except where otherwise indicated, referenced or acknowledged.

Abstract

The clinical use of ion beams facilitates highly precise treatments of patients suffering from cancer. Utilizing the sharp peak in the depth-dose curve of protons and heavier ions, ion-beam radiotherapy treatments exhibit particularly localized dose distributions compared to conventional modalities. However, they are sensitive to changes such as variations in the patient's anatomy which can occur over the treatment course of typically several weeks. These changes could be assessed prior to each treatment fraction by employing the ion beam itself to generate an image of the patient's anatomy from beam's eye view. Despite extensive efforts over the past decades, no ion-beam radiography system is routinely used in clinics yet.

Most ion-imaging prototypes require devices with a large material budget. In order to increase the practicability and foster clinical acceptance, a compact detection system was built from thin silicon pixel detectors. However, the system's ability to precisely measure the clinically relevant quantity for heterogeneous objects is limited.

This thesis experimentally investigates the energy-painting approach eliminating this remaining principal limitation of the detection system based on thin detectors. Energy painting subsequently allows for the acquisition of a helium-beam radiograph of an anthropomorphic phantom, which is evaluated regarding its accuracy and compared to clinically used CT modalities based on X-rays. To extract the position of phantom modifications along the beam direction from single ion-beam projections, the 2.5D imaging method is investigated in simulations and experiments. Overall, the system's capability to detect, quantify, and localize anatomical changes with high spatial resolution is demonstrated.

Consequently, this thesis presents fundamental contributions towards a future clinical application of the compact helium-beam radiography system for low-dose verification of the patient's anatomy prior to ion-beam radiotherapy treatments.

Zusammenfassung

Die klinische Anwendung von Ionenstrahlen ermöglicht eine hochpräzise Behandlung von Krebspatienten. Durch die Nutzung des scharfen Peaks in der Tiefendosiskurve von Protonen und schwereren Ionen weisen Ionenstrahl-Therapien im Vergleich zu herkömmlichen Verfahren eine besonders lokalisierte Dosisverteilung auf. Allerdings sind diese auch anfällig für Veränderungen, z. B. der Patientenanatomie, welche im Laufe der üblicherweise über Wochen andauernden Behandlung auftreten können. Diese Veränderungen könnten vor jeder Behandlungsfraktion beurteilt werden, indem der Ionenstrahl selbst verwendet wird, um ein Bild der Patientenanatomie aus der Perspektive des Strahls zu erzeugen. Trotz umfangreicher Bemühungen in den letzten Jahrzehnten wird aktuell jedoch noch kein Ionenstrahl-Radiografiesystem routinemäßig in Kliniken eingesetzt.

Die meisten Prototypen für die Ionenbildgebung erfordern Geräte mit hohem Materialaufwand. Um die Praktikabilität zu erhöhen und die klinische Akzeptanz zu fördern, wurde ein kompaktes Detektionssystem aus dünnen Silizium-Pixeldetektoren gebaut. Die Fähigkeit des Systems, die klinisch relevante Größe für heterogene Objekte präzise zu messen, ist jedoch begrenzt.

Diese Arbeit untersucht den Energy-Painting-Ansatz experimentell, durch welchen diese verbleibende wesentliche Einschränkung des auf dünnen Detektoren basierenden Detektionssystems behoben wird. Energy-Painting ermöglicht anschließend die Aufnahme einer Heliumstrahl-Radiografie eines anthropomorphen Phantoms, die hinsichtlich ihrer Genauigkeit bewertet und mit klinisch verwendeter Röntgen-CT-Bildgebung verglichen wird. Um die Position von Phantomveränderungen entlang der Strahlrichtung aus einzelnen Ionenstrahlprojektionen zu extrahieren, wird die 2,5D-Bildgebungsmethode in Simulationen und Experimenten untersucht. Insgesamt wird die Fähigkeit des Systems demonstriert, anatomische Veränderungen mit hoher räumlicher Auflösung zu erkennen, zu quantifizieren und zu lokalisieren.

Folglich leistet diese Arbeit einen grundlegenden Beitrag zur zukünftigen klinischen Anwendung des kompakten Heliumstrahl-Radiografiesystems zur Niedrigdosis-Verifizierung der Patientenanatomie vor Ionenstrahl-Therapie-Behandlungen.

Contents

1 Introduction

1.1 Motivation

Multiple therapeutic strategies are employed in the treatment of cancer, with external radiation therapy being one of the principal approaches (Mee et al. 2023). This treatment modality is indicated for around 50% of the patients suffering from cancer (Delaney et al. 2005, Rosenblatt et al. 2018, Laskar et al. 2022), often in combination with other approaches (Mee et al. 2023).

To irradiate cancer cells with ionizing radiation, as the standard of care, photons are used. The radiation dose deposited by photons in the tissue decreases exponentially over depth, which is why these treatments also leave a significant dose in the surrounding healthy tissue. Therefore, historically also other particles have been investigated for specific tumor types and sites (Trump et al. 1953, Griffin 1992, Castro 1994). Over the past several decades, predominantly protons and carbon ions have been used for ion-beam radiotherapy. More recently, helium ions have entered clinical use (Tessonnier et al. 2023).

The potential use of proton beams for radiotherapy has already been identified in the 1940s by Wilson (1946), a finding that also applies to other ion species. Due to their specific way of interaction with matter, ions[1] deposit most of their energy at a certain depth, shortly before they stop. The depth at which this dose peak – the so-called Bragg peak (Bragg and Kleeman 1905) – occurs, can be influenced by the particle's initial beam energy and thus be intentionally placed inside of the tumor volume. By combining beams with several initial beam energies, the whole tumor can be covered and highly focused dose distributions can be created (Schulz-Ertner and Tsujii 2007, Palm and Johansson 2007, Schardt et al. 2010, Van De Water et al. 2011, Durante and Debus 2018). Due to the reduced dose in healthy tissue, treatments with ion beams promise to cause less mild-moderate acute toxicity (Leeman et al. 2017) and lower incidence of secondary tumors (Paganetti et al. 2012).

---

[1] Throughout this whole thesis the term ion also includes protons.

In clinics, the focused dose distributions are tailored to the individual anatomy and tumor geometry of each patient. To precisely plan these treatments, X-ray CTs are acquired prior to treatment in order to obtain a 3D map of the patient's tissue (Dobbs et al. 1983, Wohlfahrt and Richter 2020). The treatment plan is usually delivered in around 30 fractions over the course of several weeks. However, if the patient's anatomy changes over time, the highly focused dose distributions may shift within the patient compared to the planning situation, resulting in a reduced dose to the tumor and a higher dose in the healthy tissue. Thus, these highly precise treatments also require a high accuracy in the treatment delivery (Paganetti 2012). While uncertainties connected to the beam production – e.g., the energy spread of the beam – are well-controlled, the patient's anatomy is probably the most significant source for uncertainties in today's ion-beam radiotherapy treatments (Lomax 2020).

A variety of imaging techniques have been or are currently being developed in order to ensure accurate dose delivery over all treatment fractions. Among them are mainly X-ray- or MR-based modalities, but also techniques based on secondary radiation e.g., prompt gamma or iono-acoustic imaging (Lane et al. 2023).
Another interesting idea for daily monitoring of the patients' anatomy is the use of the ion-beam itself for that purpose (Koehler 1968, Poludniowski et al. 2015, Gianoli et al. 2024). Accordingly, higher initial beam energies must be used such that the beam can traverse the whole patient and can be detected on the other side. Due to the higher energy, the imaging beam experiences different interactions with the target material which can, however, be related to those of the treatment beam: if quantities are reported relative to the corresponding ones in water, the energy dependence becomes negligible (Parodi 2024). Therefore, ion-beam radiographs are usually expressed quantitatively in terms of water-equivalent thickness (WET), based on which direct conclusions can be drawn for the treatment beam. Contrary to X-ray or MR imaging, no conversion from photon or nuclear spin interactions to ion-related quantities is required.

Due to their low dose, ion-beam radiographs could be potentially taken on a daily basis directly before treatment. Once the patient is positioned for the treatment, an ion-beam radiograph from beam's eye view could be acquired and compared with previous fractions or the WET-map determined based on the planning CT. Positioning verification of the patient could be conducted based on these images as well as a monitoring of the patient's anatomy (Schneider and Pedroni 1995, Hammi et al. 2018). In that way, anatomical changes could be detected before each treatment fraction without a disadvantage in terms of dose compared to the standard positioning with X-ray images (Schulte et al. 2005, Schneider and Pedroni 1995, Depauw and Seco 2011, Arbor et al. 2015, Meyer et al. 2019, Miller et al. 2019).

1.2 Research gap and aim of the thesis

Several ion-imaging prototypes have been developed during the last decades (Gianoli et al. 2024). By now, a first proton imaging system can be purchased commercially from ProtonVDA (DeJongh et al. 2021) and a first clinical study was conducted to image patients with a multi-layer ionization chamber (Meijers et al. 2021). Despite these efforts, ion imaging is not yet used in clinical routine. Reasons for this include the relatively high doses of around 1 cGy in the first clinical study (Meijers et al. 2021) and the limited spatial resolution of systems which can operate at high beam intensities (Gianoli et al. 2024).
Another reason for this could be the complicated integration of the systems into a clinical workflow (Johnson 2024), e.g., due to their large physical dimensions. To infer the clinically relevant quantity WET, most systems measure residual energy or range of the ions (Poludniowski et al. 2015). By definition, these detectors must decelerate the ions until they stop, which requires a considerable amount of material. Therefore, they involve a rather big apparatus.

In contrast to that, the approach of our research group is to develop a lightweight and compact detection system based on thin pixelated detectors (Gehrke et al. 2018b, Amato et al. 2020). These detectors measure the energy deposited by single ions within the 300 µm thin sensitive layer. Thus, the measurement principle of these detectors can be seen as a probing of the steep rising edge of the imaging ions' Bragg peak. Furthermore, the same detectors are used to track the ions up- and downstream of the imaged object. Based on this, the scattering of the ions can be corrected for.
Using this compact system might increase practicability and foster acceptance to integrate the imager into the clinical workflow. Furthermore, the patients' comfort between physically smaller detection units might be higher.

Before I started my PhD project, the detection system based on thin detectors developed in our group had been proven to be functional. The characteristics of the images were found to be satisfactory for clinical use (Gehrke et al. 2018b, Amato et al. 2020) and even the feasibility of quantitative imaging in terms of WET was demonstrated (Knobloch et al. 2022). Furthermore, the system had been tested for several ion types, revealing helium ions to be suited best. However, only simple geometric objects had been imaged so far due to a limited range within which the clinically required WET precision could be achieved.

My task was to develop the system towards the foreseen clinical application of daily monitoring of the patient's anatomy. **Thus, the main focus of the work was to enable detection, quantification and localization of changes in anthropomorphic phantoms**

with the system based on thin detectors. Achieving this goal necessitated three key steps:

- The measurement principle, the probing of the Bragg peak, relies on steep gradients of the dose-depth curve for high precision WET measurements. Therefore, the WET range within which a clinically sufficient precision can be achieved is limited. This fundamental constraint, which inherently hinders the clinical application of the system, must be addressed first.
- Secondly, the WET accuracy in anthropomorphic phantoms must be benchmarked against clinical imaging modalities.
- Lastly, the system's capability of detecting and localizing anatomical changes must be assessed.

1.3 Thesis structure

Following this introduction, the second chapter explains the theoretical fundamentals which were important for the work presented in this thesis. It mainly involves the physics of ion beams and their interactions with matter, their detection by means of semiconducting detectors and their use for ion-beam radiotherapy and ion imaging. The third chapter presents the material and methods, which were required for the experimental setup, conduction of experiments, data analysis, image reconstruction and assessment procedures. The fourth chapter shows the results obtained during my PhD. First, one small project is presented which concerns the investigation of large-angle scattering events, their effect on the images, and the developed methods to filter them. Subsequently, the main results, which directly contribute to achieving the research aim of the thesis listed in section 1.2 above, are presented. They focus on the following:

- Energy painting method to bypass limited high-precision WET range of detector
- Imaging of an anthropomorphic phantom and comparison of the achieved WET accuracy to the one of clinically used X-ray modalities
- 2.5D imaging method to test the system's capability to detect anatomical changes and localize them along all three spatial dimensions

The fifth chapter discusses the results of chapter four and puts them into perspective with other published work. In chapter six, conclusions will be drawn and an outlook will be provided in the final chapter seven.

1.4 Novelty and credit statement

Naturally, this PhD thesis builds upon the research previously conducted in the group. Furthermore, I collaborated with other researchers on many tasks. Thus, in this section my original contribution to the content presented in this thesis will be delineated.

First, I want to disclose that I conducted a Master's thesis (Metzner 2022) on a preceding project in the helium-beam radiography research group prior to my PhD. During the work for my Master's thesis, I primarily examined the establishment of calibration curves and compared their ion-wise and pixel-wise application. I introduced the energy painting idea theoretically and tested it experimentally for a single radiograph of an anthropomorphic phantom. Consequently, the work of my PhD builds upon that prior work which results in minor overlaps in some parts of the methodology.

In particular, I want to emphasize that I carried out all experiments underlying the results of this thesis during the course of my PhD studies. Furthermore, in my PhD project I advanced the existing methodological framework, including the thorough methodological assessment of the energy painting algorithm with a dedicated study. Furthermore, I assessed the WET accuracy in anthropomorphic phantoms using a reference data set and clinical computed tomography (CT) scans obtained especially for this purpose in collaboration with external research partners. Moreover, I worked on Monte-Carlo simulations and experiments for the 2.5D imaging project, which enabled the 3D localization of anatomical changes.

Throughout my PhD, collaboration with other researchers played a central role. Furthermore, the results obtained throughout my PhD were summarized in publications. In the following, I will point out which chapters are based on a publication, while clearly distinguishing my own contributions from those of my collaborators.

Sections 3.7, 4.1 and 5.1 are based upon Metzner et al. (2024a), which I presented at IEEE NSS MIC RTSD in Tampa, USA as first author. The data, which the presentation at the conference was based upon, was acquired by Carlo Amato. The corresponding chapter in this thesis presents data which I personally collected through dedicated experiments. I repeated and expanded the analysis with this new data for the respective results presented in this thesis. In the whole process, I was responsible for the methodology, writing of code, data evaluation, visualization and the writing of the conference contribution. Annika Schlechter contributed by writing post-processing code. Oliver Jäkel, Mária Martišíková and Tim Gehrke were responsible for conceptualization, funding acquisition, resources and supervision. All authors reviewed the conference contribution.

Sections 3.8, 4.2 and 5.2 are based on the publication (Metzner et al. 2024b). As a first author, I was responsible for the project administration, design of the study, methodology, conduction of the experiments, software, the data analysis, visualization, and writing of the manuscript. Daria Zhevachevska, Annika Schlechter, Florian Kehrein and Stephan Brons contributed to the experiments. Statistical consultation and derivation of the analytical formulas were provided by Julian Schlecker. Carlos Murillo was responsible for the electronics of the experiments. Oliver Jäkel was responsible for funding acquisition, resources and supervision. Mária Martišíková and Tim Gehrke contributed to the conceptualization, project administration, validation, resources and supervision. All authors proofread and edited the manuscript.

Sections 3.9, 4.3 and 5.3 are based on the publication (Metzner et al. 2025a). As first author, I was responsible for the project administration, design of the study, methodology, the conduction of the helium-beam radiography experiments, software, the data analysis for all imaging modalities, visualization and writing of the manuscript. The CT data was acquired by the colleagues at the Heidelberg Ion-beam therapy center (Friderike K. Longarino, Benjamin Ackermann), the ground truth data set was obtained from colleagues at OncoRay, Dresden (Patrick Wohlfahrt, Christian Richter). Annika Schlechter, Maike Saphörster, Yanting Xu and Stephan Brons helped with the helium-beam radiography experiments. Julian Schlecker helped with the handling of the phantom and provided statistical guidance. Jürgen Debus and Oliver Jäkel were responsible for funding acquisition, resources and supervision. Mária Martišíková contributed to conceptualization, project administration, resources and supervision. Tim Gehrke provided conceptualization, project administration, methodology, validation, resources and supervision. All authors reviewed the manuscript.

The foundation of section 3.10 (apart from section 3.10.1), sections 4.4.4 and 5.4.2 was established in the Master's thesis of Annika Schlechter (Schlechter 2024), who conducted experiments, established methodology, wrote software, analyzed and investigated the collected data and conceptualized the visualization of the data. I co-supervised her, in the scope of which I conducted all experiments together with her and contributed to the methodology and data analysis. After I completely took over the project, I conducted additional required experiments and expanded the methodology of the post-processing and visualization of the data, contributed to the software and was responsible for the project administration and validation of the results. I then summarized the study in a publication (Metzner et al. 2025b), the first authorship of which I share with Annika Schlechter. Daria Zhevachevska contributed with software and helped with the experiments. Patrice Schlegel contributed to the methodology and validation. Oliver Jäkel was responsible for funding acquisition, resources and supervision. Mária Martišíková and Tim Gehrke provided conceptualization, project administration, methodology, validation, resources and supervision. All authors reviewed the manuscript.

The simulations presented in sections 3.10.1, 4.4.1 to 4.4.3 and 5.4.1 are not part of a publication. I was responsible for the simulation design, conducting the simulations, and the data analysis. The simulations are based on previous work by Maike Hermle (Hermle 2025), for which I served as one of the supervisors.

This PhD thesis was supervised by Dr. Tim Gehrke, Dr. Mária Martišíková and Prof. Dr. Oliver Jäkel who also conceptualized the project idea, performed previous work and provided guidance throughout the project. Prof. Dr. Dr. Jürgen Debus served as an advisor for the first half of my PhD. Prof. Dr. Mark E. Ladd acted as an independent referee for the physics faculty and, as such, was required to have no involvement in any project work or publications.

2 Background

In this chapter, the background relevant for this thesis is introduced. Fundamental concepts regarding the interactions of ions with matter are discussed in detail after which their implementation in Monte Carlo simulations is briefly touched upon. This will be followed by more application-oriented sections about the detection of ion beams and the field of ion-beam imaging in the context of ion-beam radiotherapy.

2.1 Interactions of ions with matter

The characteristic way in which ions deposit energy in matter led Wilson (1946) to propose the use of ion beams for cancer therapy. The underlying physical processes and the reasons for their remarkable therapeutic potential will be discussed in the following. This section will therefore focus on three main processes by which ions interact with matter: energy loss, scattering and fragmentation.

2.1.1 Energy loss

While traversing matter, ions transfer energy to the target material, resulting in their gradual deceleration. This energy loss is a stochastic process and varies for the individual particles of a beam. The average energy $\mathrm{d}E$ which ions deposit within an absorber over the unit path length $\mathrm{d}z$ is called linear stopping power S

$$S = S_{\text{tot}} = \left\langle -\frac{\mathrm{d}E}{\mathrm{d}z} \right\rangle = S_{\text{el}} + S_{\text{nuc}} + S_{\text{rad}}\,, \tag{2.1.1}$$

where the average characterizes the stochastic nature of individual particle interactions and thus reliably represents the collective effect of an entire beam. The stopping power consists of three components (Thomas 2012): the electronic S_{el}, nuclear S_{nuc} and radiative stopping power S_{rad}, which are all shown exemplarily in fig. 2.1 for protons and muons in water. While the nuclear stopping power is mainly important for E_{kin}/E_0

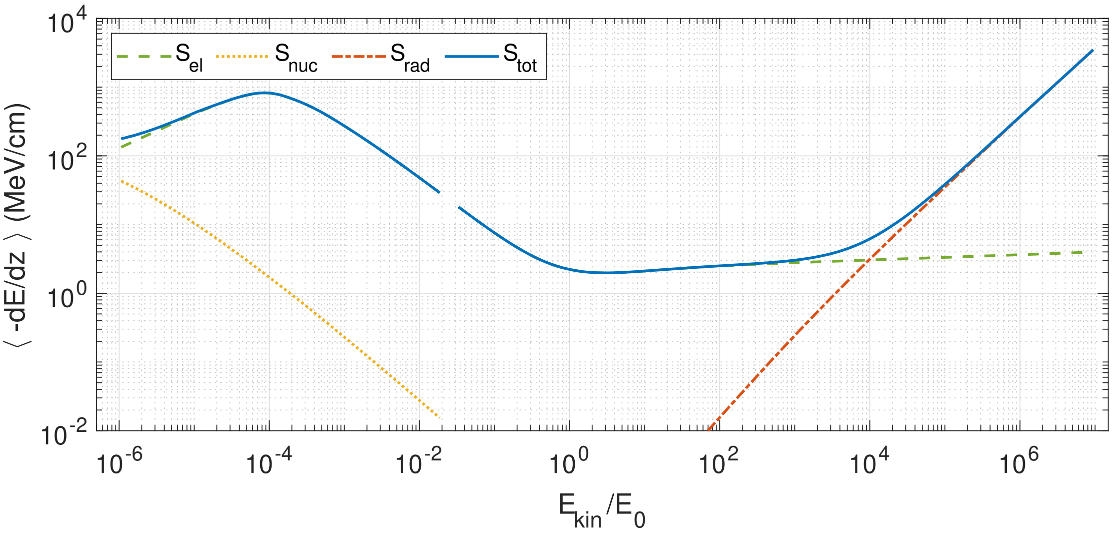

Figure 2.1: Mean stopping power of protons and muons in water plotted against their kinetic energy E_{kin} relative to their rest energy E_0. Data below 0.02 for protons was taken from Berger et al. (2017). Since no data was available for protons at higher energies, analogous to (Navas et al. 2024), data above 0.03 was taken from Groom et al. (2001) for muons to obtain an estimate for the shape of the curve. The total stopping power S_{tot} and its components S_{el}, S_{nuc} and S_{rad} are shown.

below 10^{-4} (Schardt et al. 2010), the radiative term becomes relevant for relative kinetic energies above 10^4 (Navas et al. 2024). Thus, the electronic stopping power governs the energy loss of ions for the intermediate energies, which include those used in medical applications. We will therefore solely focus on the electronic stopping power in the following.

Bethe (1930) formulated an equation describing the average energy loss for heavy charged particles in matter. Including later modifications, the mean electronic stopping power for a heavy particle can be described by (Navas et al. 2024)

$$\left\langle -\frac{\mathrm{d}E}{\mathrm{d}z} \right\rangle = K\rho z_{\mathrm{p}}^2 \frac{Z}{A}\frac{1}{\beta^2}\left[\frac{1}{2}\ln\left(\frac{2m_{\mathrm{e}}c^2\beta^2\gamma^2 W_{\max}}{I^2}\right) - \beta^2 - \frac{\delta}{2} - \frac{C}{Z} + z_{\mathrm{p}}L_1 + z_{\mathrm{p}}^2 L_2\right], \tag{2.1.2}$$

which is commonly referred to as the Bethe-Bloch equation. The parameters occurring in this equation are the mass density of the target ρ, the atomic charge and mass of the target Z and A, the charge number of the projectile z_{p}, the relativistic speed of the projectile β and corresponding Lorentz factor γ, the maximum energy transfer per collision $W_{\max}$ and the mean excitation energy I of the target. The constant K is thereby defined as (Navas et al. 2024)

$$K = 4\pi N_\mathrm{A} r_\mathrm{e}^2 m_\mathrm{e} c^2 \, , \tag{2.1.3}$$

including Avogadro's constant N_A, the classical electron radius r_e, the electron mass m_e and the speed of light c.

Dependence on the projectile's kinetic energy

Equation (2.1.2) describes a very complex interplay of many processes which become relevant for different ranges of the particles' kinetic energy. To simplify and understand the equation, we will discuss it in different regimes of the relativistic kinetic energy factor $E_\mathrm{kin}/E_0 = \gamma - 1$. At $\gamma - 1 \approx 2$, the particle is referred to as minimum ionizing particle (MIP) since the mean stopping power reaches a minimum there.

For $\gamma - 1 > 2$, an increase of the stopping power can be observed in fig. 2.1, which is due to the relativistic extension of the field of the projectile. In eq. (2.1.2), this is reflected by the logarithmic term. Additionally, the stopping power increases due to an implicit dependence of W_max on the projectile's kinetic energy (Navas et al. 2024)

$$W_\mathrm{max} = \frac{2 m_\mathrm{e} c^2 \beta^2 \gamma^2}{1 + 2\gamma m_\mathrm{e}/M + (m_\mathrm{e}/M)^2} \, , \tag{2.1.4}$$

where M is the mass of the projectile.

The density correction term $\delta/2$ in the Bethe Bloch eq. (2.1.2) accounts for the fact that at high energies, the ions begin to polarize the medium thus shielding themselves from interactions with electrons further away. It therefore partly counteracts the increase of electronic stopping power for higher energies (Navas et al. 2024).

For $10^{-4} < \gamma - 1 < 2$, the inverse quadratic dependence on β is governing the energy loss which corresponds to the relatively straight part of the curve in fig. 2.1 with slope -1. The steep increase of stopping power for decreasing $\gamma - 1$ accounts for the longer time during which the ions can interact with the surrounding electrons (Navas et al. 2024). When the speed of the projectile is in the order of that of the target's electrons, the term C/Z, called shell correction, gains importance. The last two correction terms were introduced by Barkas and Bloch, which are linearly and quadratically dependent on the projectile charge, respectively, and become relevant for relative kinetic energies below 10^{-4} (Navas et al. 2024).

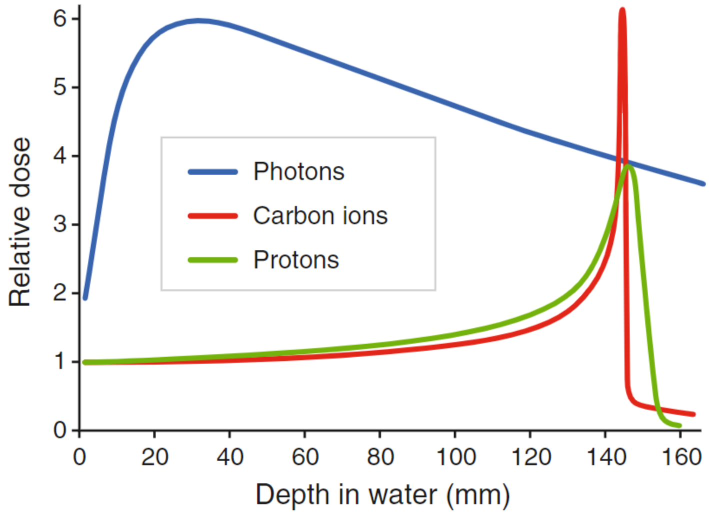

Figure 2.2: Depth-dose curve of photons, protons and carbon ions. The curve is expressed relatively to the entrance dose. Reprinted from Grau et al. (2020), CC BY 4.0.

Depth-dose curve

For medical purposes, initial beam energies of up to several hundred MeV/u are employed. Therefore, the logarithmic term rather behaves constant and the energy loss is mainly governed by the $1/\beta^2$ dependency.
When a particle with the described initial energy penetrates a medium, it transfers energy to it and is consequently decelerated. Thus, $\gamma - 1$ is reduced which in turn leads to an even higher loss of energy and a more rapid reduction of $\gamma - 1$.

In fig. 2.2, this escalation of energy deposited in a medium is shown for protons and carbon ions in water. Note that instead of the stopping power, the dose relative to that at the surface is shown here. The dose D can be approximated by multiplying the stopping power S by the fluence ϕ and dividing by the target's mass density ρ (Schlegel et al. 2018, p.548)

$$D(x,y,z) = \frac{1}{\rho}\frac{\mathrm{d}E(z)}{\mathrm{d}z}\phi(x,y,z) \tag{2.1.5}$$

while the fluence ϕ itself is defined as the number of particles N penetrating a sphere with the cross-section A (Schlegel et al. 2018, p.5)

$$\phi = \frac{\mathrm{d}N}{\mathrm{d}A}\,. \tag{2.1.6}$$

In eq. (2.1.5) the stopping power as a function of depth is used, which is not easily obtained from eq. (2.1.2). An analytical approximation of this complicated functional relation was derived by Bortfeld (1997) based on Geiger's law (Hall 2018)

$$-\frac{\mathrm{d}E}{\mathrm{d}z} = \frac{1}{p\alpha^{1/p}}(R-z)^{1/p-1}\,, \tag{2.1.7}$$

which will play a major role in this thesis. Here, α and p are material-dependent constants (Bortfeld 1997, Zhang et al. 2010) and R corresponds to the range of the beam, which will be introduced in the following.

In fig. 2.2, it can be observed that the relative dose does not diverge like one could expect from the $1/\beta^2$ dependence of the stopping power. This is partly due to the described correction terms of the mean stopping power for low energies. However, the steepness of the fall-off is mainly caused by the last factor in eq. (2.1.5): at this point, the primary ions stop and the fluence drops to zero. This stopping point of the ions is referred to as range R and can be calculated by integrating the inverse stopping power (Schlegel et al. 2018, p. 18)

$$R = \lim_{E_0 \to 0} \int_{E}^{E_0} \frac{1}{S(E')} \mathrm{d}E'\,. \tag{2.1.8}$$

For this calculation of the range, the continuous slowing down approach (CSDA) is employed. It assumes that ions lose their energy continuously, which is a valid approximation for many processes. The range of different projectiles $\mathrm{p1}$ and $\mathrm{p2}$ with the same kinetic energy per nucleon can be approximately related as (Schlegel et al. 2018, p. 18)

$$\frac{R_{\mathrm{p1}}}{R_{\mathrm{p2}}} = \frac{M_{\mathrm{p1}}}{M_{\mathrm{p2}}}\frac{z_{\mathrm{p2}}^2}{z_{\mathrm{p1}}^2}\,. \tag{2.1.9}$$

From this equation, we can conclude that carbon ions have an approximately three times shorter range than protons and helium ions. Therefore, in fig. 2.2, the carbon ion beam must have a higher initial beam energy than the proton beam in order to reach the Bragg peak at the same depth.

The steep falling and rising edge of the depth-dose curve in fig. 2.2 led Wilson (1946) to propose the use of proton beams for cancer treatment. Compared to conventionally used photons, ions deposit their maximum energy at a specific depth at which they stop. The resulting sharp peak discovered by William Henry Bragg is commonly referred to as Bragg peak (Bragg 1904, Bragg and Kleeman 1905). The idea of Wilson was to place this peak inside of the tumor volume, thereby focusing the dose more precisely on the tumor than with photons. This idea will be followed in more detail in section 2.4.

Dependence on the projectile's charge number

Apart from the complex β dependence of the Bethe-Bloch equation eq. (2.1.2), we can observe several parameters of the projectile influencing the stopping power. Besides the correction terms and a slight mass dependence of W_{max}, we are mainly left with a quadratic dependence on the projectile's charge z_{p}^2. For medical purposes, this directly implies that nuclei with higher charge deposit overall more energy in the tissue.

Dependence on the target properties

Furthermore, eq. (2.1.2) exhibits a linear dependence on Z/A of the target. Additionally, the ionization potential I of the target influences the stopping power. Since the latter contributes to the argument of the logarithm, its influence for clinical intensities is rather low, but non-negligible. To extract the dependence of the stopping power only on the target characteristics, it can be expressed relative to the one in water. In that way, the dependence on the projectile's charge and velocity approximately cancels out, since most human tissue is at least similar to water. By doing so we arrive at the relative stopping power (RSP)

$$\mathrm{RSP}(E) = \frac{S(E)}{S_{\mathrm{water}}(E)} \,. \tag{2.1.10}$$

Another quantity expressed relative to water, which is highly important throughout the whole thesis, is the water-equivalent thickness (WET). It corresponds to the integral over the thickness element $\mathrm{d}x$ weighted with its RSP

$$\mathrm{WET} = \int_0^L \mathrm{RSP}(x)\mathrm{d}x \,. \tag{2.1.11}$$

The WET expresses how thick a water column would need to be to slow down a particle as much as the material of interest. Thus, high-density materials usually have higher WETs than their geometrical thickness. Since the energy and ion-type dependence of the RSP of human tissue is negligible (Parodi 2024), the same can be assumed for WET.

Energy and range straggling

The Bethe-Bloch equation eq. (2.1.2) describes the mean energy loss of heavy ions in matter. A single ion loses its energy in a myriad of single interactions, which are all stochastic processes. Even if we consider a perfectly mono-energetic beam, this beam will have an energy spread after traversing an absorber due to the individually different interactions of the ions. The standard deviation σ_{E} in energy loss was derived by Tschalär and Maccabee (1970)

$$\sigma_{\mathrm{E}}(\bar{E}) = S^2(\bar{E}) \int_{E_{\mathrm{init}}}^{\bar{E}} \kappa_2 \frac{1}{S^3(E)} \mathrm{d}E \quad \text{with} \quad \kappa_2 = K\rho_e \frac{1-0.5\beta^2}{1-\beta^2}\,, \tag{2.1.12}$$

where the initial beam energy is referred to as E_{init} and the electron density as ρ_e. This variation in energy loss around the mean value is known as energy straggling, and it also leads to a corresponding spread in the particles' range. The variance of the range straggling can be calculated through (Durante and Paganetti 2016)

$$\sigma_{\mathrm{R}}^2 = \int \left(\frac{\mathrm{d}E}{\mathrm{d}z}\right)^{-3} \frac{\mathrm{d}\sigma_{\mathrm{E}}}{\mathrm{d}z} \mathrm{d}E \tag{2.1.13}$$

in case of a Gaussian energy straggling. Durante and Paganetti (2016) also provide a useful estimate for comparison of the extent of range straggling for two different ion types, which scales with the square root of their inverse masses

$$\frac{\sigma_{R1}}{\sigma_{R2}} = \sqrt{\frac{M_2}{M_1}}\,. \tag{2.1.14}$$

2.1.2 Scattering

Due to electromagnetic interactions with predominantly the target nuclei, ions are laterally deflected from a straight path. In most interactions, ions are deflected by small angles, which would be negligible for a single event. However, due to the vast amount of interaction partners, the lateral scattering accumulates and becomes significant. This phenomenon called multiple Coulomb scattering (MCS) can be described by Molière's theory (Molière 1948) which describes the process adequately for both small and large-angle scattering events. However, it is rather complex and computationally intense. Therefore, different simplifications have been made.

A Gaussian approximation can adequately describe the scattering distribution for around 98 % of the ions (Navas et al. 2024). Based on this simplification, Highland (1975) proposed an empirical equation for the scattering angle. Here, the angle θ_0 refers to the root-mean-square width of the distribution of the scattering angles projected onto a plane orthogonal to the beam. With later modifications, the so-called Highland formula reads (Highland 1975, Lynch and Dahl 1991)

$$\theta_0 = \frac{13.6\,\mathrm{MeV}}{\beta c p} z_{\mathrm{p}} \sqrt{\frac{x}{X_0}} \left[1 + 0.038 \ln\left(\frac{x z_{\mathrm{p}}^2}{X_0 \beta^2}\right)\right]\,, \tag{2.1.15}$$

where x/X_0 is the material budget in terms of radiation lengths. For most applications, this Gaussian approximation is sufficient to calculate the scattering angle. However, it does not properly incorporate large-angle scattering events.

2.1.3 Fragmentation

If ions have enough energy to overcome the Coulomb barrier, they can interact with the target nuclei directly. During such interactions, both the target and projectile may disintegrate, resulting in secondary particles commonly referred to as fragments. The fragmentation leads to a reduction of the flux of primary ions, which can be estimated to be roughly around 4 %/cm for carbon ions and 1 %/cm for protons in the therapeutic energy range (Schlegel et al. 2018, p. 19).

Tripathi et al. (1996) suggested a parametrization for the cross section σ_F of a nucleus-nucleus interaction based on the preceding work of Bradt and Peters (1950), Townsend and Wilson (1986)

$$\sigma_{\mathrm{F}} = \pi r_0^2 (A_{\mathrm{p}}^{1/3} + A_{\mathrm{T}}^{1/3} + \delta_{\mathrm{E}})^2 (1 - B/E_{\mathrm{cm}})\,, \tag{2.1.16}$$

where r_0 is the nucleon radius, δ_{E} an energy-dependent correction factor, B the Coulomb interaction barrier, and E_{cm} the center-of-mass energy per nucleon. Equation (2.1.16) reveals a dependency of the cross section on the target's and projectile's atomic mass A_{p} and A_{T}. We can thus conclude that fragmentation per incident ion increasingly occurs for heavier particles.

More descriptively, the fragmentation process can be explained by the abrasion-ablation model (Serber 1947). The abrasion phase is entered when the projectile collides with the target nucleus. In the overlap region, a fireball is created. In the ablation phase, this fireball forms clusters which subsequently decay further until the fragments reach a stable state. During the ablation phase, different daughter nuclei are formed. The projectile fragments can inherit an energy per nucleon comparable to that of the original projectile before the collision. Due to their smaller squared charge over mass (see eq. (2.1.9)), their range can be significantly higher than that of the primary ions. Therefore, they contribute to the depth-dose curve with a so-called fragment tail behind the Bragg peak, especially for heavier ions like carbon (as also seen in fig. 2.2). Furthermore, the excited nuclei nearly instantaneously emit highly energetic photons, so-called prompt gammas. Due to β^+-decays, photons stemming from positron-electron annihilations are also emitted in the ablation phase.

2.2 Monte Carlo simulation of particle transport

In the previous section, the interactions of ions with matter were described mathematically. However, it is difficult to analytically describe particle transport in heterogeneous media in a closed form. Therefore, Monte Carlo simulations (Metropolis and Ulam 1949) are employed to simulate particle transport in matter. These simulations are based on random sampling of particle steps and interactions with probabilities given by physics-informed cross sections (Berger 1963, Raeside 1976). In the following, a brief overview over the conducted steps is given (Dedes and Parodi 2015, Haghighat 2020):

- **Initialization:** A particle is initialized as a point in phase space. The different dimensions correspond to the degrees of freedom of the particles, such as position, momentum, mass, spin of particle etc. Furthermore, the material properties and geometry of the target are defined.

- **Transport:** The particle is moved by the exponentially distributed distance s, which is calculated by (Liljequist 2012)

  $$s = -\lambda \ln(1 - R) \tag{2.2.1}$$

  where R is a uniformly distributed, quasi-random number between 0 and 1 (Liljequist 2012). Theoretically, λ should correspond to the mean free path of the particle. For ions, the mean free path is very small as compared to their range and thus, the computation time would increase drastically. Therefore, many Monte Carlo frameworks for heavy ion transport follow the so-called condensed history approach (Berger 1963), where several interactions are combined into one.

- **Interaction:** After the translation of the particle, the interaction is simulated. All interactions which the particle can theoretically undergo are assigned physics-informed cross sections σ_i which all sum up to the total cross section σ (Ivanchenko and Pandola 2024). Each interaction occurs with a probability of (Ivanchenko and Pandola 2024)

  $$p_i = \frac{\sigma_i}{\sigma}\,. \tag{2.2.2}$$

  The type of interaction is decided by pseudo-randomly sampling from the corresponding probability function (Ivanchenko and Pandola 2024). After this interaction, e.g., energy loss, scattering, fragmentation, or the creation of a δ-electron, the new coordinates in phase space are calculated. If new particles were created due to the interaction, their coordinates in phase space are initialized and they are added to the stack of particles to be simulated in the following iterations.

- **Repetition:** Further translations and interactions of the particle are simulated until it fulfills a stopping condition, e.g., exiting a predefined space, or falling below an energy threshold.

If a reasonable number of particles is simulated, the data of all phase space trajectories for all simulated particles quickly exceeds the amount of processable data. Therefore, it must be defined which quantities are to be saved, which is called scoring. Often, the dose to a certain target is scored, but also any other variable e.g., the tracks of ions, their velocity or the fluence of fragments can be requested as output.

2.3 Detection of ion beams with semiconducting detectors

To detect ion beams, their characteristics of ionizing the matter they traverse can be utilized. As described in section 2.1.1, they interact with a multitude of target electrons leaving lots of electron-hole pairs behind. To detect and quantify radiation, a variety of detection principles and different detector layouts exist. In this work, semiconducting hybrid detectors will play a major role, which is why they will be discussed in the following.

Semiconductors are well-suited for detection of ionizing radiation since their band gap is inherently low. In silicon, 3.6 eV of energy are needed to create an electron-hole pair (Bussolati et al. 1964). Through doping, the properties of a semiconductor can be influenced: by introducing these impurity atoms, the concentration of electrons or holes and thus the conductivity of the semiconductor can be increased. A p-doped semiconductor contains atoms with fewer valence electrons whereas an n-typed one contains atoms with an additional valence electron (Spieler 2005, p.13). If a p- and n-doped substrate are combined, the charge carriers in the p-n-junction zone recombine resulting in a depletion zone with no charge carriers left. This depletion zone can be expanded over parts or even the whole semiconductor if a bias voltage opposing the electric field caused by charge migration in the depletion zone is applied (Spieler 2005, p.13-15).

If an ionizing particle now creates electron-hole pairs in the depletion zone, electrons and holes are separated due to the attraction by the respective electrodes and a voltage signal can be detected. While these charge clouds drift in opposite directions, diffusion and the repulsive electric force within the clouds cause them to expand (Spieler 2005, p.16-18).

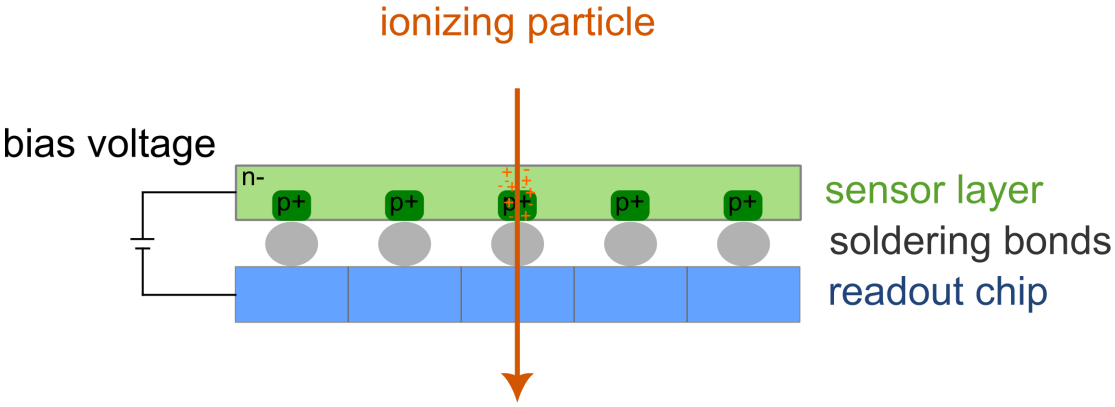

Figure 2.3: Cross section of semiconducting hybrid detector. In this example, the sensor layer consists of a n-doped substrate with p-doped implants. Via bump-bonds, the p-doped implants are connected to a readout chip. A reverse bias voltage is applied between sensor and readout chip increasing the depleted volume within the semiconductor. If an ionizing particle traverses the detector, it creates electron-hole pairs within the sensor layer. The charge carriers are drawn to the respective electrode creating a voltage signal.

In fig. 2.3, the cross-section of a hybrid semiconducting detector is shown, which consists of a semiconductor and a separate component for the readout. Both parts are connected via small soldering bonds for each pixel of the readout (Spieler 2005, p.11). In this example, the sensor layer is composed of a n-type substrate with p-type implants. The charge clouds created by the incoming ionizing particle drift to the electrodes due to the applied reverse bias voltage. As a result of the expansion process, the cloud can spread over several pixels of the readout, yielding a cluster of hit pixel signals (Jakůbek 2009). To obtain the whole signal of the particle, all pixels need to be taken into account. The number of contributing pixels, the shape of the cluster, the total signal and its spatial distribution can then be important parameters to extract different quantities from the measured signal (Jakůbek et al. 2010, Granja et al. 2018). In order to mitigate noise on the detector, usually a threshold voltage is set which needs to be exceeded in order for the signal to be registered.

2.4 Ion-beam radiotherapy

Ion-beam radiotherapy is of growing interest (Hartsell et al. 2024). Currently, there are more than 130 particle therapy centers in operation (PTCOG 2025b) with many more being under construction (PTCOG 2025a) or in the planning stage (PTCOG 2025c). By the end of 2023, more than 400,000 patients have been treated with ion-beam therapy (PTCOG 2023).

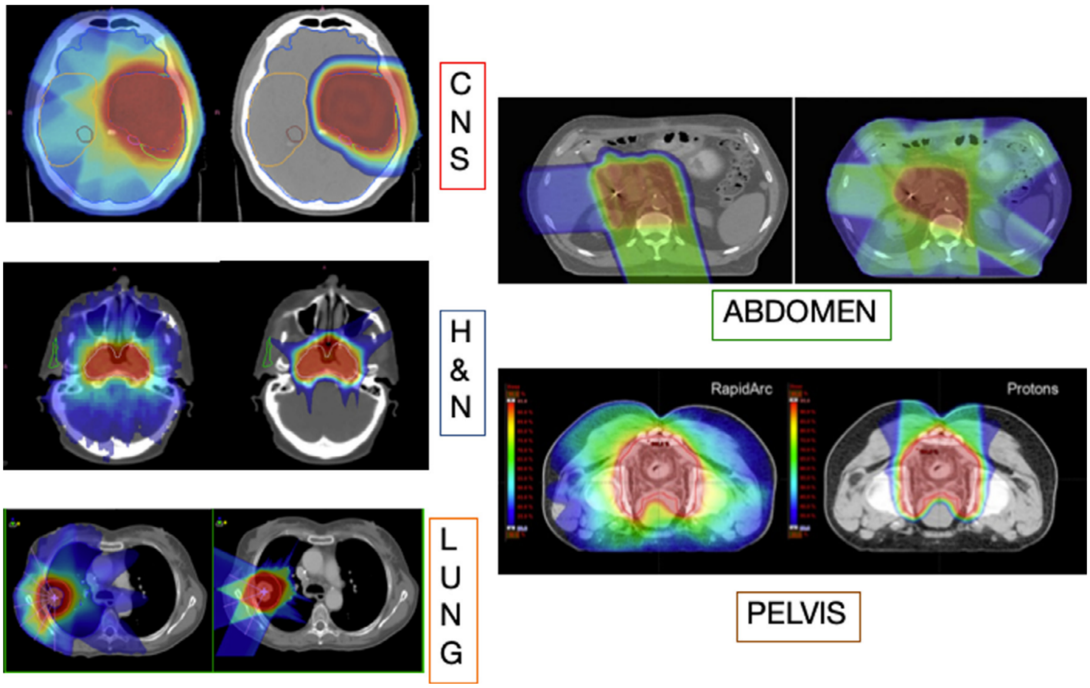

Figure 2.4: Physical dose distributions created with photons (CNS, H&N, lung, pelvis: left, abdomen: right) and protons (CNS, H&N, lung, pelvis: right, abdomen: left) for several tumor sites. Reprinted from Durante et al. (2019), CC BY-NC-ND 4.0.

In section 2.1.1, the motivation for the use of ions for radiotherapy was already briefly touched upon: compared to conventionally used photons, ions deposit their energy in a more focused way. This is due to the Bragg peak within their dose-depth curve, which was shown in fig. 2.2. By choosing the initial beam energy accordingly, the Bragg peak can be positioned at any depth. If several beam energies are combined, a so-called spread-out Bragg peak (SOBP) can be created over depth. Additionally, for each initial beam energy, the beam can be deflected due to bending magnets thereby scanning the tumor laterally to the beam axis (Haberer et al. 1993). In that way, conformal dose distributions can be created, which are then usually delivered over the course of several weeks in so-called fractions (Thames 1988, Fletcher 1988, Joiner and Bentzen 2018).

In fig. 2.4, dose distributions for different tumor sites are shown for both photon and proton-beam treatments. Here, it can be seen that the integral dose is reduced for proton beam treatments compared to the ones with photons (Schulz-Ertner and Tsujii 2007, Palm and Johansson 2007, Schardt et al. 2010, Van De Water et al. 2011, Durante and Debus 2018). This promises to be connected with less normal tissue complications or better tumor control (Paganetti et al. 2012, Leeman et al. 2017). It is important to mention that there are a multitude of radiobiological aspects which must also be taken into account when comparing the effectiveness of different particle types for external radiotherapy (Durante et al. 2021). However, we will not examine this broad topic worthy of standalone treatment, as it is not particularly relevant to the objectives of this thesis.

Considering the focused dose distributions in fig. 2.4, it becomes apparent that these highly precise treatments must be delivered accurately. Otherwise, parts of the tumor might not be treated properly and healthy tissue to be spared is irradiated instead. Compared to photon treatments, it is therefore of special importance to ensure an accurate treatment and to mitigate uncertainties (Paganetti 2012).

In clinics, these uncertainties are usually considered within margins, which are applied around the clinical tumor volume. Many centers established their own regulations to determine the size of the margin which can depend, among other factors, on the treated body site and the range of the beam. Often the applied margins amount to 3.5 % of the range (Paganetti 2012), which corresponds to e.g., 7 mm for a beam range of 200 mm.

These margins increase the irradiated volume and by definition involve healthy tissue. To fully exploit the potential of ion-beam radiotherapy with its steep gradients and conformal dose distributions, mitigating the uncertainties and therefore the margins is a major goal. In the following, a brief overview of the clinical workflow in ion-beam radiotherapy will be given with a special focus on uncertainties and the respective imaging techniques to mitigate these.

2.4.1 The role of imaging within the clinical workflow

Ion-beam radiotherapy critically depends on imaging since imaging plays a crucial role for cancer diagnosis, a precise treatment delivery and for follow-up examinations. While we will not delve into diagnostic and follow-up imaging here, our focus will instead be on imaging throughout the ion-beam radiotherapy treatment workflow. Furthermore, we will concentrate on static targets, as the treatment of moving targets involves a broader range of imaging modalities. What follows is a non-exhaustive overview of the imaging approaches relevant to this context.

Treatment planning

Once a patient has been diagnosed with cancer and ion-beam radiotherapy has been selected as one of the treatment modalities, the therapy is individually tailored to the patient's anatomy and the specific shape of the tumor. In order to conformally shape the SOBP to the tumor volume, a planning CT is acquired of each patient before treatment start (Wohlfahrt and Richter 2020). Within this 3D volume, the tumor and adjacent anatomical features are delineated to identify the target volume and all critical regions. Furthermore, the CT numbers (CTN) are converted to RSP such that the dose deposited by the particle beams can be calculated. The conversion from CTN to RSP is usually performed with the so-called stoichiometric method (Schneider et al. 1996).

Following this method, different tissue surrogates with a known elemental composition are employed. First, two effective atomic numbers of each sample are determined (Jackson and Hawkes 1981, Rutherford et al. 1976, Schneider et al. 1996)

$$\tilde{Z} = \left[\sum_i \lambda_i Z_i^{3.62}\right]^{1/3.62} , \quad \hat{Z} = \left[\sum_i \lambda_i Z_i^{1.86}\right]^{1/1.86} \tag{2.4.1}$$

with (Jackson and Hawkes 1981, Seltzer and Berger 1982)

$$\lambda_i = \frac{\frac{w_i Z_i}{A_i}}{\sum_i \frac{w_i Z_i}{A_i}} , \tag{2.4.2}$$

where w_i is the mass proportion of the element within the compound and A_i and Z_i are the atomic mass and charge number of it.

In a second step, CT scans of the tissue-equivalent materials are acquired and their CTN is obtained. From this, their linear attenuation coefficient can be obtained with the following equation

$$\text{CTN} = 1000\,\frac{\mu - \mu_{\text{water}}}{\mu_{\text{water}}} , \tag{2.4.3}$$

where μ is the linear attenuation coefficient. Now that we have both attenuation coefficient and the effective atomic numbers $\tilde{Z}$ and $\bar{Z}$ for each sample, we can plot them against each other. Through the points, a fit following the function (Jackson and Hawkes 1981, Rutherford et al. 1976, Schneider et al. 1996)

$$\mu = \rho_\text{e}(\sigma^{\text{ph}} + \sigma^{\text{coh}} + \sigma^{\text{incoh}}) = \rho_\text{e}(K^{\text{ph}}\tilde{Z}^{3.62} + K^{\text{coh}}\hat{Z}^{1.86} + K^{\text{incoh}}) \tag{2.4.4}$$

can be performed to obtain the three parameters K. Here, ρ_e is the electron density, while K^{ph}, K^{coh} and K^{incoh} are constants characterizing the cross sections of the photoelectric effect, coherent scattering and incoherent scattering (Jackson and Hawkes 1981). These parameters are scanner specific and allow for the theoretical calculation of the CTN of any material with a known chemical composition.

After the coefficients have been obtained by means of the tissue surrogates, the theoretical CTN can be calculated using eq. (2.4.3) and eq. (2.4.4) for human tissue with a known chemical composition. Furthermore, the RSP can be calculated by the Bethe-Bloch formula described in section 2.1.1 in a slightly modified form (Bichsel 1969, Schneider et al. 1996)

$$\mathrm{RSP} = \frac{\rho_\mathrm{e}}{\rho_\mathrm{e,water}} \frac{\ln\left(\frac{2m_e c^2 \beta^2}{I_\mathrm{m}(1-\beta^2)}\right) - \beta^2}{\ln\left(\frac{2m_e c^2 \beta^2}{I_\mathrm{water}(1-\beta^2)}\right) - \beta^2} \,. \tag{2.4.5}$$

Here, the energy dependence of the RSP is usually neglected and for protons an initial beam energy of 100 MeV is assumed (Peters et al. 2023). In order to obtain the ionization potential I_m for the tissue samples, the Bragg additivity rule is employed, analogously to eq. (2.4.2) (Seltzer and Berger 1982)

$$\ln I_m = \frac{\sum_i \frac{w_i Z_i}{A_i} \ln I_i}{\sum_i \frac{w_i Z_i}{A_i}} \,. \tag{2.4.6}$$

If now the theoretical CTN and RSP for the human tissues are plotted against each other, another fit can be performed, this time yielding the so-called Hounsfield look-up table (HLUT). Usually, the fit for this stoichiometric calibration (Schneider et al. 1996) is performed piecewise for different intervals of CTN. Schneider et al. (1996) suggested to use three linear fits plus two connecting lines to account for adipose tissue. By now, the use of four fits and three connecting lines in between is recommended (Peters et al. 2023).

Since there is no direct physical relationship between attenuation of photons and deceleration of ions, the accuracy of RSP determination based on single-energy computed tomography (SECT) is inherently limited. Two different tissues can have the same CTN but different RSP, which is not resolvable with the SECT technology. Therefore, uncertainties of around 3 % (1.5σ) in range can arise already due to the uncertainty on RSP values based on SECT (Paganetti 2012, Yang et al. 2012, Wohlfahrt and Richter 2020).

An approach to address this limitation is the use of two different X-ray spectra for the acquisition of the CT, called dual-energy computed tomography (DECT). Since the attenuation coefficient μ is energy dependent, measuring it with two different energies allows for a better differentiation between similar materials. There is a multitude of approaches for the acquisition of DECT data (McCollough et al. 2015), which will not be discussed in detail here in the interest of brevity.

Usually, scans with two different X-ray spectra are used to determine the relative electron densities and the effective atomic number, the latter of which can then be translated

to the ionization potential. These two quantities can be inserted into the Bethe-Bloch equation eq. (2.1.2) to calculate the RSP (Wohlfahrt and Richter 2020). Numerous other approaches exist for the RSP determination based on DECT data, which are covered extensively in pertinent literature (Wohlfahrt and Richter 2020).
With these techniques, the uncertainties connected to the RSP values of the treatment planning CT can be reduced to around 2 % in range (Li et al. 2017, Peters et al. 2022).

Patient positioning

Another source for uncertainties is connected to the reproducibility of the positioning of the patient (Landry and Hua 2018). For each treatment fraction, the positioning of the patient in the planning CT must be replicated. For this purpose, many immobilization and positioning devices like thermoplastic masks are used in clinical routine (Wroe et al. 2015). Additionally, pre-treatment imaging is typically employed at this stage as part of standard practice. In many centers, two orthogonal X-ray projections are acquired and registered to the CT (Jans et al. 2006, Landry and Hua 2018). The resulting transformation is then applied to the patient couch. Other centers use cone-beam CT, which could also be used for a verification of the patient's anatomy (Jaffray et al. 1999, Landry and Hua 2018). Also, surface guidance can be integrated into the process (Freislederer et al. 2020, Qubala et al. 2023).

In-vivo range verification

Treatment planning enables the creation of conformal dose distributions. However, the actual delivered dose may differ from the planned distribution due to various uncertainties e.g., on the planning itself, beam delivery, or the patient's anatomy. To detect and adjust for discrepancies, additional imaging modalities are increasingly developed and employed (Parodi 2024).

In order to monitor the in-vivo range of the treatment beams, several imaging modalities have been developed, which mainly utilize secondary or tertiary particles created during ion-beam treatments. Therefore, they do not cause any additional dose to the patient. Utilizing algorithms to reconstruct the origin of these particles, images can be created which should give insight into the in-vivo dose distribution.

Range verification based on positron emission tomography (PET) relies on the detection of two photons emitted in opposite directions, at an angle of 180° relative to each other. They result from the annihilation of a positron, produced by the decay of a fragmentation event, with an electron inside the patient. However, low signal-to-noise ratio and a biological washout due to the life time of the positron emitters in the order of minutes pose problems (Parodi 2024).

Another technique is prompt gamma imaging which is based on photons created directly during the decay of excited nuclei. Biological washout is not relevant in this context due to the nearly instantaneous emission of the photons after the fragmentation, which happens within nanoseconds (Parodi 2024). Furthermore, the statistical power is better compared to PET. However, the detection of these highly energetic photons and the high background are challenging (Knopf and Lomax 2013).

Charged nuclear fragments can be used to monitor carbon-ion treatments. If two detection layers are employed to measure coincident hits, the background can be drastically reduced (Kelleter et al. 2024). As for prompt gamma imaging, washout is not affecting these measurements due to the almost immediate creation of the fragments. However, Multiple Coulomb scattering within the patient decreases the resolution. Furthermore, a compromise between statistics and spatial resolution has to be made by choosing the detector's angle to the beam axis (Ghesquiere-Dierickx et al. 2021).

Furthermore, ionoacoustic imaging has been suggested as an approach for online in-vivo range monitoring (Hayakawa et al. 1995, Hickling et al. 2018). It is based on the measurement of thermoacoustic waves created by pulsed ion beams. Remaining challenges include the low signal to noise ratio at clinical doses and acoustic heterogeneities of the patients (Lehrack et al. 2017, Parodi and Assmann 2021).

2.5 Ion-beam imaging

Another imaging approach to increase the precision of ion-beam radiotherapy treatments is to use the ion beam itself for that purpose. In order for this to work, higher initial beam energies have to be employed such that the beam can traverse the object to be imaged and then be detected with specialized detectors. This approach is quite attractive since images can be acquired in beam's eye view right before the treatment and no conversions between different particle types are needed. Ion-beam imaging could be integrated into the workflow in several ways, which will be discussed in the following.

In order to eliminate the uncertainties arising from the conversion of CTN to RSP, an ion-beam CT (iCT) could be acquired for the planning of the treatment instead of an X-ray CT. However, experimental studies have found that the RSP accuracy of proton and helium CT is similar to the one of DECT (Bär et al. 2022, Volz et al. 2021).

Since an acquisition of a DECT is cheaper and the treatment beam is not occupied, it is questionable whether there is a strong indication for iCT. However, iCT promises to impose a lower dose on the patient (Meyer et al. 2019). Furthermore, iCT imaging could be applied for patients with metal implants due to less pronounced artifacts (Civinini et al. 2020).

In contrast to iCT, a single ion-beam projection, a so-called ion-beam radiograph (iRad) cannot provide a 3D RSP distribution since it only shows a 2D projection along beam direction. If the imaging beam is chosen in the same direction as the treatment beam, this projection can also yield relevant information for clinicians: the integral over the RSP along the imaging beam path, which equals the WET as introduced in eq. (2.1.11). In very good approximation it is independent from the initial beam energy (see section 2.1.1).

As pointed out, iRad cannot be used for the planning of the treatment. Instead, the low dose of an iRad makes it an interesting modality for daily imaging. An iRad could be obtained right before each treatment fraction when the patient is positioned for the treatment. The WET-map could be acquired in beam's eye view and compared with the one calculated from the treatment planning CT (Schneider and Pedroni 1995, Deffet et al. 2021, Sarosiek et al. 2021, Palaniappan et al. 2021). In that way, coarse errors due to RSP uncertainties or changes in the patient's anatomy could be detected and quantified and their impact on the dose distribution could be assessed (Martišíková et al. 2018). Furthermore, the radiograph could be used for positioning of the patient (Schneider and Pedroni 1995, Romero et al. 1995, Hammi et al. 2018, Palaniappan et al. 2019). In that way, the orthogonal X-ray projections of current practice could be replaced while imposing a similar dose on the patient (Schulte et al. 2005, Schneider and Pedroni 1995, Depauw and Seco 2011, Arbor et al. 2015, Meyer et al. 2019, Miller et al. 2019). Since the iRad would be acquired in the treatment position, no more couch movement introducing additional uncertainties would follow. Also for iRad, imaging of metal implants is less problematic than for other imaging modalities.

Apart from daily application directly before the treatment, iRads could be used to improve the CT calibrations (Schneider et al. 2005, Doolan et al. 2015, Collins-Fekete et al. 2017a, Krah et al. 2019, Gianoli et al. 2020, Fogazzi et al. 2024). Furthermore, during the treatment, helium-beam radiography could be performed if a mixed carbon-helium beam is accelerated in the synchrotron (Graeff et al. 2018, Mazzucconi et al. 2018). Since helium ions have an around three times higher range, for most treatment geometries they could traverse the patient and be used for an online verification of the carbon-ion treatment (Volz et al. 2020b, Hardt et al. 2024).

While all ion imaging approaches cover interesting and promising use cases, in this thesis we will focus on iRad prior to the treatment fractions with the aim of verification of the patient anatomy.

2.5.1 Ion-beam imaging systems

Two types of ion imaging systems can be distinguished: integrating and list-mode systems (Poludniowski et al. 2015). While the former consists of one detector only, the latter employs additional tracking detectors in the back, and often additionally in the front of the phantom. While integrating systems are usually cheaper and can process higher beam intensities, list-mode systems typically work with lower doses and exhibit higher spatial resolution (Poludniowski et al. 2015, Gianoli et al. 2024).

In order to infer the WET, different detector technologies are utilized. Conventionally, the residual energy or range is measured (Poludniowski et al. 2015). Enabled by recent detector developments, also time of flight (TOF) measurements are used to deduce the traversed WET (Krah et al. 2022, Ulrich-Pur et al. 2022, 2024). In this thesis, the energy deposited within a thin detector will be the measured quantity generating the contrast of our WET images.
Many promising ion imaging prototypes exist and even a first commercial product is available (DeJongh et al. 2021). Furthermore, a first patient study has been conducted (Meijers et al. 2021). Still, as of today, no ion-imaging system is used routinely in clinics yet.

2.5.2 Imaging with protons, helium and carbon ions

Since different ion types are used for ion-beam radiotherapy treatments, they can also be considered for imaging. In this section, a brief theoretical comparison of the different ion types for imaging is presented following the derivations of Gehrke et al. (2018a). Herein, we will focus on list-mode systems since such a system was used for the experiments presented in this thesis.

Most importantly, the ion types differ in the dose which they deposit in the patient. To facilitate a fair comparison of these three ion types, they should be compared at the same dose. This directly implies that a different number of particles must be used for the acquisition of an image. Furthermore, an equal range should be assumed (Gehrke et al. 2018a).

Considering contrast-to-noise ratio (CNR), range straggling of the ions plays a major role. Following eq. (2.1.14), the range straggling scales with the inverse square root of the mass of the ion. Therefore, helium ions and even more so carbon ions suffer from less range straggling than protons. However, the reduced number of particles for an equal dose approximately neutralizes this advantage, such that we arrive at a similar CNR for all ion types (Gehrke et al. 2018a)

$$\mathrm{CNR}^{^{12}\mathrm{C}} \approx 0.77\,\mathrm{CNR}^{^{4}\mathrm{He}}\,, \quad \mathrm{CNR}^{^{4}\mathrm{He}} = \mathrm{CNR}^{^{1}\mathrm{H}}\,. \tag{2.5.1}$$

The impact of different ion types on the spatial resolution is difficult to extract when considering the Highland formula in eq. (2.1.15). Here, it seems like a higher charge number z_p increases the extent of scattering for heavier ions. However, it is important to note here that in order to reach the same range, helium ions and even more so carbon ions must have a much higher momentum than protons. A detailed derivation of the relation of scattering between protons, helium and carbon ions can be found in Gehrke et al. (2018a), who obtained

$$\sqrt{\epsilon_{1,1}^{^{12}\mathrm{C}}} \approx \frac{1}{1.8}\sqrt{\epsilon_{1,1}^{^{4}\mathrm{He}}}\,, \quad \sqrt{\epsilon_{1,1}^{^{4}\mathrm{He}}} = \frac{1}{2}\sqrt{\epsilon_{1,1}^{^{1}\mathrm{H}}}\,. \tag{2.5.2}$$

for the first entries, describing lateral displacement, of the respective scattering covariance matrices ϵ. Consequently, Gehrke et al. (2018a) concluded that helium ions offer the best trade-off between CNR and spatial resolution (SR), which they also confirmed with simulations and measurements.

Another important factor is the ions' fragmentation, which was not taken into account for the abovementioned derivation of (Gehrke et al. 2018a). Fragmentation within the patient and the detection system causes severe noise, which must be filtered using advanced post-processing techniques (Volz et al. 2018, Gehrke et al. 2018b, Volz et al. 2019).

Furthermore, the availability of the different particle beams plays a role. While proton facilities are most widespread, quite a few centers also operate a carbon beam (PTCOG 2025b). Centers with a commissioned helium beam are still rare (Mairani et al. 2022). Therefore, most list-mode systems are currently still operated with a proton beam (Martišíková et al. 2018).

3 Material and Methods

In this chapter, the material and methods utilized for the experiments and analyses presented in this thesis are described. The materials consist of the ion-beam at the Heidelberg ion-beam therapy center, the detectors, their arrangement in a detection system and the imaged phantoms. The methods include e.g., the data processing, energy painting and 2.5D imaging. Also, the use of a Monte Carlo simulation framework for this specific project is described.

3.1 Heidelberg Ion-beam Therapy center

The Heidelberg Ion-beam Therapy center (HIT) is the first facility in Europe designed exclusively for proton and heavier ion treatments (Ondreka and Weinrich 2008). By the end of 2023, more than 9.000 patients have been treated since its opening in 2009 in this facility (PTCOG 2023). Most patients were treated with protons and carbon ions, which were already commissioned in 2009. In 2021, the first helium-ion radiotherapy treatment was conducted there (Tessonnier et al. 2023). Oxygen ions are also available at HIT, but only for research purposes.
All ion-beam radiography experiments conducted within the scope of this thesis were carried out at the Heidelberg Ion-beam Therapy center (HIT). Therefore, a brief overview over the layout of the center is given in the following. Afterwards, the beam settings used for our experiments are listed.

3.1.1 Layout

The layout of the HIT facility is schematically shown in fig. 3.1. Three ion sources (1) are available there, which can be used to extract protons, helium, carbon and oxygen ions. In the linear accelerator (2) they are pre-accelerated and then injected into the synchrotron (3). Here, the ions are accelerated further to the requested energy of up to 430 MeV/u corresponding to around 75 % of the speed of light (Ondreka and Weinrich

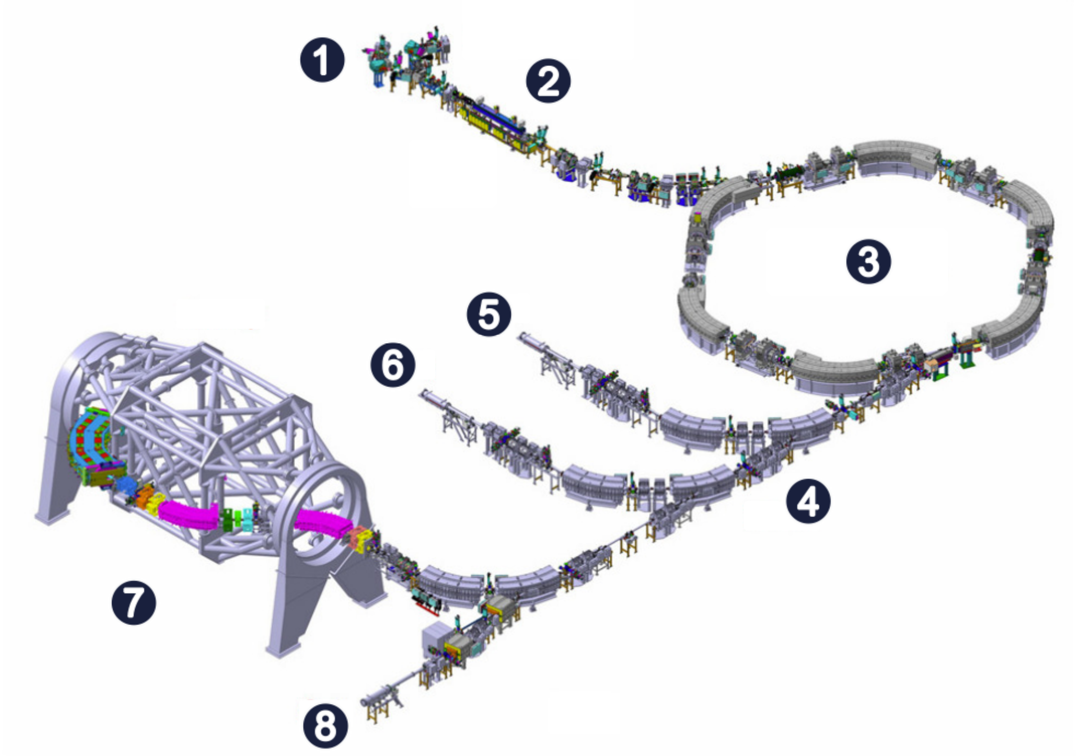

Figure 3.1: Layout of Heidelberg ion-beam therapy center. Ions from one of the three ion sources (1) are pre-accelerated in the linear accelerator (2). Then, they are injected into the synchrotron (3) and accelerated to the requested energy. By means of the high-energy beam transport system (4), the ion-beams are guided to the treatment rooms. There are two rooms with a fixed horizontal beam line (5,6). One room is equipped with a gantry (7) in which the beam can be delivered to the patient from arbitrary angles. One room with a horizontal beam line is dedicated to experiments (8). Adapted from Winkelmann et al. (2014). CC BY 3.0. Text labels in figure were exchanged by numbers.

2008). The high energy beam transport system (4) directs the ion beams to the treatment rooms. At HIT, two of the three treatment rooms for patients contain a fixed horizontal beam line (5,6). Here, only the patient can be moved relative to the beam. The third room is equipped with a gantry (7), which was the first one for carbon ions worldwide (Haberer et al. 2004). This rotating structure guides the beam around the patient thereby enabling a beam delivery from all around the patient at any angle within the full 360°. The last room (8) is dedicated to experiments. The horizontal beam line in this room was used for all experiments conducted for this thesis.

3.1.2 Beam settings

For all experiments, a static beam directed to the iso-center was used. Different energies were utilized throughout the studies for this thesis. They are listed in the respective sections of the individual experiments.
The focus was consistently set to F4, corresponding to a full width at half maximum (FWHM) of 10.2 – 11.1 mm depending on the initial energy. The intensity was set to I1, the lowest clinically available one. To further reduce the number of particles, a magnet between ion sources and linear accelerator was slightly detuned such that we achieved intensities of around $10^4 - 10^5$ particles/s.

For all experiments, a fully ionized helium-4 beam was used. Gehrke et al. (2018a) compared the performance of the detection system in terms of SR and CNR in combination with a proton and helium beam. Helium was found to yield better SR and slightly better CNR at equal dose compared to protons. Simulations revealed that carbon ions performed best in terms of SR, but exhibited worst CNR. Therefore, Gehrke et al. (2018a) concluded helium ions to be the best ion type for the system based on Timepix detectors, which is why all experiments were conducted with a helium beam accordingly (see also section 2.5.2).

3.2 Timepix detector

To detect single ions of the beam, a specialized detector developed at the European Organization for Nuclear Research (CERN) was employed. The Timepix detector of the first generation is a compact hybrid semiconductor pixel detector (for details about these detectors see section 2.3). It consists of a silicon layer and a Timepix chip (Llopart et al. 2007). The electronics chip has 256 × 256 pixels with a pixel pitch of 55 µm in both directions and is connected to the silicon layer via soldering bumps made from tin-lead alloy. This connection is individual for each pixel, enabling a single-pixel readout ASIC. The field of view is approximately 14 mm × 14 mm (Llopart et al. 2007).

The chips of our detectors were thinned down to approximately 100 µm by Advacam s.r.o. (Prague, Czech Republic) in order to reduce their material budget and therefore scattering within the detection system. The thickness of the silicon layer, which is composed of an n-type substrate with p-type implantations, was selected to be 300 µm.

The internal clock of the detector is operated at 10 MHz. Each pixel is provided with its own electronic circuit including a capacitor, pre-amplifier, discriminator and a digital counter (Llopart et al. 2007). The charge created in the depletion zone by the ionizing radiation is collected due to the reverse bias on the capacitor of each pixel. During readout, the capacitor is discharged and the preamplifier output becomes non-zero. The way this output is sampled depends on the measurement mode.

Since each pixel has its own electronic readout, the measurement mode of each pixel can be chosen independently out of four options (Llopart et al. 2007):

- Time over Threshold (ToT)-mode: the counter is increased for each clock tick for which the signal is over threshold. This mode enables the measurement of single particles' energy deposition (see section 3.2.1)
- Time of Arrival (ToA)-mode: the counter is increased for each clock tick after a particle has arrived. Early arrival times therefore correspond to a high ToA. This mode can be used to determine the particles' incidence time
- counting-mode: the counter is increased for each impinging particle. It enables to measure the number of incident particles
- masked-mode: the counter is disabled and no signal is recorded. This mode can be used for noisy or faulty pixels.

Of the named modes, only the ToA and ToT modes were used for the helium-beam radiography experiments, which will be discussed in detail in section 3.3.

The first generation Timepix detectors are operated in frame mode. Thus, after the active time of the detector, the whole pixel matrix is read out during its dead time (Llopart et al. 2007). In our measurements, the frame duration is set to 1 ms causing a dead time of around 30 ms. This frame duration was found to be the trade-off between the best ratio of active time to dead time while keeping detector artifacts, the so-called overshoots, temporally separated from the actual signal (Kroupa et al. 2014, Hartmann et al. 2014, Martišíková et al. 2018). The overshoots are caused by induction effects within the electronics and appear as oscillations in the signal, which can exceed the threshold multiple times and therefore falsify the ToT.

For all detectors, we set a detection threshold of 5 keV, which exceeds the background of the detectors. Since ions deposit way more energy than this threshold, the detector can be operated quasi noise-free for our purposes (Gehrke et al. 2018b). Thus, the efficiency of ion detection is nearly 100 % (Granja et al. 2018) for intensities of up to 10^4 ions/s. For intensities used for the experiments in this thesis ($\approx 10^5$), a detection efficiency of around 90 % is reached due to overlapping signals within the chosen frame time (Metzner et al. 2024b).

3.2.1 ToT-dE calibration

To translate the ToT signal to energy deposition values, calibration curves provided by Advacam were used, which were established following a procedure by Jakůbek (2011). For this purpose, X-ray sources with well-known photon energies are used to irradiate the detector and to measure the corresponding ToTs in each pixel. Through the resulting data points, a fit f following the function (Jakůbek 2011)

$$f(\delta) = \text{ToT}(\delta) = a \cdot \delta + b - \frac{c}{\delta - t} \qquad \text{with } \delta = -\,\mathrm{d}E \tag{3.2.1}$$

is performed. Here, $-\mathrm{d}E$ is the energy deposited by the photons, which is a positive quantity. a, b, c, t are fit parameters, which are determined for each pixel individually to also compensate for the varying behavior of each electronic circuit and inhomogeneities of the detector. Note that the ToT-dE calibration curve is given in its inverse form here due to its more compact form.

These calibration curves were established for X-ray photon energies in the order of 1 keV to 100 keV, whereas ion imaging experiments often involve higher energies. However, the detector's ToT approximately follows a linear behavior within a certain interval of higher energy depositions. In previous work (Gehrke et al. 2017), the calibrations were shown to provide sufficient accuracy for the energy depositions relevant for helium-beam imaging. Furthermore, the calibration curves homogenize the response of the detector since they are established for each pixel individually.

3.2.2 Detection units

The Timepix detectors of the first generation can be stacked on top of each other with a distance of approximately 3.6 mm and up to 8 detectors can be connected to one FPGA-based readout called FITPix (Kraus et al. 2011). In our experiments, we use stacks of two detectors, like shown in a close-up in fig. 3.2. Here, on a motherboard (1), two Timepix detectors (2,3) are mounted together with a protective cover (4). The detectors are air-cooled via a fan (5), which is attached to the motherboard. These stacks of two Timepix detectors will be called a *unit* in the following.

Both detectors within one unit share a readout, which is connected to a Laptop via USB 2.0 connectors. Detectors and readout interface are operated via the proprietary software package Pixet (Version 1.4.7) (Tureček et al. 2011). All named components were purchased from Advacam s.r.o., Prague, Czech Republic.

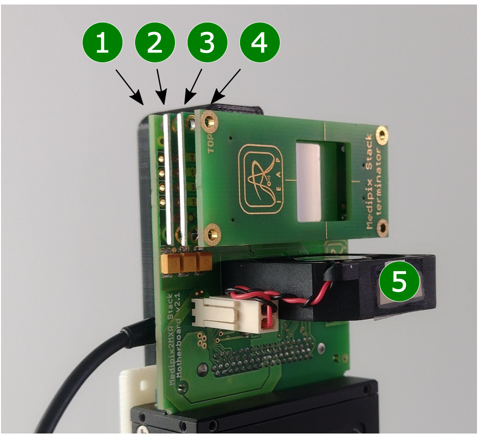

Figure 3.2: Close-up of Timepix detectors of the first generation (Llopart et al. 2007). Each detector consists of a Timepix chip and a layer of silicon, which are connected via bump-bonds. For the experiments conducted for this article, two Timepix detectors (2,3) were attached to a motherboard (1) with a fan (5). On top, a protective cover (4) was mounted with a window of the size of the sensitive area. The detectors including motherboard and cover were purchased from Advacam s.r.o.

3.3 Detection system

For the helium-beam radiography (αRad) experiments, a specialized detection system was used, which was previously constructed in-house (Gehrke 2018, Amato et al. 2020). The aim was to develop a lightweight system. By definition, this decision inhibits the measurement of the commonly assessed residual energy or range to create the image contrast, since a lot of decelerating material is required for these systems (see section 2.5). Instead, the energy deposited within a thin Timepix detector is measured to infer the water-equivalent thickness (WET) of the traversed material (Knobloch et al. 2022). The measurement principle can thus be seen as a probing of the steep rising edge of the Bragg peak where small deviations in thickness or density translate to a large change in deposited energy (Metzner et al. 2024b). Additionally, Timepix detectors are used to track single ions and, in that way, correct for the Multiple Coulomb scattering (Gehrke et al. 2018a).

The system is based on, in total, six Timepix detectors of the first generation (Llopart et al. 2007), which were described in the preceding sections. The detection system, which is shown in fig. 3.3, contains three units and was introduced in this form by Amato et al. (2020). Each of these units consists of a stack of two Timepix detectors (see fig. 3.2). The first unit (A) is the front tracker, the second unit (B) the rear tracker and

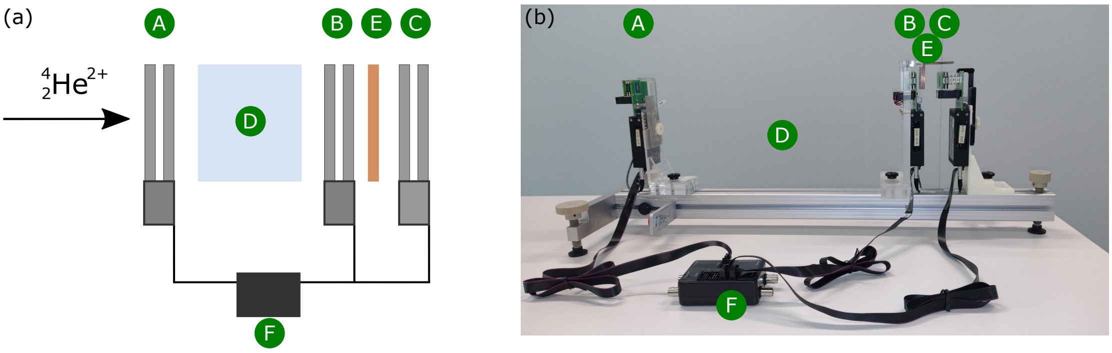

Figure 3.3: Detection system for helium-beam radiography experiments shown in (a) as a schematic and (b) as a photograph. The system contains three units of two Timepix detectors each: the front tracker (A), the rear tracker (B), and the energy deposition unit (C). The object to be imaged (D) is placed between the two tracking units. The energy degrader (E) was included to increase the system's spatial resolution (Amato et al. 2020). The three units are synchronized by the device denoted by (F). Reprinted from Metzner et al. (2024b). © Institute of Physics and Engineering in Medicine. Reproduced with permission. All rights reserved.

the third unit (C) the energy deposition unit. The object to be imaged (D) is positioned between the two trackers. Between the last two units, an energy degrader made from copper (E) is included. Designated hardware (F) handles the synchronization of the three units.

The energy deposition measurement is conducted by means of the first detector within the energy deposition unit (C), which is the only detector operating in ToT mode. On this fifth Timepix detector in the beam line, single ions leave different energy depositions depending on the material they traversed, resulting in different measured ToT. The ToT can then be translated to energy deposition values (Jakůbek (2011), see section 3.2.1) and subsequently to WET (Knobloch et al. (2022), see section 3.8.1). Of course, this measurement principle works most precisely in the steep rising edge whereas the precision decreases if the measurement is conducted in the plateau region of the dose-depth curve (Metzner et al. 2024b). The method used to ensure the steep rising edge to be reliably positioned on the fifth detector is outlined in section 3.8.

The tracking units are employed to estimate the path of each single ion within the object to be imaged. The four detectors within these units are run in ToA mode. Due to the synchronization, temporal coincidences can be utilized to find the signal of one ion on these detectors of the two tracker units. The center-of-mass coordinates of the hit pixels can be used to determine the impact position (Gehrke et al. 2018a). If both measurements per unit are considered, also the ion's direction of motion can be estimated. How the position and direction in front and back of the object to be imaged can be used to correct for scattering of the ions will be described in detail in section 3.4.

To also match the signals on the detector measuring ToT with the ones on the other five detectors, the very last detector is operated in ToA as well. Due to the close proximity, the ToT detector responsible for the image contrast is matched spatially to this detector (Amato et al. (2020), see section 3.4).

All detectors are operated partially depleted at around 7.4 V since Gehrke et al. (2017) found pronounced saturation effects for ion hits on fully depleted sensors. Because the ToT of partially depleted detectors is especially sensitive to bias voltage fluctuations, the last detection unit is operated with an external power supply (RS-3005P, RS PRO, UK).

The energy degrader (thickness of 5.45 mm) was included by Amato et al. (2020) due to two reasons: to increase the spatial resolution of the system and as an additional precautionary measure. The improvement in terms of spatial resolution is due to the higher initial beam energies which must be used in order to compensate for the extra material of the energy degrader and to ensure that the fifth detector is still positioned on the steep rising edge of the Bragg peak. Since higher beam energy means overall higher ion velocities, scattering within the object to be imaged is reduced and spatial resolution thus increased (see section 2.1.2). Additionally, the energy degrader constitutes extra material between the Bragg peak measured at the last detection unit and the patient. Therefore, small inaccuracies in the choice of initial energy cannot lead to an accidental positioning of the Bragg peak within the patient (Amato et al. 2020).

3.4 Data processing

In order to obtain a radiograph from the measured data, several post-processing steps are required, which were previously established gradually in Gehrke (2018), Amato et al. (2020), Knobloch et al. (2022), Metzner et al. (2024b). The data processing workflow, which was implemented in C++ and MATLAB[1], is depicted in fig. 3.4 and will be described in the following.

The data received from the Pixet software contains the pixel coordinates of the hit pixels and the corresponding ToT or ToA. Within the Pixet software, the pixel data measured by the Timepix detectors is already grouped into clusters. Within one line of the output, the data caused by the charge cloud of one hit is provided.

---

[1] MATLAB (23.2.0.2485118 (R2023b) Update 6, Natick, Massachusetts: The MathWorks Inc.)

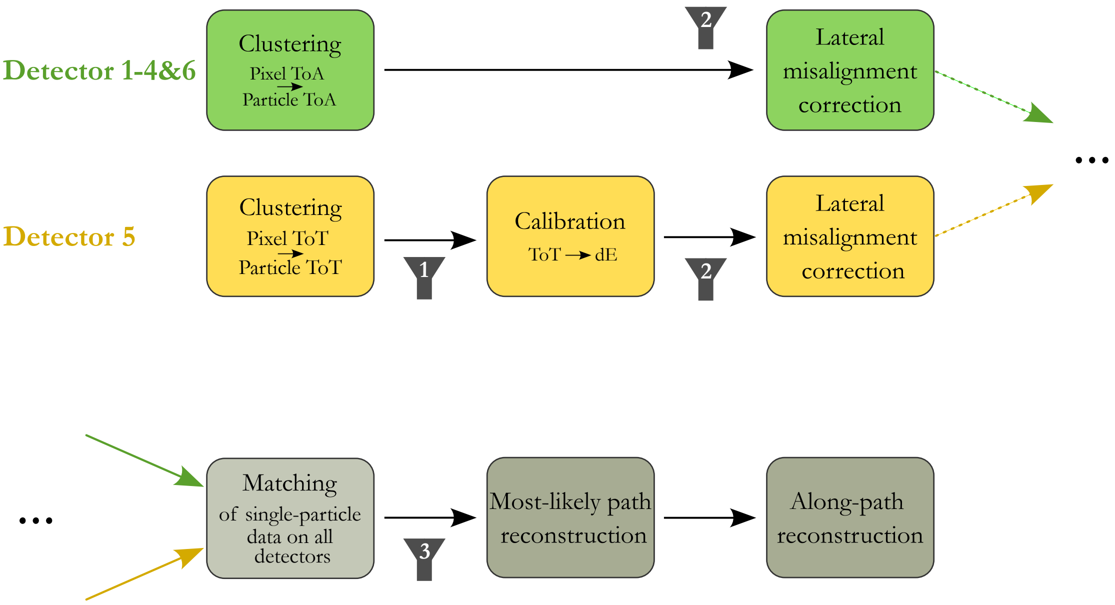

Figure 3.4: Data processing flowchart. Several steps are conducted for all helium-beam radiography experiments. First, the data is clustered. Then, the ToT data measured on detector 5 is converted to energy deposition. The position coordinates on all detectors are then corrected for lateral misalignment. Afterwards, the data of all detectors is matched based on temporal coincidences (detectors 1-4, 6 amongst each other) and spatial proximity (detector 5 with 6). Based on the tracking information, the most likely path within the phantom is calculated. Lastly, a radiograph can be created with the along-path reconstruction. Details about the filtering steps are provided in the main text. Reprinted from Metzner et al. (2024b). © Institute of Physics and Engineering in Medicine. Reproduced with permission. All rights reserved.

Subsequently, three steps follow which are only applied to detector five. Clusters with several distinct maxima are omitted since they are assumed to stem from overlapping hits which cannot be easily separated due to the lack of time information on this detector (Gehrke et al. 2017). Next, energy deposition values are derived from the ToT values measured by detector five (see section 3.2.1). A histogram binning the data according to the number of pixels per cluster and the integrated cluster signal is used to identify contributions of different ion types (Hartmann et al. 2017, Gehrke et al. 2018b). In this histogram, secondary fragments and signals caused by unwanted detector effects are filtered.

On the first five detectors, hits within 1 mm from all four edges are discarded to omit spatially cropped clusters. Additionally, data from the two corners of the detector where an extra layer of material is mounted at the back is excluded. The ions which hit these corners traversed more material than the others and therefore skew the data if not discarded (Metzner et al. 2024b).

In the next step, the coordinates on all detectors are corrected for lateral misalignment of the detectors in the experiments (Aricò et al. 2017). For this purpose, one additional data set is acquired without any imaged object for each initial energy. The resulting data is then analyzed by means of histograms showing relative single-ion shifts between the detectors. By finding the x- and y-coordinates of the maxima in the histograms for all detectors, the alignment vectors are extracted and applied to all following data (Metzner et al. 2024b).

Afterwards, the data of all five detectors operated in ToA-mode is matched temporally by searching for coincidences in a window of at most 400 ns (Gehrke et al. 2018a, Amato et al. 2020). Since detector 5 measures ToT, it cannot be matched temporally. Due to its close proximity to detector 6, it is spatially matched to this detector (Amato et al. 2020): Within a radius corresponding to 3σ of the angular spread within the back tracker, but at least 14 px, clusters are searched for. If no cluster or several clusters are found within the radius, the clusters are omitted to prevent mismatches.
In a last filtering step, the ions which arrived within the last 200 µs of a frame are discarded to exclude ions with a ToT which was incompletely read out (Gehrke et al. 2017).

Based on the tracking information the direction vectors $\hat{\mathbf{P}}_0$ and $\hat{\mathbf{P}}_1$ in front and back of the phantom can be determined. These are used to extrapolate the single-ion tracks from the measured positions on the detectors towards the surface of the phantom assuming the scattering within air to be negligible. In that way, the position vectors at the front and back surface of the phantom $\mathbf{X}_0$ and $\mathbf{X}_1$ can be obtained. Together with the direction vectors at the surfaces, they are used to estimate the most likely path (MLP) (Schulte et al. 2008) of each single ion based on the cubic-spline path formalism of Collins-Fekete et al. (2015, 2017b), which is described in the following. We utilize the parametrization of the curve $\mathbf{S}(t)$ within the phantom (Collins-Fekete et al. 2015)

$$\mathbf{S}(t) = (2t^3 - 3t^2 + 1)\mathbf{X}_0 + (t^3 - 2t^2 + t)\mathbf{P}_0 + (-2t^3 + 3t^2)\mathbf{X}_1 + (t^3 - t^2)\mathbf{P}_1\,, \tag{3.4.1}$$

where $t \in [0, 1]$ is the parameter varying between 0 (front surface) and 1 (back surface). To consider factors influencing the amount of scattering, Collins-Fekete et al. (2015) modified the direction vectors in this equation

$$\mathbf{P}_i = \hat{\mathbf{P}}_i \cdot \Lambda_i \cdot |\mathbf{X}_1 - \mathbf{X}_0| \quad \text{with} \quad i \in \{0, 1\}\,. \tag{3.4.2}$$

These modified vectors scale with the distance between front and back surface to account for the fact that ions can deviate laterally by a greater extent in thicker phantoms. Furthermore, the scaling factor Λ_i is included for which Collins-Fekete et al. (2015)

found an optimized solution by means of simulations

$$\Lambda_i^{\text{opt}} = A_i + B_i \left(\frac{\text{WET}}{R}\right)^2 \qquad i \in \{0, 1\} \tag{3.4.3}$$

with the parameters $A_0 = 1.01$ $A_1 = 0.99$ and $B_0 = 0.43$ $B_1 = -0.46$. According to eq. (3.4.3), Λ scales with the traversed material relative to the remaining range R. If this fraction is close to one, the direction vectors at the front surface of the phantom get a higher weight than the ones in the back which accounts for the increase in scatter close to the end of the range. If the traversed WET is much less than the range, the two direction vectors are weighted more evenly (Collins-Fekete et al. 2015).

After the path reconstruction, the available data per single ion consists of an energy deposition value in combination with the path estimate, which corresponds to a curve in 3D space. In order to obtain a 2D image, two different approaches are used in this thesis: the plane-of-interest binning (PIB) and the along-path reconstruction (APR).

Following the plane-of-interest binning (PIB) approach (Schneider and Pedroni 1994, Rit et al. 2013, Volz et al. 2020a, Gehrke et al. 2018a), all path estimates are evaluated at a certain depth and the energy deposition values are binned according to their lateral position there. The remaining path information is lost with this reconstruction. However, PIB can be useful if one has prior knowledge of the depth at which a feature should be positioned. Moreover, the PIB will play a major role for the 2.5D imaging approach described in section 3.10.

If a radiograph, which contains the information of the whole path estimate, is of interest the along-path reconstruction (APR) can be employed (Gehrke et al. 2018a, Collins-Fekete et al. 2016). For this approach, 50 PIB images are reconstructed at equally spaced distances over the whole depth of the phantom. Afterwards, the mean over these 50 images is calculated. In that way, an image with lower noise, but worse spatial resolution is obtained compared to the PIB images (Collins-Fekete et al. 2016, Gehrke et al. 2018a).

3.5 Stitching

In order to obtain images larger than the sensitive area of the detector (14 mm × 14 mm), the imaging area can be segmented into smaller sub-regions, which are called regions of interest (ROIs) in the following. These ROIs, which have a size of 12 mm × 12 mm in order to ensure 2 mm overlap between neighboring regions, are arranged in a grid over the whole imaged region. The ROIs are then imaged successively.

For this purpose, the object to be imaged is placed on a translation stage (OWIS, Staufen, Germany) which is positioned such that the two linear stages (LTM120-300-HSM) move orthogonal to the beam axis. After the data acquisition with a certain region of interest (ROI) being positioned between the tracking units, the phantom can be moved with the translation stage by 12 mm along one of the lateral axes. In that way, the imaged region can be sampled piece by piece while ensuring an overlap at the ROIs' edges of 2 mm.

To combine the data of these successive acquisitions, the tracking information is displaced by the coordinates of the respective ROI within the grid and all data is combined into one large file. Then, the post-processing chain is followed in the exactly same way as described in section 3.4 for a single ROI. This stitching method was introduced in Metzner (2022), Metzner et al. (2024b).

3.6 Dose estimation

To estimate the dose of our images in a simple way, we employ the calculations presented in Amato et al. (2020). Here, the dose D per ROI was determined as

$$D = \frac{N D_{\mathrm{ion}}}{\eta_{\mathrm{M}}\,\eta_{\mathrm{T}}} \tag{3.6.1}$$

where N is the number of particles in the final image, while η_{M} and η_{T} are the matching and transmission efficiency. These numbers can all directly be obtained from the measured data.

For D_{ion} we use the value stated in Amato et al. (2020) (table 2) who determined it by means of Monte Carlo simulations. Since we can have a slightly different target thickness and composition, we incorporate this in the uncertainty interval of this quantity, such that we obtain $D_{\mathrm{ion}} = (1.7 \pm 0.4)$ nGy. If several ROIs are combined into one larger image, the average dose over all ROIs is calculated.

This calculation does not take into account the dead time of the detector. To not extensively strain the accelerator magnets, we leave the beam on during the dead time of the detector. As the beam could be synchronized with the detector, and Timepix3 and 4 (Poikela et al. 2014, Llopart et al. 2022) do practically not have any dead time, it is more reasonable to report the dose during the active time of the detector as is done throughout this thesis.

3.7 Scatter investigation

This section is based on Metzner et al. (2024a).

When ions interact with matter they are deflected nearly continuously along their path due to electromagnetic interactions with the target nuclei. This process is called Multiple Coulomb Scattering (see section 2.1.2).
Some ions collide with the target nuclei which results in large scattering angles. Since these events can be inelastic, they are often also connected to large energy losses.
An often-used approach to filter large scattering events is applying a threshold on the difference angle between the ions' incident and exiting direction (Schulte et al. 2008). In our group, we decided to filter based on the track length L of the ions instead to take into account all tracking information thereby also including the entry and exit positions (Metzner et al. 2024a). Generally, the track length L can be determined as

$$L = \int_0^1 |\mathbf{S}'(t)| \mathrm{d}t \tag{3.7.1}$$

or for our case with N evaluated discrete depths within the phantom (Metzner et al. 2024a)

$$L = \sum_{n=2}^{N} \sqrt{(\Delta S_{x,n})^2 + (\Delta S_{y,n})^2 + (\Delta S_{z,n})^2}\,, \tag{3.7.2}$$

$\Delta S_{x,n}$ and $\Delta S_{y,n}$ describe the spatial deviations of the curve parametrization (see section 3.4) orthogonal to the beam. $\Delta S_{z,n}$ describes the difference in depth. Since we evaluate the path at equidistant points, $\Delta S_{z,n}$ is the same for all n depths.

The filtering of scatter based on the track length is studied in section 4.1. In the post-processing chain, it was introduced between the path calculation and the reconstruction of the final image by means of the PIB or APR.

3.8 Energy painting

This section and its sub-sections are based on (Metzner et al. 2024b).

The use of lightweight and compact detectors for ion-beam radiography is connected to a challenge, which is schematically depicted in fig. 3.5.
In fig. 3.5(a), a homogeneous object with two steps is imaged by means of a thin detector. Tracking detectors are omitted in this example since they are not relevant for

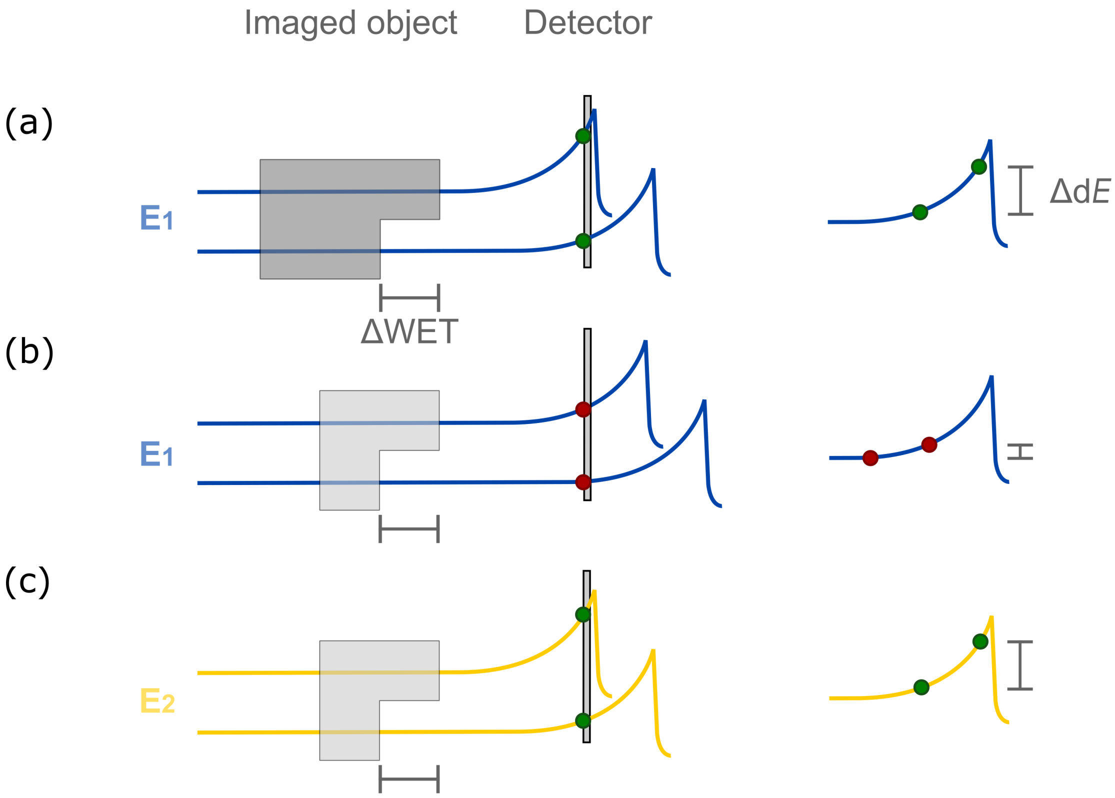

Figure 3.5: Motivation for the energy painting method (Metzner et al. 2024b). (a) The energy deposition dE on a thin detector can be measured to infer the traversed WET. A difference in thickness ΔWET, translates to a difference in energy deposition ΔdE. A high precision is reached in the steep rising edge of the Bragg peak of a beam with an initial beam energy E_1. (b) If the same initial beam energy is used to image an overall thinner object, a measurement in the plateau of the depth-dose curve causes a low-precision. (c) By decreasing the initial energy to E_2 according to the expected lower WET of the object, the high precision is restored. Thus, the idea of the energy painting method is to adjust and combine several initial beam energies for high-precision imaging over a wide WET range.

the following considerations. Ions with the energy E_1 crossing the different steps of the phantom traverse a different amount of WET, which is why they deposit a different amount of energy on the detector. In the scenario in fig. 3.5(a), the difference in deposited energy ΔdE is high.

In fig. 3.5(b), an overall thinner object with the same difference in thickness ΔWET is imaged. The ions with the same energy as in fig. 3.5(a) deposit a lower energy on the detector. Additionally, the difference in energy is smaller because the measurement is conducted in the plateau region of the dose-depth curve of these ions. The initial energy E_1 thus cannot be used to image any object with a high precision.

In fig. 3.5(c), the solution is presented: the use of a lower initial beam energy $E_2 < E_1$ for the thinner object. In that way, the measurement is conducted in the steep rising edge again and the precision is restored. If an object exhibiting all three stairs is to be imaged, this implies the use of both energies for the respective transitions. The idea of the energy painting method therefore is to tailor the initial beam energy to the expected WET (Metzner et al. 2024b). For complex, heterogeneous objects this can also involve the use of multiple beam energies for high-precision imaging[2].

By means of this example, requirements for the energy painting methodology can be stated:

- **Calibrations:** Due to the use of the different initial energies, combining the energy deposition images directly would result in discontinuities. Thus, a translation to WET values, which are independent from the initial energy, is required to facilitate a combination within one coherent image.
- **Determination of high-precision WET intervals:** For each initial energy a WET interval must be determined which is suitable for high-precision imaging.
- **Prior WET estimate:** Prior knowledge about the expected WET of the imaged object is needed to choose the optimal energies.
- **Combination:** A method for combining the data acquired with different energies within one image is necessary.

The third point, addressing the prior knowledge of the expected WET, can be solved by the use of X-ray imaging modalities. Since a planning CT is available for each patient in clinical conditions, a WET estimate could be obtained from it. Therefore, also for our energy painting experiments, we acquire an X-ray CT of our phantoms beforehand following the foreseen clinical workflow. For details regarding the WET determination based on CT scans, please refer to section 3.9.2.

While the third prerequisite can be fulfilled by utilizing X-ray CT modalities, the other three requirements necessitate methodological considerations on our part. These will be addressed in the following. Additionally, in the very end of this section, the methodology for the thorough experimental assessment of the energy painting approach will be presented.

---

[2] Previously, multiple beam energies have also been employed for calorimeters, range telescopes and flat panel detectors (Dickmann et al. 2021b, DeJongh et al. 2021, Telsemeyer et al. 2012, Sarosiek et al. 2021).

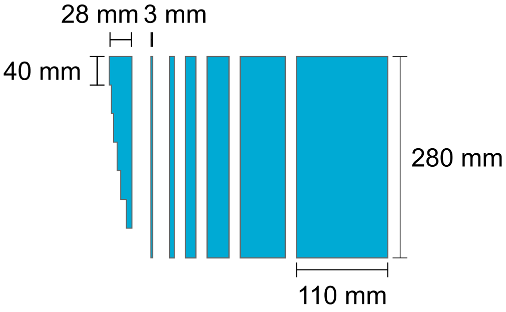

Figure 3.6: Calibration phantom. The PMMA phantom consists of six homogeneous blocks and one part with different thicknesses resulting in a stair shape.

3.8.1 dE-WET calibrations

In order to establish a connection between energy deposition and WET, a dedicated calibration phantom is used. This phantom, which is depicted in fig. 3.6, consists of homogeneous blocks of polymethyl methacrylate (PMMA) with different thicknesses and one special block exhibiting six steps.

The calibration procedure consists of several stages, which are shown in fig. 3.7. In order to enable accurate WET calibrations, the WETs of the different parts of the calibration phantom were determined first (fig. 3.7(a)). This was done in range-pullback measurements with the PTW Peakfinder Water Column (PTW, Freiburg). These measurements are described in detail in Metzner (2022).

Following the procedure of Knobloch et al. (2022), Metzner (2022), different combinations of the parts of the calibration phantom were positioned successively in the beam line. With the fifth detector operated in ToT-mode and the ToT-dE calibration, distributions of single-ion energy deposition values are obtained (fig. 3.7(b)). The mean energy deposition of all ions, excluding the ones on the detector edges, can then be plotted against the WET of the respective parts of the phantom (fig. 3.7(c)). Through these data points, a non-linear least squares fit is carried out (Knobloch et al. 2022, Metzner 2022). The fit function is a modified version of Geiger's law and was further adapted by Bortfeld (1997) as an analytical approximation of the Bragg peak. The functional expression is

$$\mathrm{WET}(\delta) = R - (p\alpha^{1/p}\delta)^{p/(1-p)} \qquad \text{with } \delta = -\,\mathrm{d}E\,. \tag{3.8.1}$$

Since the quantity $\mathrm{d}E$ is the energy lost by the particle $-\mathrm{d}E$ is a positive quantity and directly corresponds to the energy measured by the detector. The parameters p and α are material-related quantities; R denotes the range of the ions.

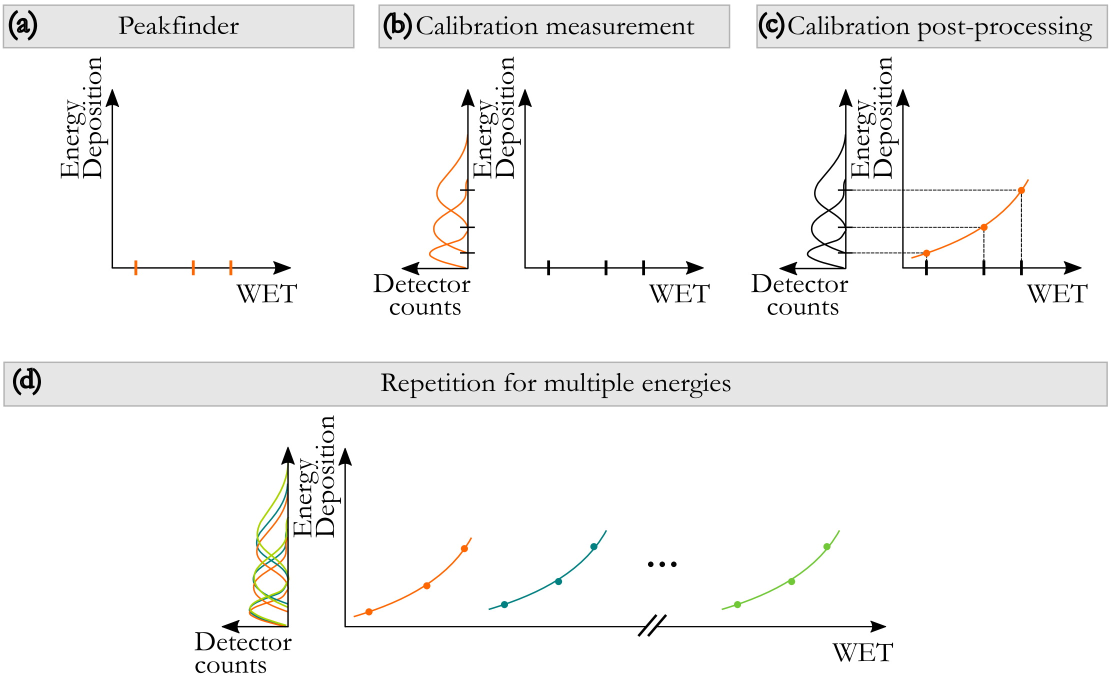

Figure 3.7: Calibration procedure. (a) With range-pullback measurements by means of the Peakfinder water column, the WET values of the phantom are determined. (b) Energy-deposition distributions are obtained if different parts of the phantom are positioned in the beam line. (c) The mean values of the distributions can be plotted against the corresponding WET to obtain calibration points. Through these points, the calibration function following eq. (3.8.1) is fitted. (d) This procedure can be repeated for several initial beam energies to cover a wide range of calibrated WET values. Reprinted from Metzner et al. (2024b). © Institute of Physics and Engineering in Medicine. Reproduced with permission. All rights reserved.

Equation (3.8.1) is a slightly modified version of the one derived by Bortfeld (1997), who used the stopping power $\mathrm{d}E/\mathrm{d}x$ as the variable. Since $\mathrm{d}x$ is the track length within the detector and can approximated to be constant due to the small incidence angles, this quantity is included in our modified parameter α (Metzner et al. 2024b).

The whole procedure can be repeated for several initial energies thereby covering a wide range of calibrated WET values (fig. 3.7(d)). For the energy painting experiments, five energies between 167.80 MeV/u and 206.35 MeV/u with range differences of around 20 mm were selected and calibrated as described.

In order to assess the precision of the calibrations, the mean and standard deviation of the energy deposition distributions μ_e and σ_e are determined after a 3σ cut. The single-ion

WET precision (SIWP) can then be obtained by (Metzner 2022, Metzner et al. 2024b)

$$\mathrm{SIWP} = \frac{\left|\frac{\partial f(\mu_e)}{\partial \mu_e}\sigma_e\right|}{\mathrm{WET}}, \tag{3.8.2}$$

where f is the calibration function of eq. (3.8.1) converting energy deposition into WET. To assess the accuracy, additional probing measurements are conducted. The energy deposition distributions obtained from these measurements are also evaluated regarding their first two moments μ_e and σ_e. The accuracy A can then be calculated through (Metzner 2022, Metzner et al. 2024b)

$$A = \frac{f(\mu_e) + \frac{\partial^2 f(\mu_e)}{\partial \mu_e^2}\frac{\sigma_e^2}{2N} - \mathrm{WET}}{\mathrm{WET}}, \tag{3.8.3}$$

where N is the number of contributing particles. The second term in the numerator originates from the high non-linearity of the calibration function. For a detailed description of the derivation of these formulas please refer to Metzner (2022), Metzner et al. (2024b).

3.8.2 Determination of high-precision WET intervals for initial beam energies

After establishing the calibration curves and assessing their accuracy and precision, suitable intervals for high-precision imaging must be identified as a prerequisite for the energy painting method.
The upper WET limit ensures that we do not measure in the steep falling edge of the Bragg peak where the number of ions which stop before the last detector increases drastically. The upper limit was defined as (Metzner et al. 2024b)

$$\mathrm{WET}_{\mathrm{up}} = 0.98 \cdot R - \mathrm{WET}_{\mathrm{DS}} - \mathrm{WET}_{\mathrm{BL}} \tag{3.8.4}$$

where R is the range of the ions in water, $\mathrm{WET}_{\mathrm{BL}}$ is the WET of the beamline and $\mathrm{WET}_{\mathrm{DS}}$ the WET of the detection system itself.

The lower WET limit is set in order to to avoid capturing readings within the plateau of the depth-dose curve, where the single-ion WET precision (SIWP) is not sufficient. As a criterion, the derivative of the SIWP is required to decrease by no more than one tenth of its value at the upper limit. The lower limit can be calculated as (Metzner et al. 2024b)

$$\frac{\mathrm{d\,SIWP}}{\mathrm{d\,WET}}(\mathrm{WET}_{\mathrm{low}'}) \overset{!}{=} \frac{1}{10}\frac{\mathrm{d\,SIWP}}{\mathrm{d\,WET}}(\mathrm{WET}_{\mathrm{up}}) \tag{3.8.5}$$

To ensure that a WET overlap of at least 5 mm exists between the different energies, the lower WET limit is modified in case this is not guaranteed (Metzner et al. 2024b), such that we obtain

$$\mathrm{WET}_{\mathrm{low}} = \min(\mathrm{WET}_{\mathrm{low}'}, \mathrm{WET}_{\mathrm{up}} - 25) \tag{3.8.6}$$

3.8.3 Combination of data from different energies within one image

Now, that optimal WET intervals are defined for all initial beam energies we can proceed with a selection of the energies suitable for the imaging process. As already discussed, an estimate for the expected WET-distribution is required for this purpose and can be obtained from e.g., X-ray CT modalities. Since the image is assembled from smaller sub-regions (see section 3.5), the WET distributions are evaluated within all ROIs individually. If an overlap between the WET distribution of one ROI and the high-precision WET interval of a calibrated energy is found, this energy is selected for the imaging of that whole ROI.

In that way, mono-energetic images covering different regions of the object to be imaged are obtained. Since the energies are always used for the imaging of whole ROIs, the WET limits described in the previous section are again applied to the obtained mono-energetic images. In that way, we ensure that still only high-precision WET values are further processed.

Due to the overlap in the WET intervals, for a lot of pixels there is an entry in more than one mono-energetic image. How we can combine these within one image is schematically shown in fig. 3.8. If we use several energies E_k $(1 \leq k \leq K)$ for the acquisition of an image consisting of P pixels $(1 \leq p \leq P)$ the final pixel values WET_p can be obtained from the calculation of a weighted mean over all mono-energetic images (Metzner et al. 2024b)

$$\mathrm{WET}_p = \frac{\sum_{k=1}^{K} \mathrm{WET}_p(E_k) \cdot w_p(E_k)}{\sum_{k=1}^{K} w_p(E_k)} \,. \tag{3.8.7}$$

The weight $w_p(E_k)$ accounts for the uncertainty connected to the WETs of the mono-energetic images. It is defined as the inverse of the Poissonian uncertainty (Metzner et al. 2024b)

$$w_p(E_k) = \frac{\sqrt{N_p(E_k)}}{\mathrm{SIWP}_p(E_k)} \tag{3.8.8}$$

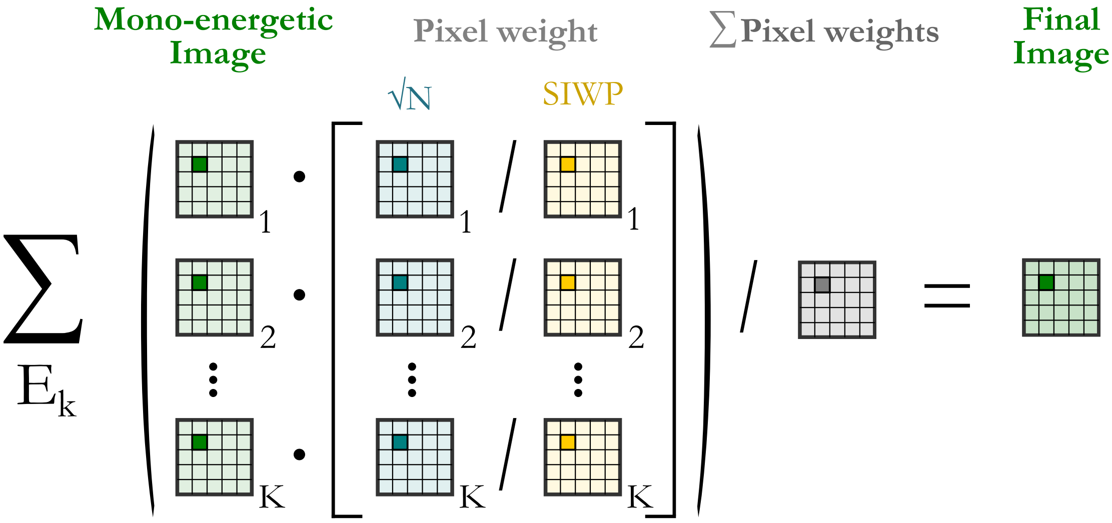

Figure 3.8: Energy painting method. Several mono-energetic images are acquired. To obtain the value for a pixel in the final image, a weighted mean over that pixel in all images acquired with the energies E_k is calculated. The weights reflect the precision connected to the mono-energetic pixel values. They are calculated from the square root of contributing particles N divided by the SIWP of the WET in this pixel. Reprinted from Metzner et al. (2024b). © Institute of Physics and Engineering in Medicine. Reproduced with permission. All rights reserved.

therefore scaling with the square root of the number of particles N and the inverse SIWP. In that way, contributions based on a low number of contributing particles or a high SIWP value are penalized with a lower weight.

3.8.4 Experimental assessment of the energy painting method

To thoroughly assess the energy painting method, a dedicated experiment was conducted. A wedge phantom, made from the same block of PMMA as the calibration phantom (see fig. 3.6) was used for this purpose. It inclines from 0 mm to 200 mm with a slope of one. The remaining dimension has a length of 4 cm.

For this specific experiment, we obtained the WET estimate needed for the energy painting approach not based on a CT. Instead, we employed the measured RSP of the PMMA block and the geometric dimensions of the wedge phantom. This choice was made due to the superior accuracy of the range-pullback measurements and considerations of resource efficiency.

During the experiment, the phantom was positioned such that the direction of incline was aligned with the horizontal axis of the detection system. Within the rows of the image of the wedge phantom in this orientation we therefore expect a constant gradient. If we consider that the geometrical slope is 1, the increase in WET corresponds to the RSP of the material. Along the vertical dimension of the detector (columns), the wedge exhibits a constant thickness. The imaged region with the size of 60 mm × 12 mm covering a WET range of around 150 mm to 220 mm was divided into five neighboring ROIs (see section 3.5).

Due to the use of different initial beam energies and inhomogeneous statistics over the whole image, the SIWP cannot be calculated through eq. (3.8.2) as was done for the calibrations. To facilitate a determination of the SIWP and thus a comparison with the calibrations and other ion imaging systems, an alternative way for the calculation is derived. A detailed derivation[3] is provided in Metzner et al. (2024b).

The fact that a constant WET is expected along the vertical axis can be used to calculate the SIWP separately for each column. Over all pixels p within one column, the weighted mean μ (Metzner et al. 2024b)

$$\mu = \frac{\sum_p \sqrt{N_p}\,\mathrm{WET}_p}{\sum_p \sqrt{N_p}} \tag{3.8.9}$$

is determined. It is used to shift all WET_p additionally to multiplying them with the square root of the number of ions N_p which contributed to the respective pixel. In that way we obtain a new set of pixel values y_p (Metzner et al. 2024b)

$$y_p = \sqrt{N_p}(\mathrm{WET}_p - \mu)\,. \tag{3.8.10}$$

which are corrected for the varying statistics across the pixel columns. This expression together with μ is constructed such that the distribution of y_p is centered around zero. If the standard deviation σ_W of the distribution of y_p is determined, it yields an upper estimate for the SIWP within the column. If the calculation is repeated for all columns, the SIWP over the varying WET of the wedge phantom can be assessed.

The accuracy of the energy painting method was determined exploiting its constant WET gradient which corresponds to the RSP of the material. By conducting a linear fit through the profile of the radiograph, we obtain a value for the RSP, which we can compare with the RSP of the PMMA block measured with the Peakfinder water column. Furthermore, we can assess the residuals of the fit, which can be caused by e.g., the calibrations, the energy painting method or the stitching of the sub-regions. In that way, we can judge the performance of our system and methodology as a whole.

---

[3] conducted by Julian Schlecker

3.9 Imaging of anthropomorphic phantom and comparison to clinical X-ray CT modalities

This section and its sub-sections are based on Metzner et al. (2025a).

After the implementation and validation of the energy painting algorithm, the helium-beam radiography system can be used to image clinically more realistic phantoms. Furthermore, the achieved WET accuracy can be compared to that of well-established X-ray CT modalities. In the following section, the methodology of the respective experiments and their analyses are described.

3.9.1 Reference RSP data set

To be able to compare the performance of the helium-beam radiography system for anthropomorphic phantoms with clinical X-ray modalities, a reference data set representing the true RSP distribution within the phantom is required.
For this purpose, colleagues from Oncoray (Dresden, Germany) shared their data with us, which they previously published in Wohlfahrt et al. (2018). In this publication, they established a ground truth RSP data set of a 731-HN phantom (Proton Therapy Dosimetry Head, Model 731-HN; CIRS, Norfolk, VA). This phantom is composed of materials which are tissue-equivalent for both photons and protons (Computerized Imaging Reference Systems, Inc., Albertini et al. 2011) facilitating a comparison of imaging modalities exploiting both particle types. Together with the data set, we also borrowed the phantom itself from the colleagues at Oncoray for our imaging experiments.

The reference data set of Wohlfahrt et al. (2018) is based on a high-resolution X-ray CT scan (voxel size $(0.5\,\mathrm{mm})^3$), in which they delineated all structures. Furthermore, they conducted range-pullback measurements with homogeneous slabs of the materials used for the construction of the phantom thereby obtaining a ground truth RSP value for all nine occurring materials. They assigned these values to the segmented structures of the high-resolution scan. In that way, they obtained a 3D data set consisting of only nine discrete RSP values. This 3D RSP data set serves as our reference to enable a quantitative assessment of the other imaging modalities described in the following sections.

3.9.2 X-ray imaging

Two X-ray computed tomography (CT) scans of the anthropomorphic head phantom were especially recorded for the study Metzner et al. (2025a) with a SOMATOM

Table 3.1: Parameters used for acquisition of the scans based on single-energy computed tomography (SECT) and dual-energy computed tomography (DECT) (Metzner et al. 2025a)

	SECT-HLUT	DECT-DirectSPR
Tube Voltage	$120\,\mathrm{kV_p}$	$80/140\,\mathrm{kV_p}$
Tube current-time product	165 mAs	248/58 mAs
Collimation	$2 \times 32 \times 0.6\,\mathrm{mm}$	$2 \times 32 \times 0.6\,\mathrm{mm}$
Rotation time	1 s	0.5 s
Pitch	0.55	0.55
$\mathrm{CTDI_{vol}}$ using ∅32 cm	24.9 mGy	11.1/12.7 mGy
Voxel size	$0.9766 \times 0.9766 \times 1.5\,\mathrm{mm}^3$	$0.9766 \times 0.9766 \times 1.5\,\mathrm{mm}^3$

Confidence CT scanner (Siemens Healthineers, Forchheim, Germany): a single-energy computed tomography (SECT-HLUT) scan and dual-energy computed tomography (DECT-DirectSPR) scan[4]. This scanner uses a dual-spiral acquisition technique for DECT scans during which it scans the field of view (FOV) subsequently with two different tube potentials.

Both scans were acquired with clinical head protocols (Longarino et al. 2023), the parameters of which are listed in table 3.1. For the reconstruction of the scans, a Qr40 reconstruction filter with bone beam hardening correction was employed.

Both scans were translated from CTN to RSP values[5]. For the SECT scan a clinically used HLUT was applied (Schneider et al. 1996, 2000, Telsemeyer et al. 2014). For the DECT scan, the proprietary DirectSPR algorithm in the syngo.via software (Siemens Healthineers, Forchheim, Germany) was employed.

3.9.3 Helium-beam radiograph of an anthropomorphic phantom

The region to be imaged was chosen based on several criteria (Metzner et al. 2025a). First, it should contain structures which are often treated with ion-beam therapy, e.g., at the skull base or head and neck. Additionally, it should show many transitions from high- to low-density materials hence constituting a challenging region and yielding the upper limit of achievable accuracy in this comparison. Additionally, the region should

---

[4] The scans were acquired in collaboration with Friderike K. Longarino and Benjamin Ackermann at the Heidelberg Ion-beam Therapy center (HIT)

[5] Conducted by Friderike K. Longarino

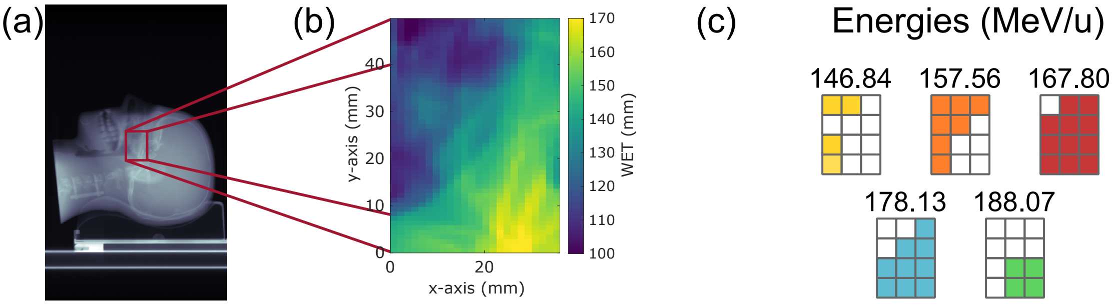

Figure 3.9: Application of energy painting method for imaging of anthropomorphic phantom. (a) Projection of X-ray single-energy computed tomography (SECT) scan, where the imaged region is marked in red. (b) water-equivalent thickness (WET) map of the imaged region based on the SECT scan. (c) The imaged region was divided into 12 sub-regions to make imaging with the detector's limited FOV feasible. For each sub-region, the initial beam energies were chosen depending on the expected WET distribution in (b). Reprinted from Metzner et al. (2025a), CC BY 4.0.

be prone to inter-fractional changes and therefore relevant for daily verification of the patients' anatomy.

Fulfilling all the criteria, a region at the skull base was selected. A beam entering orthogonally from 90° on the left side of the patient was chosen, which is a common geometry for treatments e.g., with opposing beams. The selected region is marked with the red rectangle in fig. 3.9(a) in the corresponding projection of the SECT scan. Because of the cavities, anatomical changes can occur making it an interesting region for frequent monitoring of the patients' anatomy.

Based on the SECT scan, which served as a planning CT for us, an estimate for the expected WET distribution could be obtained, which is shown in fig. 3.9(b). Founded on this, the appropriate imaging energies were selected for the energy painting method. For the respective helium-beam radiography (αRad) experiments with the anthropomorphic phantom, five initial beam energies between 146.84 MeV/u and 188.07 MeV/u were used, which were calibrated in the same way as described in section 3.8.1. To facilitate imaging of regions larger than the detector's FOV (see section 3.5), in fig. 3.9(c), the chosen area is divided into sub-regions. For each region, the WET distribution was estimated based on the WET-map in fig. 3.9(b) and the suiting energies were selected. In fig. 3.9(c), the ROI is marked in the respective color if the energy was used to image that region. Using only a subset of the acquired data allowed to obtain an image with a clinically acceptable dose. The pixel size was set to 0.49 mm × 0.5 mm.

3.9.4 Image registrations and creation of WET-maps

To facilitate a reproducible positioning of the head phantom, metal stickers were attached at the crossing points of the laser positioning system in the CT scanner (Metzner et al. 2025a). These markers were then used to position the phantom for the αRad experiments. Unfortunately, no markers of the high-resolution X-ray CT scan, which the reference is based on, were left on the phantom. Therefore, this data set had to be registered to the SECT and DECT scans.

Separate 3D registrations were conducted in MITK[6], once with the SECT and once with the DECT as target. The similarity metric was based on Mattes mutual information (Mattes et al. 2001), the optimizer on a regular step gradient descent. Because of the higher contrast, the registration was conducted with the data sets in terms of CTN.

Theoretically, both registrations should result in identical transformation matrices as the phantom remained stationary between the SECT and DECT scan. Practically, they yielded a maximum displacement of only 0.1 mm, which can be neglected. Thus, we only proceeded with the reference data set, which was registered to the DECT. The reference scan was interpolated to the volumetric grid of the DECT scan, which is why the reference afterwards also contains interpolated tissue values apart from the nine discrete ground truth RSP values. Additionally, now all 3D modalities have the same voxel size of 0.9766 mm $\times$0.9766 mm $\times$1.5 mm.

To obtain WET-maps for the 3D data sets, all air-filled voxels around the phantom were omitted. Then, the RSP values were integrated along the chosen imaging beam direction which was previously described in section 3.9.3.

The helium-beam radiograph (αRad) was finally also registered to the WET-map based on the reference to correct for a slight mispositioning during the experiment. For this purpose, a 2D image registration by means of the in-house developed MatchPoint software (Floca 2009) was performed. Also for this registration, Mattes mutual information (Mattes et al. 2001) was employed as similarity metric. In this process, the αRad was interpolated linearly to the pixel grid of the reference scan. After the image registration, all WET-maps comprise pixels of size 0.98 mm $\times$ 1.5 mm.

3.9.5 Metrics for image comparison

For the quantitative comparison of the WET-maps based on αRad, SECT and DECT with the reference, different metrics were applied (Metzner et al. 2025a). Within each

---

[6] Medical Information Toolkit (MITK), v2023.12 (ITK 5.3.0, VTK 9.2.6, Qt 5.12.12)

pixel p ($1 \leq p \leq P$), the relative WET difference $\Delta\,\mathrm{WET}$ with respect to the reference R (Metzner et al. 2025a)

$$\Delta\,\mathrm{WET}(p) = \frac{\mathrm{WET}(p) - \mathrm{WET_R}(p)}{\mathrm{WET_R}(p)} \tag{3.9.1}$$

was determined. The distributions of these pixel differences were visualized as histograms and violin plots (Karvelis and oyvindlr 2024).
Additionally, a local gamma analysis was performed (Low et al. 1998, Geurts 2024). The criteria were chosen based on the uncertainty intervals of the reference. Since Wohlfahrt et al. (2018), who established and validated the reference scan, reported 1 mm for the segmentation and 1 mm in range, this translates to parameters of 1 mm and 0.7 % (for the mean WET of around 135 mm). All pixels with a gamma index smaller than 1 agree with the reference within the uncertainties. Gamma indices above 1 indicate a deviation not compatible with the uncertainties of the reference.

To summarize the deviations of the whole image within one metric, the mean absolute percentage error (MAPE) (Metzner et al. 2025a)

$$\mathrm{MAPE} = \frac{1}{P}\sum_{p=1}^{P} |\Delta\,\mathrm{WET}(p)| = \langle|\Delta\,\mathrm{WET}(p)|\rangle \tag{3.9.2}$$

and root-mean-square percentage error (RMSPE) (Metzner et al. 2025a)

$$\mathrm{RMSPE} = \sqrt{\frac{1}{P}\sum_{p=1}^{P} \big(\Delta\,\mathrm{WET}(p)\big)^2} \tag{3.9.3}$$

were calculated. To facilitate an assessment of the uncertainty intervals, the image was partitioned into 42 regions and the MAPE and RMSPE were obtained independently for each of them. The standard error of the mean was then determined as an estimate for the uncertainty.

3.10 2.5D Imaging

This section and its sub-sections (apart from section 3.10.1) are based on Metzner et al. (2025b).

An inherent limitation of radiographs in general is their confinement to two dimensions. Due to the projection along the beam direction, information concerning the depth is not contained in a radiograph. This information can be obtained through either a complete ion CT or estimated from multiple projections, which are, however, connected to additional dose to the patient.

Recently, a Monte Carlo simulation study presenting a technique for the improvement of the spatial resolution of ion-beam radiographs also assessed a method for depth detection based on different reconstructions of single ion-beam radiographs (Volz et al. 2024). How this method works will be explained in the following (Metzner et al. 2025b).

Let us assume the following scenario: We want to acquire an ion-beam radiograph of a simple phantom as it is depicted in fig. 3.10(a). It is a homogeneous phantom with two distinct features in its middle: a blue and yellow one. These features have a different density from each other and also from the rest of the phantom. Thus, ions traversing the blue feature deposit a different energy on our detector compared to the ions passing the yellow one.
In fig. 3.10, four exemplary ion paths are shown which can be calculated based on the tracking information. The paths are colored corresponding to the feature they traverse since we obtain that information in the experiments based on the energy deposition measurement.

Now, we can reconstruct plane-of-interest binned (PIB) images (see section 3.4) meaning that we evaluate all ion paths in a certain depth and assign their WET value to the resulting lateral positions (Schneider and Pedroni 1994, Rit et al. 2013, Volz et al. 2020a, Gehrke et al. 2018a). This process is schematically shown in fig. 3.10(b-c) for three depths, where the depth d_2 in the middle agrees with the position of the blue and yellow feature.

If we have a look at the images with the four entries of the exemplary ions, we can note that the blue and yellow ions in the image at d_2 are well separated. At d_1 and d_3, the ions mix due to their curved paths. If we consider more particles, the spatial resolution of the transition between the two WET values differs over the PIB images (fig. 3.10(d)). It is highest in the image reconstructed at the depth where the features were actually located at. This has been shown in several studies already (Rit et al. 2013, Volz et al. 2020a, Khellaf et al. 2022). Volz et al. (2024) suggested to use the depth of the PIB image with the maximum spatial resolution as an estimate for the location of a feature fig. 3.10(e).

In this thesis, the 2.5D imaging method (Volz et al. 2024, Schlechter 2024, Metzner et al. 2025b) is tested regarding its ability to extract depth information of anatomical changes. For this purpose, we mimicked anatomical changes in simulations and experiments by means of different phantoms, which will be described in the following.

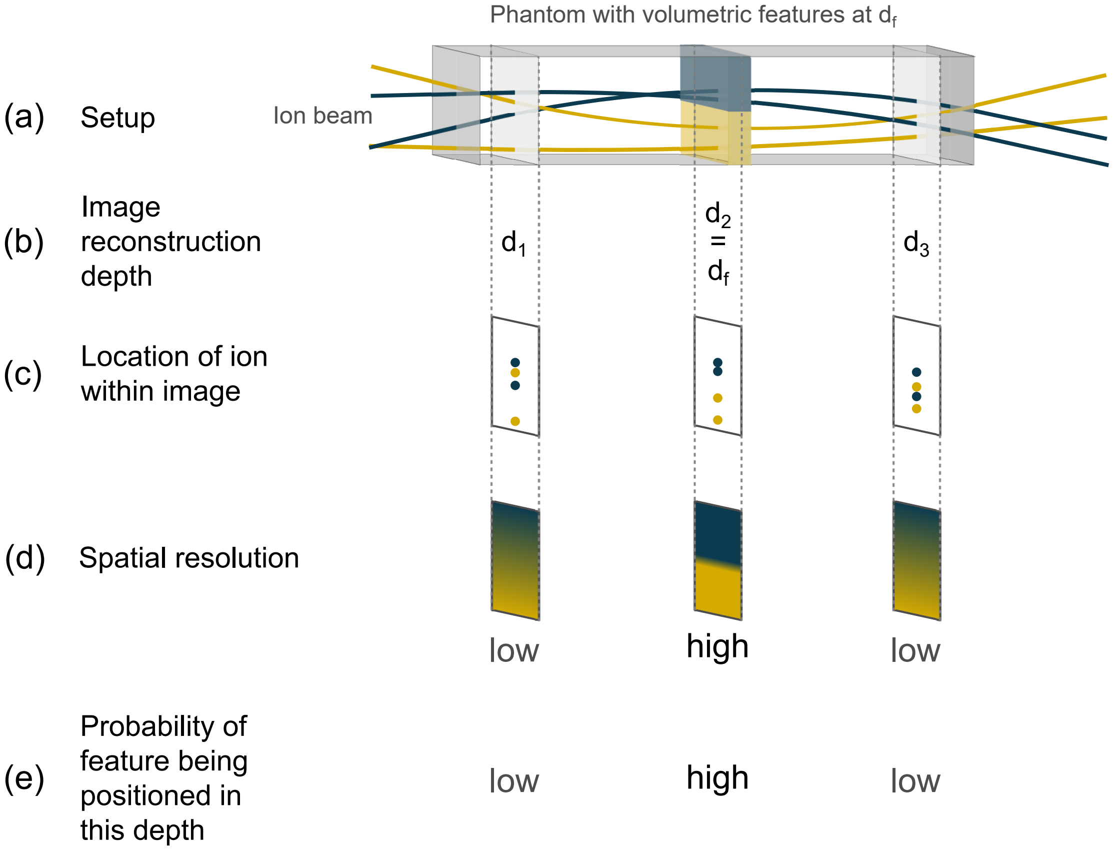

Figure 3.10: Working principle of 2.5D imaging. (a) An ion-beam radiograph of a phantom with two features in its middle (blue and yellow boxes) is acquired with a tracking system. The two features have different densities resulting in a WET difference, which can be resolved by the detector responsible for the image contrast. Furthermore, the most likely path (MLP) of each ion is calculated based on the tracking information. In (a), four exemplary ion paths are depicted and colored corresponding to the feature they traversed. (b) Applying plane-of-interest binning (PIB), images in any depth can be obtained (Schneider and Pedroni 1994, Rit et al. 2013, Volz et al. 2020a, Gehrke et al. 2018a). (c) In order to do so, the ion paths are all evaluated at the depth of interest. The WET value of each ion is then assigned to the pixel corresponding to their lateral position within that depth (Rit et al. 2013, Gehrke et al. 2018a). (d) The image at the actual depth of the features exhibits the highest spatial resolution (Rit et al. 2013, Volz et al. 2020a, Khellaf et al. 2022). In the other depths, the curved ion paths blur the transition between the two features. (e) This maximum in spatial resolution can be utilized to assess the depth of a feature (Volz et al. 2024). Reprinted from Metzner et al. (2025b), CC BY 4.0.

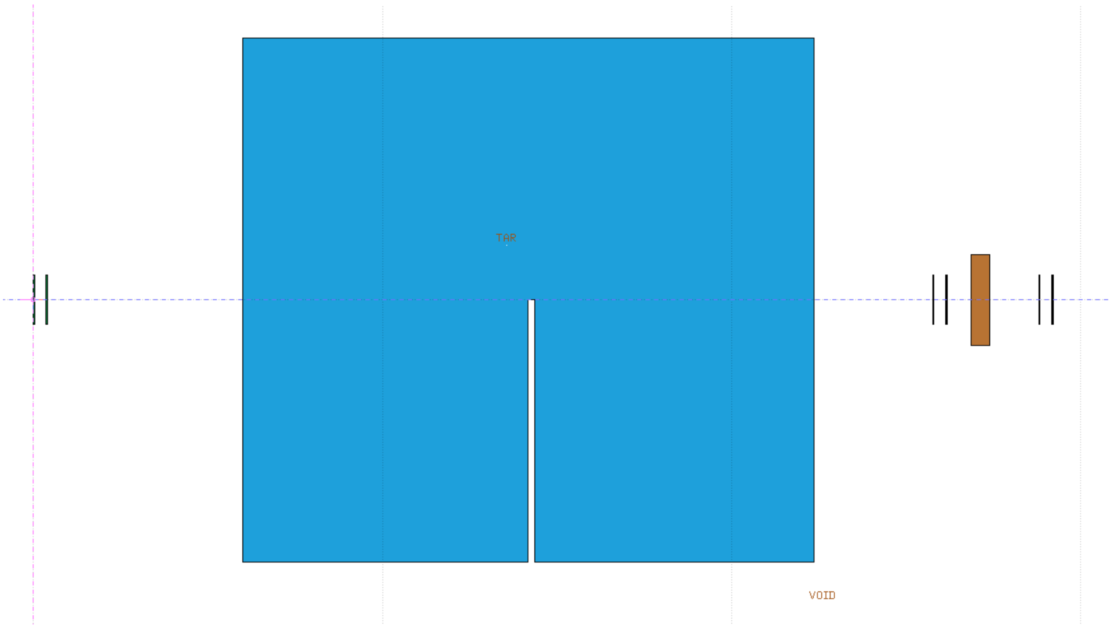

Figure 3.11: Implementation of the experimental setup in Flair, the graphical interface for FLUKA Monte Carlo simulations. The six detectors, the energy degrader and the PMMA phantom were emulated based on previous works of Gehrke et al. (2017, 2018a), Amato et al. (2020), Hermle (2025).

3.10.1 Monte-Carlo simulations of particle transport with FLUKA

At first, the 2.5D imaging method (Volz et al. 2024, Schlechter 2024, Metzner et al. 2025b) was investigated in simulations. In that way, the performance of the method can be effectively compared for protons and helium ions.
The simulations were conducted with FLUKA version 2024.1.0 (Ferrari et al. 2005, Battistoni et al. 2007, Böhlen et al. 2014, Battistoni et al. 2016, Ballarini et al. 2024) and are based on previous works in our group (Gehrke et al. 2017, 2018a, Amato et al. 2020, Hermle 2025). The detection system and the phantom were emulated by means of the graphical user interface Flair version 2.3-0e (Vlachoudis 2009), a screenshot of which can be seen in fig. 3.11. The HADROTHE card was selected loading default parameters for hadron therapy calculations. The FLUKAFIX card was activated to fix the maximum energy loss to 0.5 % per step. Additionally, EVAPORATION and COALESCENCE cards were used to enhance the precision of light fragment generation (Battistoni et al. 2016).

Having the following experiments in mind, the initial beam energy was set to 188.07 MeV/u, the beam's initial momentum spread to 3.11 MeV/c and its position spread to 0.95 cm. A 1.47 mm thin water cuboid at around 1 m before the iso-center was included to emulate the components within the beam nozzle in a simplified way. This cuboid is not included in fig. 3.11 due to the great distance to the rest of the setup.

The implementation of the detectors consists of a 300 µm silicon layer, the 100 µm thin chip and the soldering bonds for all pixels, which were implemented as a mixture of 63 % tin and 37 % lead. The energy degrader was included with a thickness of 5.45 mm. In order to precisely know where the energy was deposited within the detector, the threshold for delta ray production within silicon was decreased to 10 keV.

The Fortran subroutine mgdraw.f was modified in order to extract the information which is measured by the detection system in experiments. The modified routine ensures that the positions of the ions are saved when they enter the sensitive volume of the detectors. On detector 5, additionally the energy of each ion is saved when entering and exiting the silicon layer. In that way, the energy deposited within the detector can be easily calculated. The tracking and energy deposition information was scored without any uncertainties or pixelation. In the mgdraw.f file, only the primary ions were selected and further processed. The mgdraw.f file was compiled with the ldpmqmd linker and activated via the USERDUMP card.

The phantom, which occupies the largest part of fig. 3.11, is a simple PMMA phantom with a thickness of 163.6 mm. One simulation was run with the completely homogeneous phantom to obtain a reference image. Then, a simple change in form of a 1.9 mm air gap was introduced successively at five different depths of 1 mm, 40 mm, 83 mm, 123 mm and 163 mm, referring to the center of the gap, and a separate simulation was performed for each gap position. The aim of this study was to identify these depths by applying the 2.5D imaging method to the simulated data.

The air gap only spanned half of the phantom such that the resulting edge was positioned in the middle of the field of view of the detection system. Additionally, the edge was slightly rotated in the lateral plane such that an angle of 2° with respect to the detectors was obtained. For each depth of the air gap within the phantom, one simulation was performed with protons and one with helium ions.

For the simulated data, the first steps of the post-processing chain described in section 3.4 can be skipped, since clustering, ToT-dE-calibrations, lateral misalignment correction and matching are not required. Also, the filtering steps adjusted to the experiments were left out. Instead, in order to omit ions in the extreme tails of the energy deposition distribution, a 3σ cut was applied.

Starting from the calculation of the MLP, the same routines are applied as to the experimental data. To ensure consistency with the experiments later described in section 3.10.3, the mean number of particles further processed from this point on was set to 110.000 helium ions, which corresponds to the mean number of matched particles within the respective experiments. Consequently, 440.000 protons were taken into account to obtain an approximately equal dose.

For all data sets, PIB images were reconstructed with 1 mm spacing over the depth of the whole phantom. In that way, a stack of PIB images with a pixel size of 0.22 mm × 0.22 mm was obtained for each configuration of the phantom. To extract the anatomical change, PIB difference images were calculated for each reconstructed depth by subtracting the respective reference PIB image without the gap from the PIB image containing the gap. These PIB difference images are the basis for the following analysis.

3.10.2 Slanted edge technique

To determine the spatial resolution of the simulated radiographs, a well-accepted method for spatial resolution determination was used: the slanted edge technique (Reichenbach et al. 1991, Fujita et al. 1992). If a slanted edge is imaged, the position of the edge within each pixel row slightly changes. This shift can be used to displace the pixel rows against each other such that the edge has an angle of 0°. If the pixels are now projected onto one profile, an oversampled edge spread function (OSESF) is obtained. A fit through the data points of this profile can be differentiated with respect to the spatial coordinate orthogonal to the edge to determine the line spread function. If the latter is Fourier transformed, normalized and calculated in absolute terms, we arrive at the modulation transfer function (MTF). Determining the MTF at 10 % contrast finally yields a measure for the spatial resolution (Reichenbach et al. 1991, Fujita et al. 1992).

The slanted edge technique can be unstable for images with low spatial resolution due to large uncertainties connected to the fit parameter determining the angle of the edge. Therefore, this angle was once determined for each experiment in the difference APR image and then set as an input parameter for the following analysis of the PIB images of the data set.

Then, the spatial resolution of the difference PIB images was determined by means of the slanted edge technique for all five experiments with different gap positions (Schlechter 2024, Metzner et al. 2025b). By doing so, we can plot the spatial resolution as a function of depth for all five data sets. In order to smooth that curve, we employ the Savitzky-Golay filter of second order (Savitzky and Golay 1964) with a window size of 11 mm following the methodology of Volz et al. (2024). The 2σ standard deviation within the window divided by the square root of its size provides an approximation of the uncertainty. The depth corresponding to the maximum of the smoothed curve is then determined as the 2.5D estimate for the depth of the anatomical change (Schlechter 2024, Metzner et al. 2025b).

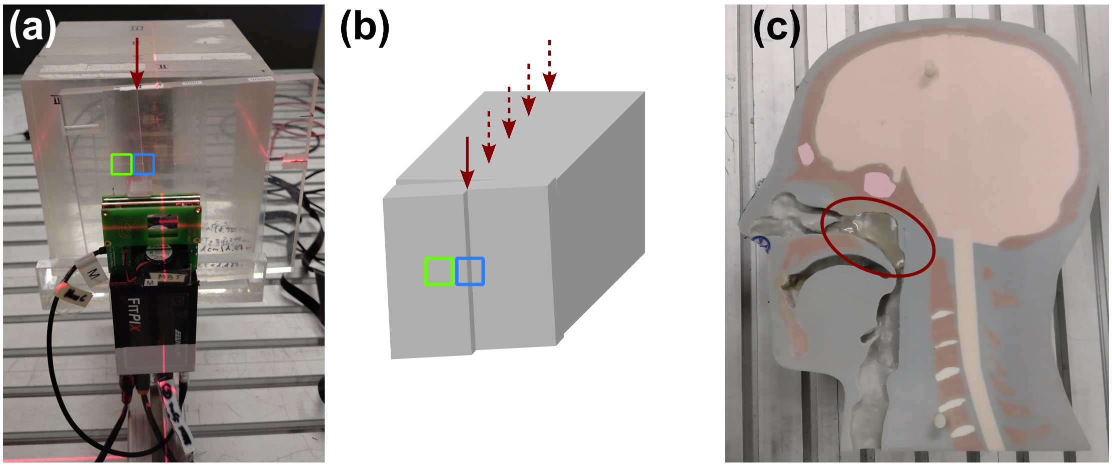

Figure 3.12: Phantoms for testing 2.5D imaging method. (a) Photograph of edge phantom. The edge caused by the thinned-down part is marked with a red arrow. Two different regions were imaged: a homogeneous one (green) and a region containing the edge in the middle (blue). (b) Schematic of the edge phantom. The part with the edge was inserted at five different depths within the built-up material and for each position one radiograph was acquired. (c) Anthropomorphic phantom, which was taken apart such that a silicone piece could be inserted into the nasopharyngeal cavity (Schweins et al. 2025). Reprinted from Metzner et al. (2025b), CC BY 4.0.

3.10.3 Experiments and phantoms

To investigate the 2.5D method in experiments with a helium beam (Schlechter 2024, Metzner et al. 2025b), the physical equivalent to the previously described, simulated phantom was used. A PMMA phantom was employed, which is shown in fig. 3.12 both as a photograph (a) and schematically (b). The phantom consists of several thick blocks of material and a thinner slab, which was partly thinned down by 1.9 mm resulting in a step (red arrow). In total, the thickness of the phantom was measured as (163.60 ± 0.12) mm ((186.50 mm ± 0.15) WET), the thinned-down side as (161.70 ± 0.12) mm ((184.26 ± 0.15) mm WET). Also for the experiments, the edge of the step was slightly rotated in the lateral plane such that an angle of around 2° with respect to the detector's vertical axis was obtained.

We once imaged the full phantom with the thinned-down part outside of the imaged region (green rectangle in fig. 3.12). This is referred to as reference image and mimics the anatomy without any change. The region containing the step (blue rectangle in fig. 3.12) was imaged in total five times. The thinned-down slab represents a simplified anatomical change and is referred to as air gap in the following. The phantom components were re-ordered for each subsequent acquisition resulting in five different depths of the air gap (denoted by dashed red arrows): 1 mm, 40 mm, 83 mm, 123 mm and 163 mm. Also in the experiments, an initial beam energy of 188.07 MeV/u was used.

To further test the 2.5D imaging method for clinically more realistic phantoms, the anthropomorphic head phantom, described in detail in section 3.9.1, was employed. Here, an anatomical change was emulated in form of a silicone piece which was positioned in the nasopharyngeal cavity (red ellipse) (Schweins et al. 2025, Schlechter 2024, Metzner et al. 2025b). Subsequently, the phantom was imaged with an empty and filled cavity using four initial beam energies between 146.84 MeV/u and 178.13 MeV/u such that two energy-painted images were obtained. For the reconstruction of the images, only a subset of the data was considered such that a clinically realistic dose was achieved.

For the insertion of the 6 g of silicone, the phantom had to be taken apart and repositioned afterwards. To correct for a misalignment of the phantom, a 2D image registration between the APR images with and without the insert was conducted. For this purpose, the MatchPoint software Floca (2009) was applied. The determined matrix was then used to transform all PIB images with the silicone insert.

3.10.4 Tenengrad score

As for the simulations, the slanted edge technique was applied to determine the spatial resolution of the experimentally acquired PIB images of the edge phantom. In that way, experiments and simulations can be quantitatively compared in terms of their spatial resolution, but also their 2.5D imaging performance. However, this methodology cannot be applied to anthropomorphic phantoms since these usually do not exhibit clean, straight edges. Therefore, another methodology was benchmarked against the slanted edge technique and finally applied to an anthropomorphic phantom.

The following approach is based on the methodology introduced by Volz et al. (2024). However, it was modified in several aspects (Metzner et al. 2025b). A comparison to the methodology of Volz et al. (2024) is presented in section A.2.

Our methodology was applied to the images of the edge phantom reconstructed with 0.44 mm × 0.44 mm spaced pixels. For the anthropomorphic phantom, a bigger pixel size of 1 mm × 1 mm was used. Since the following methodology is sensitive to noise, two preparatory steps were applied. Firstly, three pixel rows were excluded at all four edges in order to omit noise due to a lower fluence at the edges. Secondly, a median filter[7] (Tukey 1977) was applied to reduce the noise while preserving the edges. For this purpose, a kernel size corresponding to 3 mm × 3 mm was chosen.

Then, the actual determination of spatial resolution based on the Tenengrad score[8] (Tenenbaum 1971, Schlag et al. 1983, Schlechter 2024, Metzner et al. 2025b) followed. The Tenengrad is based on the Sobel operators $\hat{S}_x$ and $\hat{S}_y$ (Danielsson and Seger 1990)

$$\hat{S}_x = \begin{pmatrix} 1 \\ 2 \\ 1 \end{pmatrix} \begin{pmatrix} -1 & 0 & 1 \end{pmatrix}, \qquad \hat{S}_y = \begin{pmatrix} -1 \\ 0 \\ 1 \end{pmatrix} \begin{pmatrix} 1 & 2 & 1 \end{pmatrix}. \tag{3.10.1}$$

If these are convolved with the image I, we obtain the gradients G_x and G_y along both dimensions of the image (Metzner et al. 2025b)

$$G_x(x,y) = \hat{S}_x * I(x,y), \quad G_y(x,y) = \hat{S}_y * I(x,y). \tag{3.10.2}$$

If we now perform an element-wise summation of the squared gradients, we arrive at a measure for the gradient magnitude M within each pixel (Metzner et al. 2025b)

$$M(x,y) = G_x(x,y)^2 + G_y(x,y)^2. \tag{3.10.3}$$

To obtain a metric for the gradient magnitude within the whole image, we can calculate the mean over the entire matrix, such that we obtain (Metzner et al. 2025b)

$$\mathrm{TENG} = \langle M(x,y) \rangle. \tag{3.10.4}$$

This metric, which we refer to as Tenengrad score, serves as a measure for the gradients within the whole image (Schlechter 2024, Metzner et al. 2025b). Hereby, high values imply sharper images.
Analogously to the slanted edge technique, the Tenengrad curve over depth is also smoothed with a Savitzky-Golay filter of second order (Savitzky and Golay 1964, Volz et al. 2024) while using the same parameters and uncertainty estimate.

---

[7] Idea of Patrice Schlegel, personal communication, 26.02.2025. Volz et al. (2024) used a Gaussian filter for de-noising.

[8] Idea of Patrice Schlegel, personal communication with Annika Schlechter, 05.04.2023. Volz et al. (2024) based their method on the Laplacian operator.

4 Results

This chapter presents the main results of the work carried out as part of this PhD thesis. They span from scatter filtering and energy-painted imaging of anthropomorphic phantoms to a first presentation of how the system could be used in clinics for the detection of anatomical changes. The results can be divided into four parts which evolve from more technical and detailed aspects to application-oriented ones, ultimately gaining relevance for future clinical applications:

1. **Scatter filtering**: The impact of ions which experienced a large extent of scattering and a respective filtering threshold is studied.

2. **Energy painting:** As a prerequisite, calibration curves are presented which connect the detector signal (energy deposition) with the clinically relevant quantity (water-equivalent thickness (WET)) of the imaged object. Then, the energy painting method is tested to bypass the limited high-precision WET range of thin detectors. The performance of the energy painting method is assessed quantitatively regarding its precision for phantoms with large variations in WET.

3. **Imaging of anthropomorphic phantom and comparison to clinical X-ray CT modalities:** A helium-beam radiograph of an anthropomorphic head phantom is acquired with the previously established methodology. The WET accuracy of the image is assessed and evaluated against that of clinically used X-ray CT imaging modalities.

4. **2.5D Imaging:** The 2.5D imaging approach, which utilizes multiple Coulomb scattering of ions in matter, is tested for extracting depth information from one helium-beam radiography projection with path-tracking detectors. The chapter is concluded by a demonstration of the system's capability to detect, quantify and localize an anatomical change within a head phantom and therefore presents how the system could be used in clinics.

4.1 Scatter filtering

This section is based on Metzner et al. (2024a).

For X-ray imaging applications, the suppression of scattered photons is a crucial component to obtain images with high spatial resolution (Hoheisel 2006). Ions are nearly continuously deflected by small amounts due to multiple Coulomb scattering with the target nuclei. The impact on the image can be mitigated by the utilization of trackers and the calculation of a most likely path (MLP). However, due to collisions with the target nuclei, ions can additionally experience large-angle scattering events. These events are not considered in the MLP models and therefore their path estimates are connected to high uncertainties. Furthermore, the respective ions lose a lot of energy, which is why they might also influence the quantitative values of the images. Therefore, an investigation of the effect of scattering events on helium-beam radiographs acquired with our detection system is presented within this section.

To gain a clearer understanding of the extent of scattering in our experiments, we can first have a look at our measured data. For this purpose, a data set was chosen which was acquired with a 188.07 MeV/u helium beam impinging on a PMMA phantom with 163.6 mm thickness. At 83 mm depth, an air cavity of 1.9 mm thickness covering one half of the phantom in lateral direction was inserted (see fig. 3.12(a,b)). The effect of this cavity is negligible for the ion paths, but is important to evaluate certain image characteristics by means of the resulting edge at a later stage.
To first judge the magnitude of scattering, we can study the reconstructed path length within the phantom (including the air gap) since this quantity incorporates the positions and angles, so all measured tracking information of the ions.

In fig. 4.1(a), a histogram shows the number of ions for a specific reconstructed path length between front and back surface. For this plot, all ions which passed the post-processing chain and the respective filtering steps (see section 3.4) and therefore contribute to the final image are taken into account.
Most strikingly, no paths shorter than 163.6 mm exist. This number corresponds to the thickness of the target and is the minimum path length which the ions geometrically need to traverse. Furthermore, we see in this histogram that the vast majority of the ions is not deflected by a large extent. More than 99 % of ions deviate by less than 1 mm from the minimum path. This is mainly caused by the bias in our data due to the geometry of our detection system: only ions which were recorded on all the six detectors are taken into account. Most of the ions which scattered with large angles are unlikely to return towards the detection system and are excluded due to their incomplete sampling.
In fig. 4.1(b), the same data is shown in a slightly different histogram. Firstly, the y-axis

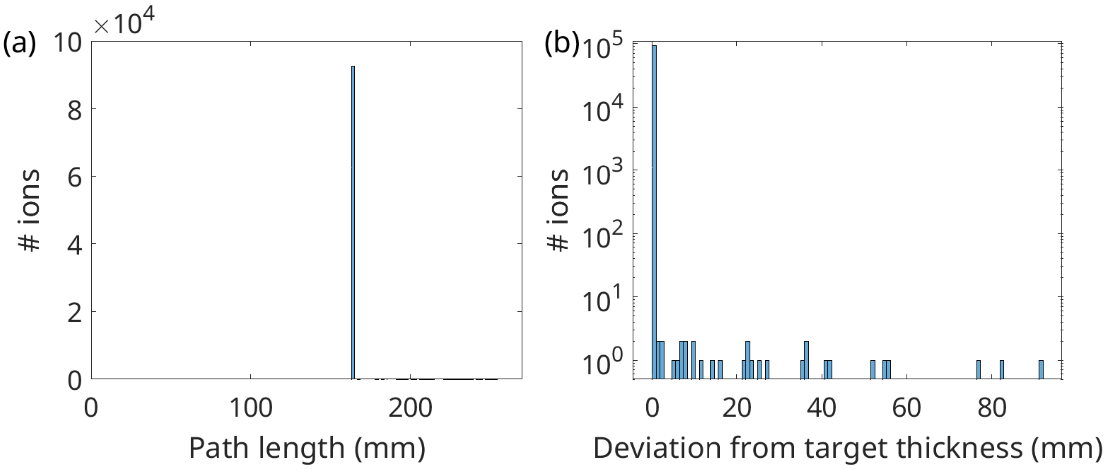

Figure 4.1: (a) Histogram of the reconstructed path length of single ions based on the measured tracking information. (b) The histogram is shown in a modified way: the number of ions is plotted against the deviation of the path length from the minimum (corresponding to the thickness of the target of 163.6 mm). The y-axis is shown logarithmically to also make single contributions visible.

is shown logarithmically to make contributions of ions with larger track lengths visible. Secondly, on the x-axis, the deviation from the target thickness is shown, such that the minimum possible path occurs at 0 mm. In this histogram, it becomes apparent that some ions supposedly travel way longer within the phantom than the vast majority. Even at around 90 mm in the histogram single entries are still observed. According to these reconstructed paths, the corresponding ions travelled around 150 % of the minimum path. The uncertainty connected to these reconstructed tracks with extraordinary length is high. Furthermore, their energy deposition is questionable. Therefore, the aim of the following investigation was to explore the impact of a scatter filtering procedure on the image quality.

In fig. 4.2(a), the helium-beam radiograph corresponding to the data in fig. 4.1 is shown. The other three radiographs in fig. 4.2(b-d) were reconstructed based on different subsets of the data. Here, thresholds of 0.1 % (b), 1 % (c) and 10 % (d) were set as the percentiles of omitted ions with the longest paths. The sensitive area of the detector is marked by a red rectangle. Interestingly, also data outside of the detector area is shown, which is discussed in section 5.1.

If the ions with the longest paths are omitted, it can be seen that the "rays" outside of the red rectangle are reduced drastically. Even if 0.1 % of the ions are filtered out, most of the data outside of the detector's field of view is removed. At 1 % and 10 %, this effect is even more pronounced.

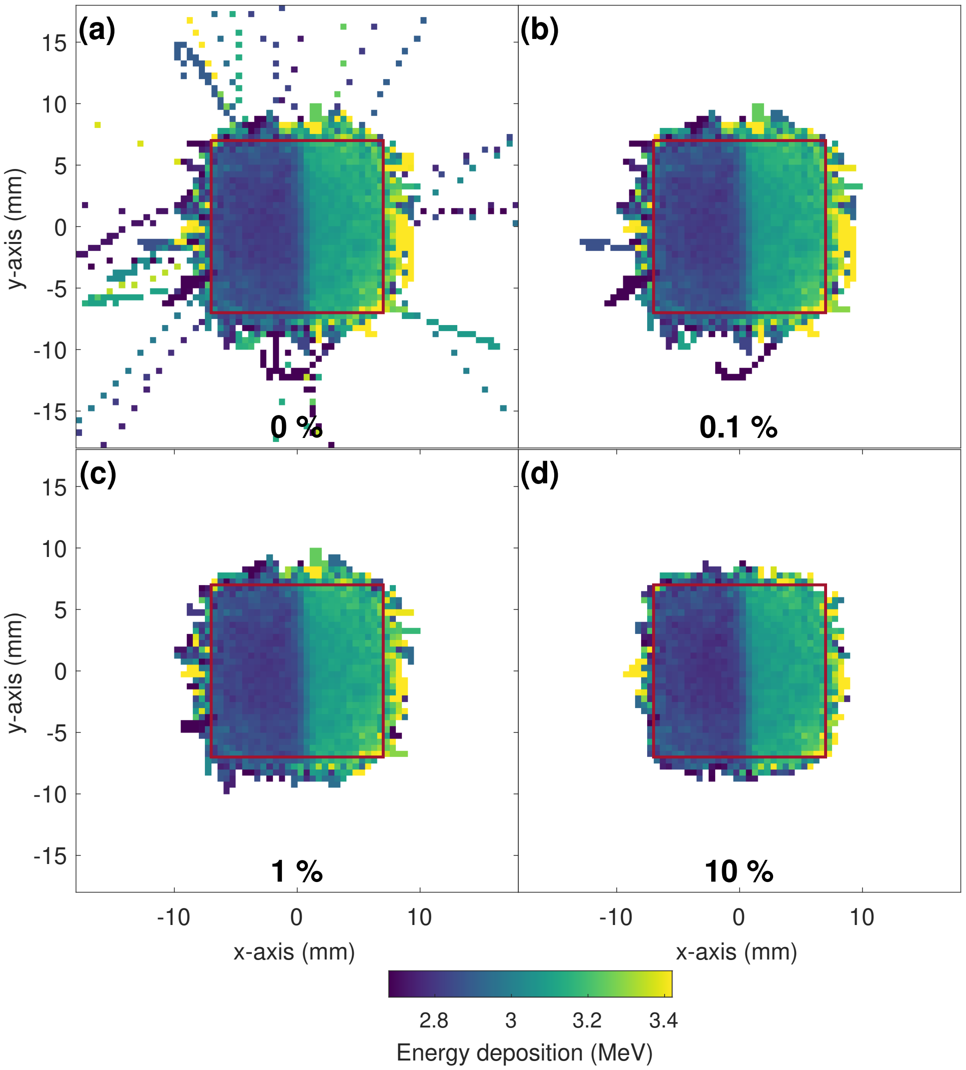

Figure 4.2: Along-path reconstructed (APR) helium-beam radiographs of the edge phantom (see section 3.10.3) reconstructed with different scatter filtering thresholds. The threshold was set to (a) 0%, (b) 0.1 %, (c) 1 %, (d) 10 % omitting the corresponding percentile of ions with the longest paths.

A systematic investigation of the image characteristics with different filtering thresholds is presented in fig. 4.3. Here, the spatial resolution (SR), contrast-to-noise ratio (CNR) and the detector signal are plotted against the filtering threshold. Note that the last two quantities were evaluated in the center of the detector excluding the edges with low statistical power. The corresponding value for the image without any filtering is shown with the dashed gray line in the background.

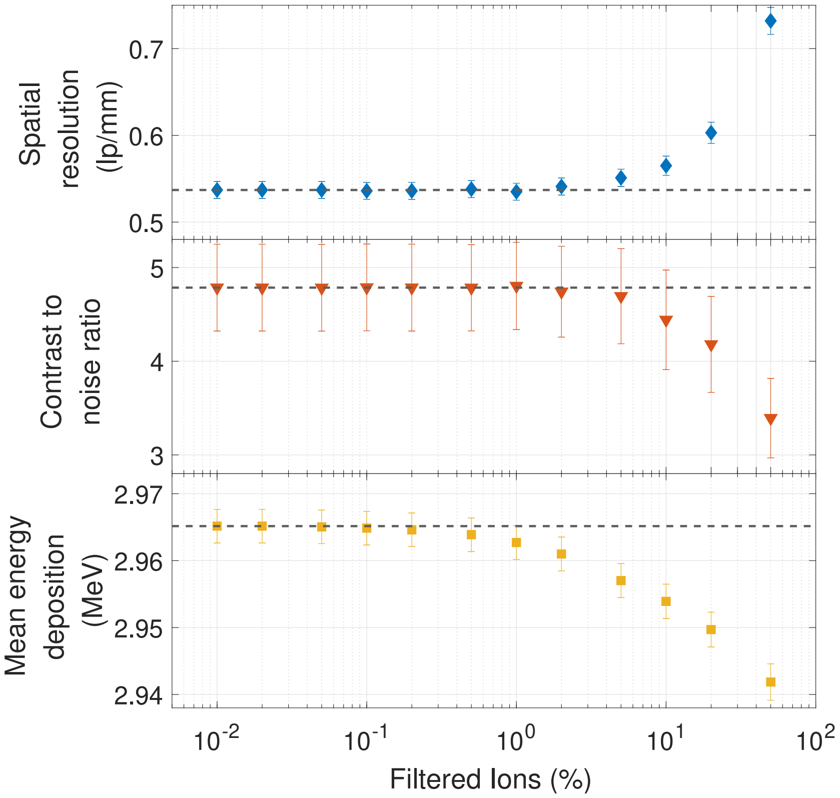

Figure 4.3: Effect of the scatter filtering threshold on image characteristics. (a) The spatial resolution (SR), (b) contrast-to-noise ratio (CNR) and (c) the energy deposition are plotted against the percentage of filtered ions. The corresponding value for the image without any filtering is marked by the dashed gray line.

A clear tendency can be seen in the data: while the CNR and mean energy deposition decrease (i.e. worsen) with increasing threshold, the spatial resolution increases (i.e. improves). All curves have a pronounced plateau for the small filtering thresholds in this logarithmic plot. For the small thresholds, only a small fraction of the data is omitted which in turn does not influence the image characteristic as much as a filtering of e.g., more than 10% of the data.

Since we do not want to compromise on CNR or cause our mean detector signal to become unstable due to the filtering threshold, we decided on a filtering of 1 % of the ions. Consequently, we do not gain much improvement in terms of spatial resolution, the reasons for which will be discussed in section 5.1. However, the CNR at the edges, which was not taken into account in fig. 4.3, is expected to be improved by the filtering due to the behavior in fig. 4.2.

4.2 Energy painting

This section and its sub-sections are based on Metzner et al. (2024b).

The detection system employed in this thesis is based on thin detectors in order to keep it compact and lightweight. To distinguish between different water-equivalent thicknesses (WETs), the Bragg peak is probed by means of these thin detectors. This measurement principle directly implies that only within the steep rising edge does the energy deposited in the detector vary considerably with changes in WET, thereby limiting the WET interval within which high precision can be achieved. The energy painting method was designed to bypass this limitation by utilizing several initial beam energies.

In this section, the energy painting method is experimentally assessed. As a prerequisite, calibration curves for multiple initial beam energies are established. They are then assessed in terms of accuracy and precision and WET intervals for high-precision imaging are identified. Finally, the energy painting method is demonstrated for a wedge phantom by means of which the performance of the methodology can be assessed quantitatively and compared to the monoenergetic approach.

4.2.1 Calibration of detector signal for quantitative WET measurements

To enable the application of the energy painting algorithm (see section 3.8), the helium-beam radiographs must be quantitative in terms of a measure that is independent of the initial beam energy. Only in that way can they be combined into one coherent image. A quantity which is, in very good approximation, independent of the initial beam energy is the water-equivalent thickness (WET) (see section 2.1.1). Furthermore, clinical imaging modalities with the purpose of treatment verification can be interpreted most easily if they show a quantity which can be related to RSP. Since the WET corresponds to the RSP integrated along the beam path, images showing this quantity are valuable for clinical use.

Five calibration curves were acquired for the experimental validation of the energy painting method. In fig. 4.4(a), these curves connecting energy deposition and WET are shown. Following the calibration procedure of Knobloch et al. (2022), for each calibration point a different part of a PMMA phantom with a distinct thickness and an accurately known WET was imaged. The corresponding measured mean energy deposition is plotted against the WET value in fig. 4.4(a), where the uncertainties connected to the two quantities are smaller than the symbols. The trend of the calibration

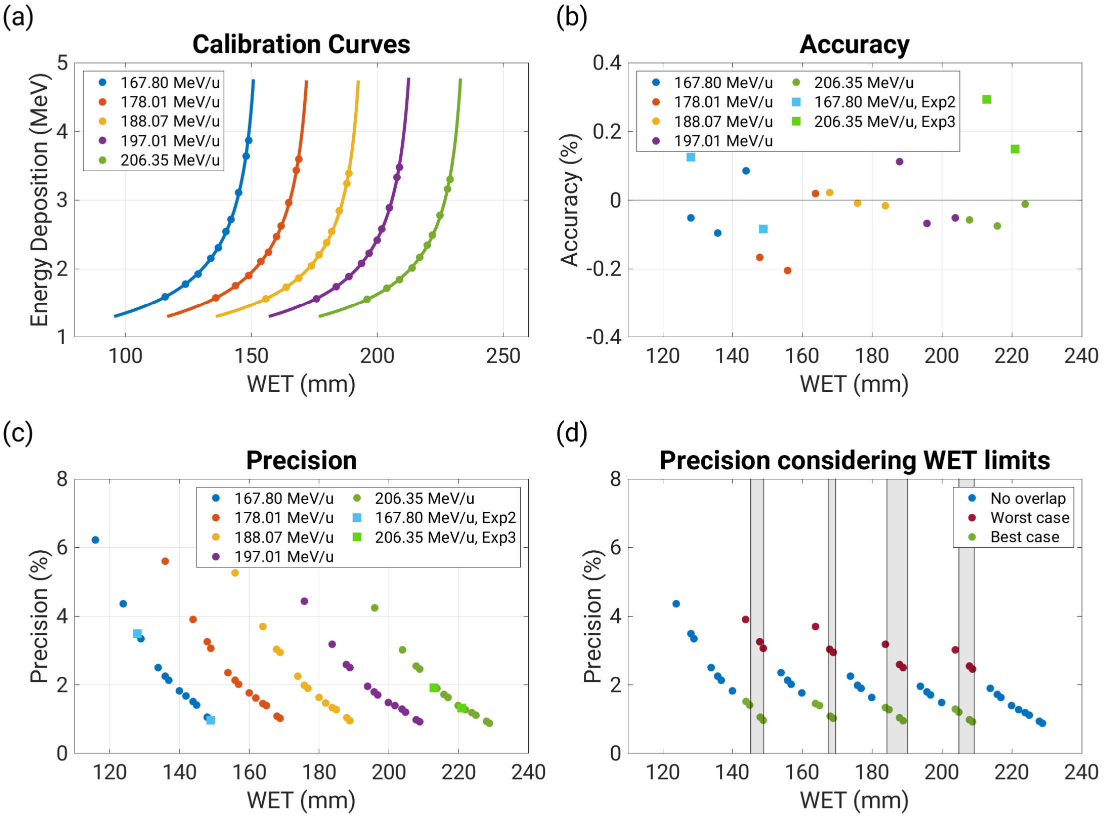

Figure 4.4: Calibration curves and their accuracy and precision. (a) Calibration curves connecting the detector signal (energy deposition) with the clinically relevant quantity (water-equivalent thickness (WET)) are shown as fits to the experimental data (points) for five initial beam energies. (b) Accuracy of the calibration curves for additional measurements that did not contribute to the fit in (a), four with time delay (Exp2 and Exp3). (c) Precision of the curves plotted against WET. (d) Precision considering implemented WET limits. The gray boxes denote WET intervals where two calibration curves can be used for the energy-painting approach. Depending on the energy, best-case precision is shown in green and worst-case precision in red. Blue points denote the intervals where only one curve can be used yielding a distinct precision value per WET. Reprinted from Metzner et al. (2024b). © Institute of Physics and Engineering in Medicine. Reproduced with permission. All rights reserved.

Table 4.1: Fit parameters of the calibration curves shown in fig. 4.4 following eq. (3.8.1) together with their root-mean-square deviation (RMSD). Reprinted from Metzner et al. (2024b). © Institute of Physics and Engineering in Medicine. Reproduced with permission. All rights reserved.

Energy (MeV/u)	R (mm)	α ($\mathrm{mm}^{1-p}\,\mathrm{MeV}^{-p}$)	p	RMSD (mm)
167.80	154.9 ± 0.5	$(3.6 \pm 1.0)10^{-3}$	1.94 ± 0.05	0.20
178.13	176.2 ± 0.4	$(3.1 \pm 0.7)10^{-3}$	1.96 ± 0.04	0.14
188.07	196.1 ± 0.7	$(6.0 \pm 1.9)10^{-3}$	1.85 ± 0.06	0.25
197.01	216.64 ± 0.29	$(3.2 \pm 0.5)10^{-3}$	1.960 ± 0.027	0.10
206.35	236.5 ± 0.5	$(6.1 \pm 1.4)10^{-3}$	1.85 ± 0.04	0.17

points is as expected from theory: the steep rising edge of the Bragg peak is represented by the steep increase in energy deposition for higher WETs.

A non-linear least-squares fit was performed with a function derived by Bortfeld (1997) as an analytical approximation of the stopping power as a function of depth (see eq. (3.8.1)). The resulting parameters are listed in table 4.1 for each of the five initial beam energies. The uncertainties given in table 4.1 correspond to 68 % confidence intervals and were calculated from the square root of the diagonal entries of the covariance matrix. It can be seen that the fit describes the data points very well. The maximum root-mean-square deviation (RMSD) of 0.25 mm also indicates low residuals of the fits.

In fig. 4.4(b-d), the accuracy and precision of the calibration curves are assessed.[1] Keeping the values of both quantities low is the aim within the project and aligns with other ion-imaging approaches focusing on low WET uncertainties.
The accuracy values shown in fig. 4.4(b) seem to be scattered around zero with no apparent trend. Most accuracy measurements were acquired a few minutes after the calibration measurement. Among these, the WET of (155.83 ± 0.10) mm is associated with the highest absolute deviation of (0.20 ± 0.08) % corresponding to (0.32 ± 0.13) mm WET difference to the ground truth value. Two measurements each were conducted 3 and 89 days later to probe the temporal stability of the detection system's energy deposition measurements and the calibration procedure. The maximum accuracy value of these time-delayed measurements, which are designated by Exp2 and Exp3, respectively

---

[1] It is important to note at this point, that accuracy and precision are expressed analogously to an uncertainty following common practice in the community (Bashkirov et al. 2016, Dickmann et al. 2019). Throughout the following, the term *value* is critical: a high accuracy or precision value refers to a numerical measure, and, counterintuitively, a low value denotes better accuracy or precision.

in fig. 4.4(b), is (0.29 ± 0.08) % for a WET of (212.86 ± 0.13) mm corresponding to (0.62 ± 0.13) mm.

In fig. 4.4(c), the precision values of the measurements are plotted against the WET. For all energies, the same trend is visible: a steep decrease of precision values with increasing WET. The minimum single-ion WET precision (SIWP) value of (0.874 ± 0.022) % was achieved for a WET of (228.81 ± 0.14) mm. The maximum precision value reached across all energies was (6.22 ± 0.12) % for a WET of (115.90 ± 0.14) mm.

In fig. 4.4(d), the precision values are shown again while considering the WET limits explained in section 3.8. The transition regions, where two energies can be used to image a certain WET, are marked by gray vertical bars in the background of fig. 4.4(d). The precision points in this region are either marked in green denoting the best-case precision or in red denoting the worst-case precision. If both energies are used, the precision can take on any value in between. Since no precision values were acquired directly at the limits of the overlap regions, the adjacent point of the worst case is also shown to avoid an underestimation of the precision value if a mean for these overlapping regions is calculated later on. It provides a conservative precision estimation in these regions. The WETs for which only one calibration curve is available are marked in blue.

Taking these limits into account, the maximum precision value can be decreased to (4.37 ± 0.06) %, which is now reached for a WET of (123.84 ± 0.16) mm. Meanwhile, the minimum precision value remains constant compared to fig. 4.4(c). Thus, an overall better precision is reached if the WET limits are taken into account and the energies are changed according to the expected WET. This will be utilized in the next section.

4.2.2 Experimental assessment of the energy painting method

This section shows the experimental results of the energy painting method which was designed to circumvent the limitation of an ion-imaging system exclusively based on thin detectors: the limited WET range where high-precision imaging is possible. To assess the performance of the approach in a well-controlled setup, the simplest phantom exhibiting a large WET range was used: a wedge phantom with a constant WET gradient.

The region containing WETs of around 150 mm to 220 mm was imaged twice: firstly, with only one initial beam energy and secondly, with multiple energies tailored to the expected WET distribution within each ROI the image is assembled from (see

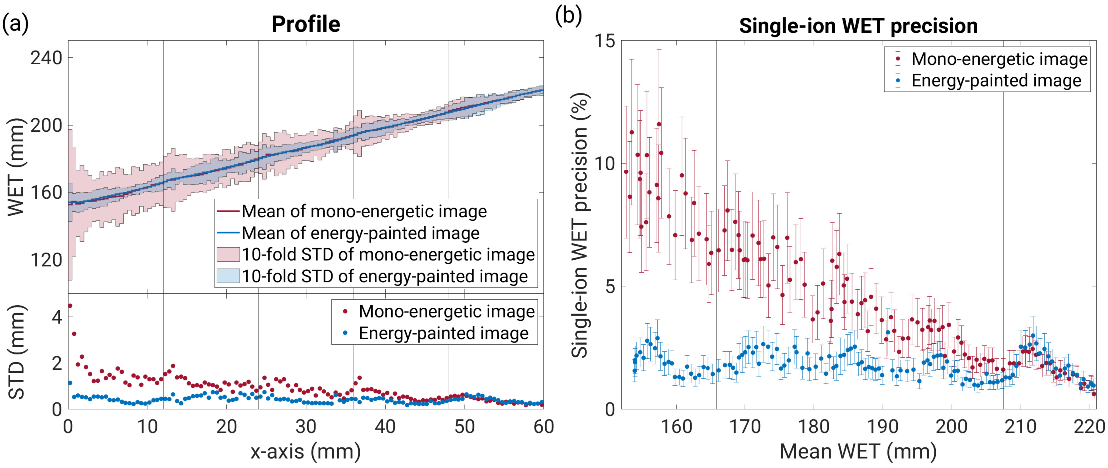

Figure 4.5: Validation of energy painting algorithm by means of wedge phantom. (a) Profiles through radiographs of a wedge phantom are shown (red: mono-energetic, blue: energy painted). The mean WET per pixel column of the radiograph is denoted by the steps, the 10-fold standard deviation by the envelope. In the lower panel the standard deviation is shown as points. (b) The SIWP, which is related to the standard deviation (see section 3.8.1), is plotted against WET. Reprinted from Metzner et al. (2024b). © Institute of Physics and Engineering in Medicine. Reproduced with permission. All rights reserved.

section 3.5). For the mono-energetic radiograph, the calibrated initial beam energy of 206.35 MeV/u was employed since for the other, lower energies, ions would stop within the phantom causing empty pixels especially for the high WET regions. The energy-painted radiograph was acquired with four of the calibrated initial beam energies between 178.13 MeV/u and 206.35 MeV/u.

The gradient of the wedge was positioned parallel to the horizontal axis of the detectors' pixel matrix (rows). Along this axis, the resulting radiograph should therefore exhibit the constant WET gradient while the columns of the resulting radiographs should be constant in WET. By calculating the mean within these columns, a profile can be obtained for both the mono-energetic and the energy-painted radiograph, which is shown in the upper panel of fig. 4.5(a). The standard deviation of the pixel columns is shown in the background as envelope, multiplied by a factor of ten for better visibility. The lower subfigure visualizes the onefold standard deviation as a function of WET.

In both the upper and lower panel of fig. 4.5(a), it can be seen that the standard deviation of the mono-energetic and energy-painted images is similar for high WETs ($x > 50$ mm). This is due to the fact that the energy-painted image in this region was also acquired with the highest energy. Therefore, both radiographs are based on mostly the same data for this WET interval. For decreasing WETs ($x < 50\,\mathrm{mm}$), the standard deviation deteriorates in the mono-energetic radiograph whereas the energy-painted image preserves its precision. The small oscillations in the standard deviation of the energy-painted image are due to the discrete choices of initial beam energy: every time the energy is switched for changing WETs, the precision values sharply decrease which is then followed by a slow increase until the next switch of energy.

For further quantitative evaluation of the method, in fig. 4.5(b) the SIWP is shown as a function of mean WET. The trend of this curve closely resembles the trends seen in the standard deviation in fig. 4.5(a). This is due to the fact that the data points in fig. 4.5(b) were calculated based on the ones in fig. 4.5(a). The mean WET shown on the x-axis in fig. 4.5(b) depends approximately linearly on the x-axis in fig. 4.5(a) as demonstrated by the profile. Furthermore, the SIWP is calculated from the standard deviation (see eq. (3.8.2)).

The behavior of the SIWP over WET confirms the trends, which could be observed for the precision of the calibration curves in fig. 4.4(c-d): If several energies are applied, the precision follows an oscillating pattern as a function of WET, similar to a sawtooth. The maximum SIWP determined based on the two different radiographs is

$$\begin{aligned} \max(\mathrm{SIWP}_{\text{energy painted}}) &= (3.1 \pm 1.0)\,\% \\ \max(\mathrm{SIWP}_{\text{mono-energetic}}) &= (12 \ \pm 4)\,\% \,. \end{aligned}$$

Consequently, energy painting reduces the maximum SIWP in the investigated WET interval by (73 ±11) %. This corresponds to an improvement by a factor of (3.9 ± 1.5). The mean SIWP of the radiographs acquired with one and multiple initial beam energies is

$$\begin{aligned} \mathrm{mean}(\mathrm{SIWP}_{\text{energy painted}}) &= (1.82 \pm 0.05)\,\% \\ \mathrm{mean}(\mathrm{SIWP}_{\text{mono-energetic}}) &= (4.67 \pm 0.25)\,\% \,. \end{aligned}$$

Due to the use of the energy-painting method, we can thus report a reduction of the mean SIWP by (61.0 ±2.3) % and hence an improvement by a factor of 2.49 ± 0.16.

In fig. 4.6(a), the energy-painted radiograph is shown. The constant WET gradient can be distinctly seen in the image with a low noise level[2] of (0.423 ± 0.014) mm. In fig. 4.6(b), the mean WET of the radiograph per pixel column is plotted along the axis of incline of the wedge. A linear fit is performed through these data points. In the lower panel of fig. 4.6(b), the residuals of the points with respect to the fit are shown

---

[2] The standard deviation within each pixel column in fig. 4.6(a) was calculated as a measure for noise. Then, the mean noise level was determined over all columns.

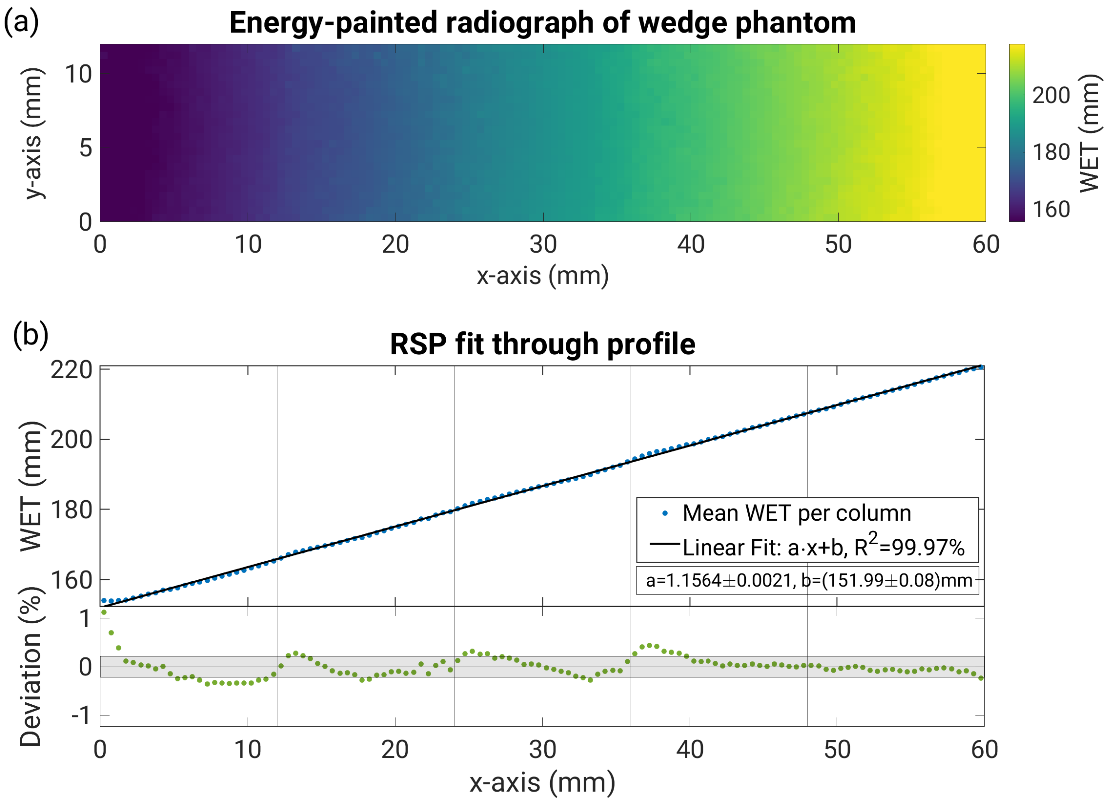

Figure 4.6: Energy-painted radiograph and RSP accuracy. (a) Energy-painted radiograph of the wedge phantom showing the WET interval between 150 mm and 220 mm. (b) RSP fit through the profile of the radiograph. The residuals of the fit are shown in the lower panel. The slope of the linear fit yields the RSP of the material the wedge is made from. The gray lines in the back mark the transitions due to the limited detector size, where the data was stitched together from separate acquisitions (see section 3.5). Reprinted from Metzner et al. (2024b). © Institute of Physics and Engineering in Medicine. Reproduced with permission. All rights reserved.

together with the 1σ band corresponding to 0.22 %. The vertical gray vertical lines in the background denote the transitions due to the limited FOV of the detector. Here, the data is combined from two neighboring acquisitions.

Since the geometric slope of the wedge phantom is 1, the slope of the fit should directly yield the RSP of the material. The determined value RSP_{fit} and the reference value RSP_{RP} obtained by means of range-pullback measurements are

$$\begin{aligned} \text{RSP}_{\text{fit}} &= 1.1564 \pm 0.0021 \\ \text{RSP}_{\text{RP}} &= 1.1611 \pm 0.0028\,. \end{aligned}$$

Thus, the RSP obtained from the fit through the profile of the energy-painted radiograph deviates from the reference value by only 0.4 % indicating accurately determined WET values.

4.3 Imaging of anthropomorphic phantom and comparison to clinical X-ray CT modalities

This section is based on Metzner et al. (2025a).

Up to now, the limited high-precision WET range of the detection system based on thin detectors inhibited the imaging of anthropomorphic phantoms. After successfully establishing and validating the energy painting method, imaging of clinically more realistic phantoms is the next natural step in order to develop the detection system further toward clinical use. This section presents an energy-painted helium-beam radiograph of an anthropomorphic phantom and a comparison to clinically used X-ray CT modalities.

In fig. 4.7(a), the WET-maps obtained from different imaging modalities are shown. In the first column, the reference image is displayed. It was derived from a data set previously presented in Wohlfahrt et al. (2018). This reference data set was established by means of range-pullback measurements of the materials occurring in the phantom and a high-resolution segmentation of an X-ray CT scan (see section 3.9.1). Throughout the following analysis, this data set will be treated as the ground truth image, which all metrics for similarities and deviations between two images in this section will refer to. This assumption will later be discussed in detail in the discussion in section 5.3.
In the second column, the αRad is shown. It was acquired with five beam energies between 146.84 MeV/u and 188.07 MeV/u and assembled from twelve sub-regions of 12 mm × 12 mm each (see section 3.9.3).
In the last two columns, the images based on X-ray CT imaging modalities are presented. A dual-energy computed tomography (DECT-DirectSPR) and single-energy computed tomography (SECT-HLUT) scan, which were converted to RSP values beforehand, were projected to obtain WET-maps (see section 3.9.2).
The four images show the same region of the anthropomorphic head phantom: the nasopharyngeal cavity at the skull base. All images exhibit the same anatomical structures and qualitatively demonstrate a visual similarity.

To compare the images quantitatively, in fig. 4.7(b-d), the helium-beam radiograph and the projections of the converted X-ray CT scans are compared with respect to the reference image by means of different metrics.

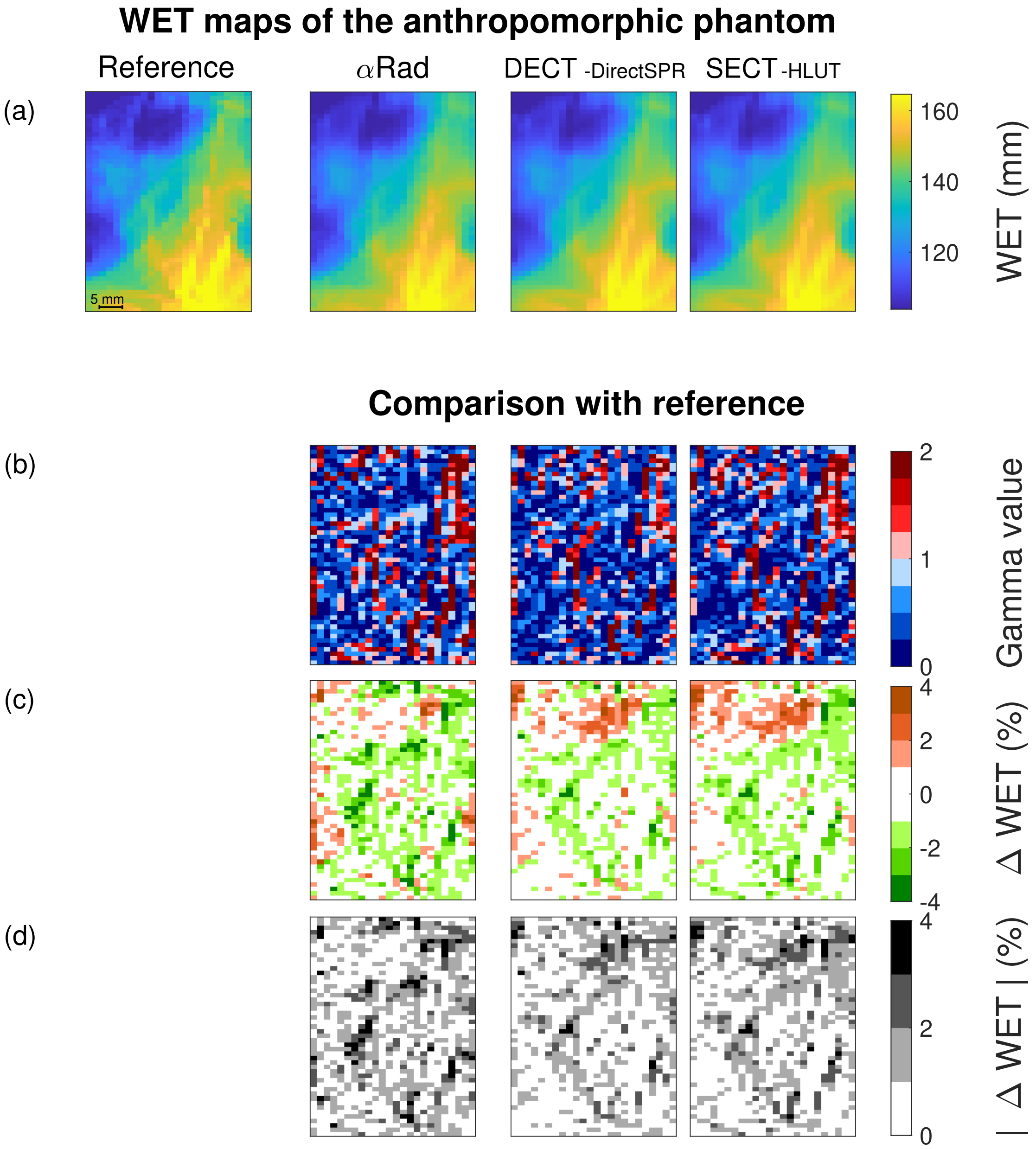

Figure 4.7: WET-maps of skull base region of the anthropomorphic phantom acquired with different imaging modalities and their quantitative comparison. (a) WET-maps determined with different imaging modalities: reference based on range-pullback measurements and a high-resolution segmentation, helium-beam radiograph (αRad), projections of a dual-energy computed tomography (DECT-DirectSPR), and single-energy computed tomography (SECT-HLUT) scan, which were converted to RSP values beforehand. (b) Gamma analysis between imaging modalities and reference with the criteria 1 mm and 0.7 %. (c) Percentage difference between imaging modalities and reference. (d) Absolute values of percentage differences. Reprinted from Metzner et al. (2025a), CC BY 4.0.

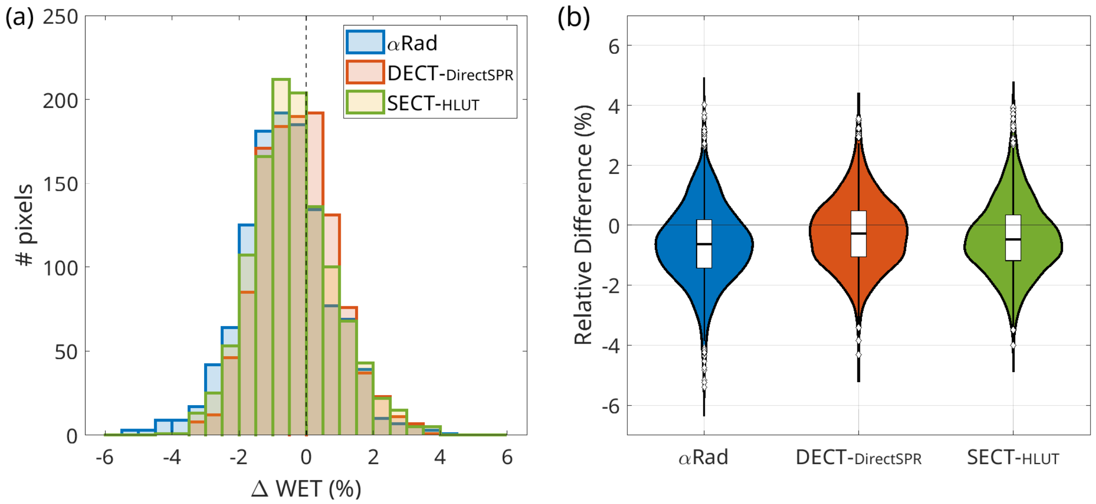

Figure 4.8: Relative differences of helium-beam radiograph (αRad) and projected RSP data sets based on dual-energy computed tomography (DECT-DirectSPR) or single-energy computed tomography (SECT-HLUT) with respect to reference image. (a) Histograms of relative differences, (b) Violin plots, where the white boxes denote the first and third quartiles and the black line the median. Reprinted from Metzner et al. (2025a), CC BY 4.0.

In row (b), a gamma analysis[3] with the criteria 0.7 % and 1 mm is displayed. The criteria were chosen based on the uncertainties which were stated by Wohlfahrt et al. (2018) for the reference scan. The passing rates are

$$\begin{aligned} \gamma_{\alpha\mathrm{Rad}} &= (73.9 \pm 0.9)\,\%, \\ \gamma_{\mathrm{DECT}} &= (78.7 \pm 0.7)\,\% \\ \gamma_{\mathrm{SECT}} &= (74.1 \pm 0.8)\,\%\,. \end{aligned}$$

In fig. 4.7(c), the percentage differences between the three imaging modalities and the reference are shown. Figure 4.7(d) presents the absolute value of these same percentage differences. Histograms and violin plots[4] of these percentage differences can be seen in fig. 4.8(a-b). The standard deviations in fig. 4.8(a) amount to 1.33 % for the helium-beam radiograph, 1.16 % for the DECT-DirectSPR and 1.24 % for the SECT-HLUT.

Two different metrics were chosen to compare the distributions (see section 3.9.5): the mean absolute percentage error (MAPE) and root-mean-square percentage error (RMSPE). The MAPE determined for the three modalities with respect to the reference

---

[3] Calculated with the code of Geurts (2024).

[4] Visualized with the code of (Karvelis and oyvindlr 2024).

is

$$\begin{aligned}
\mathrm{MAPE}_{\alpha\mathrm{Rad}} &= (1.16 \pm 0.05)\,\% \\
\mathrm{MAPE}_{\mathrm{DECT}} &= (0.95 \pm 0.05)\,\% \\
\mathrm{MAPE}_{\mathrm{SECT}} &= (1.05 \pm 0.06)\,\%\,.
\end{aligned}$$

The RMSPE is

$$\begin{aligned}
\mathrm{RMSPE}_{\alpha\mathrm{Rad}} &= (1.46 \pm 0.06)\,\% \\
\mathrm{RMSPE}_{\mathrm{DECT}} &= (1.19 \pm 0.05)\,\% \\
\mathrm{RMSPE}_{\mathrm{SECT}} &= (1.30 \pm 0.06)\,\%\,.
\end{aligned}$$

In fig. 4.9, profiles through the WET-maps in fig. 4.7(a) are presented. In (a), the WET-map of the reference is repeated with a black rectangle marking the pixel columns, which were used for the calculation of the profile. In (b), the mean WET of the selected pixels per row is plotted against the y-axis of the selected region. In the lower panel, the residuals and their uncertainties are plotted.
The deviations seem to oscillate around zero. Especially for $y > 35\,\mathrm{mm}$, the uncertainties and deviations are pronounced, which is in agreement with the high difference values in the upper part of the image in fig. 4.7(c-d). Interestingly, the deviations of all modalities behave similar, the potential reasons for which will be discussed in section 5.3.

To gain a better understanding of the source of these WET deviations, the RSP deviations can be investigated per tissue type along the projection direction. For the respective analysis, the full 3D data sets, so the reference, the DECT-DirectSPR and SECT-HLUT are taken into account. Since the helium-beam radiograph does not provide 3D RSP information, the materials in this data set cannot be distinguished from each other, which is why it was left out for this very specific analysis. For the following analysis, for one exemplary pixel, we consider the column of voxels along the projection direction in the 3D images.

In fig. 4.10(a), the reference WET-map is shown and an exemplary pixel at around $x = 30\,\mathrm{mm}$, $y = 17\,\mathrm{mm}$, which the following analysis will focus on, is marked in red. The dimension along which we projected the data sets is referred to as z in the following since it also corresponds to the direction of the beam axis. The set of voxels over which the RSP was integrated along the beam direction (z-axis) to obtain a specific pixel's WET is referred to as pixel channel in the following.

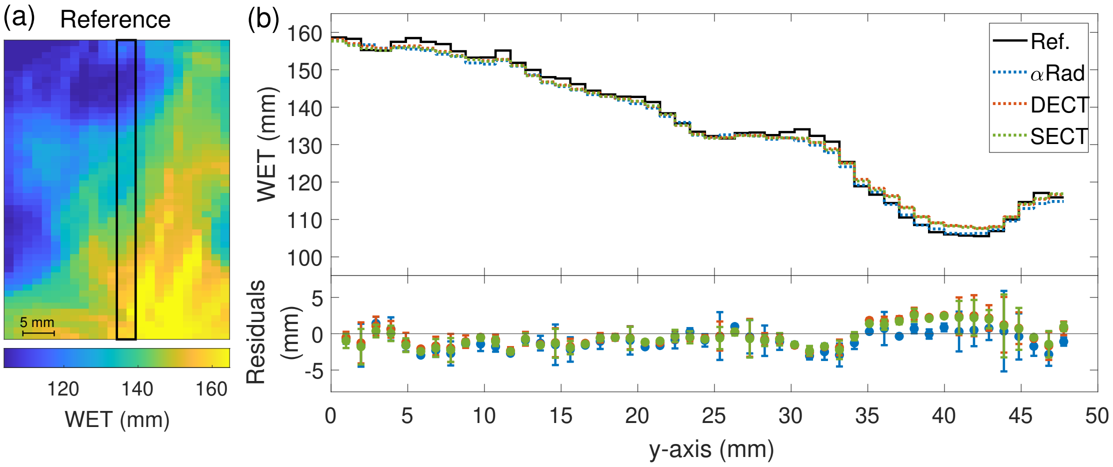

Figure 4.9: Profile through the WET-maps in fig. 4.7(a). In (a), the pixel columns which were used to calculate the profiles are marked in the reference image. In the upper panel of (b), the profiles are plotted for the WET-maps based on the reference, helium-beam radiograph (αRad), dual-energy computed tomography (DECT-DirectSPR) and single-energy computed tomography (SECT-HLUT). In the lower panel of (b), the residuals with respect to the reference are shown.

In fig. 4.10(b), the RSP of the 3D imaging modalities is plotted along the z direction. The integral over these RSP values corresponds to the WET of the pixel marked in fig. 4.10(a), which amounts to around (161.16 ±1.13) mm.
In this graph, it can be seen which tissue types contributed to the WET in the pixel at $x = 30$ mm, $y = 17$ mm. The discrete reference RSP values of the six materials present in the investigated region are marked with the black horizontal solid lines. The reference data set is composed of only these six values. The fact that intermediate values can also be seen in the profile of the reference is caused by the registration and therefore interpolation of the reference data set to the bigger pixel grid of the CT data sets (see section 3.9.4).

Moreover, in general it can be observed that the DECT-DirectSPR and SECT-HLUT blur the RSP of the different materials over depth. This is expected, since they have a finite spatial resolution. In contrast to that, the reference scan is only limited by its voxel size. Due to the blurring of the CT scans, high RSP values are underestimated, while low RSPs are overestimated.

Because the deviations in fig. 4.7(c,d) look similar to anatomical structures, the correlation between high deviations in WET and the proportion of a material in a pixel channel is investigated in the following. To investigate correlations, the abundance of materials

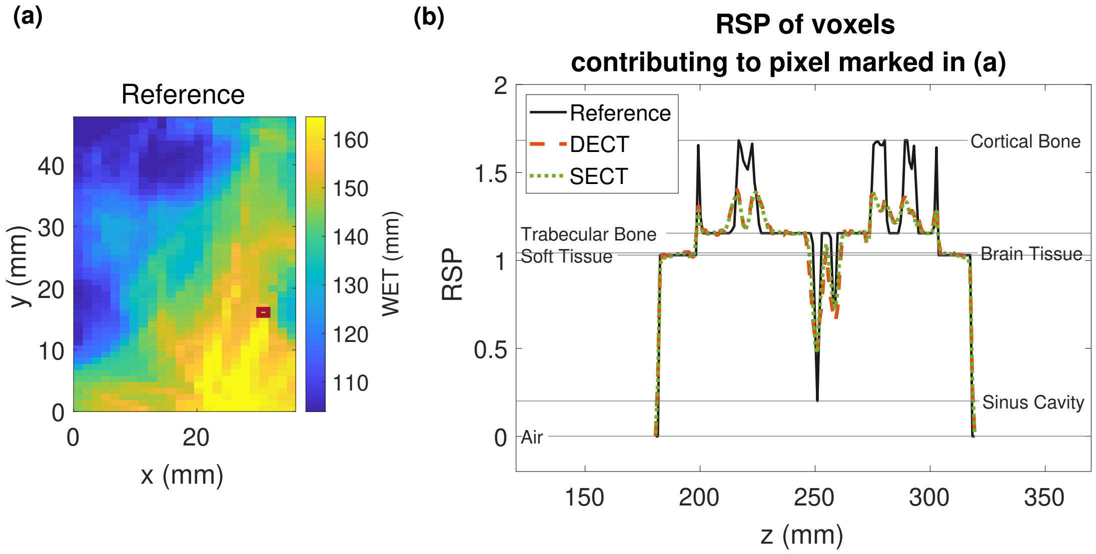

Figure 4.10: RSP deviations shown for one exemplary pixel. In (a), the investigated pixel is marked in the WET-map of the reference scan. (b) The RSP values which contributed to the pixel in (a) are shown for the 3D imaging modalities: reference, dual-energy computed tomography (DECT-DirectSPR) and SECT-HLUT. The RSP values are plotted against the beam-aligned coordinate z of the 3D volume. The discrete reference RSP values for the six tissue types which are present in the imaged region are marked with the black horizontal solid lines.

along the z-axis was determined by means of the reference scan.
The gray scale in the images in fig. 4.11(a) denotes how many voxels in a specific pixel channel contained a certain tissue-equivalent material. The x- and y-axes show the same region as in fig. 4.7. For this analysis, the voxels around the phantom were discarded. Thus, the percentage of air is rather low if only phantom voxels are considered.

In fig. 4.11(b), the correlation between the six images in fig. 4.11(a) and the WET-difference-maps in fig. 4.7(c) is plotted against all tissue types of the phantom. High correlations indicate that a high number of voxels of a certain material often occur in the same pixels where high deviations in WET are present.
Such a correlation might be easiest to perceive by eye if the abundance of sinus cavity tissue in fig. 4.11(a) and the plot showing the relative differences for the DECT-DirectSPR and SECT-HLUT scan (fig. 4.7(c)) are compared. In both images, a cluster of high intensity values can be seen in the upper half of the images.

The analysis in fig. 4.11(b) indicates that a high abundance of air and sinus cavity correlates with positive percentage deviations of all three imaging modalities. The

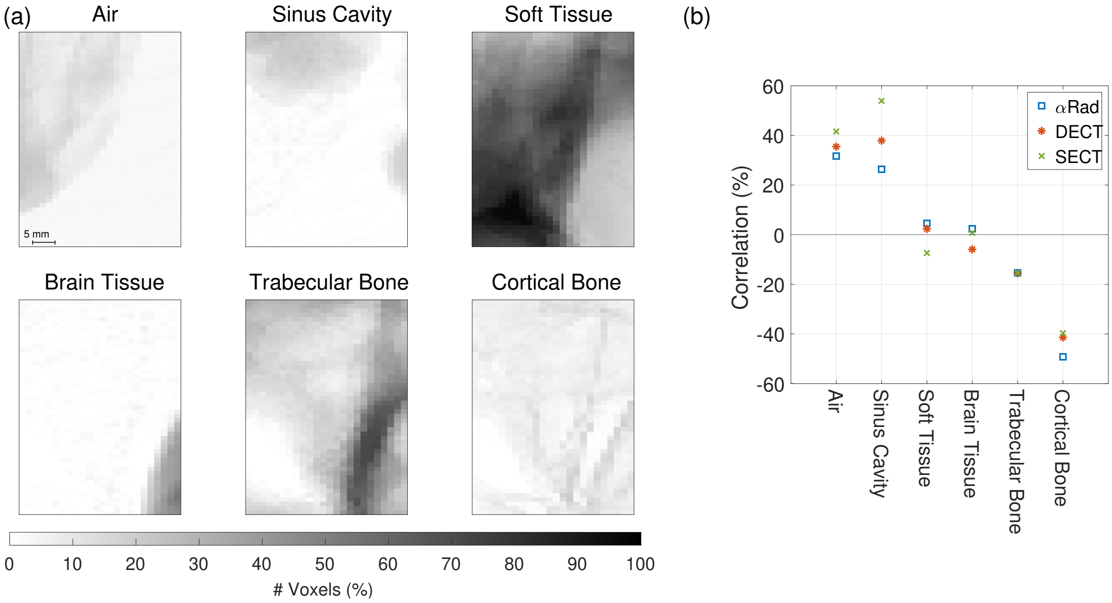

Figure 4.11: (a) Abundance of different tissue-equivalent materials in a channel of the anthropomorphic phantom contributing to the WET of each pixel, (b) Correlation between abundance of a material and deviation in WET for all three imaging modalities. Reprinted from Metzner et al. (2025a), CC BY 4.0.

highest correlation of 54 % can be found between sinus cavity and the WET-deviations of SECT-HLUT. Inversely, channels containing a lot of cortical bone seem to be correlated with negative deviations in all the three images. The highest anticorrelation was determined to occur between the deviations of αRad and cortical bone amounting to 49 %. The abundance of soft and brain tissue does not exhibit a strong correlation with WET deviations of all three modalities.

Despite the deviations from the reference scan, the WET accuracy reached with the helium-beam radiography system was shown to be competitive with modalities routinely used in clinics. Furthermore, an important milestone was reached by imaging an anthropomorphic phantom with a detection system based on thin detectors.

4.4 2.5D Imaging

In the future, ion-beam radiography could be applied in clinical conditions to monitor the anatomy of the patient between the fractions of ion-beam radiotherapy treatments. If ion-beam radiographs are acquired along the treatment beam direction before each fraction, anatomical changes can be detected in the resulting difference images. By means of these radiographs, the changes can be localized laterally and quantified in terms of WET, which is important information in order to evaluate their impact on the treatment dose distribution. However, due to the integration along the beam direction, the change cannot be localized along depth. Thus, it cannot be traced whether a change happened within the treatment field or at greater depth where it does not influence the treatment.

This is the reason why it is highly desirable to also obtain a rough estimate for the depth of an anatomical change in an ion-beam radiograph. This is exactly the purpose of the 2.5D imaging approach, which utilizes the maximum spatial resolution over the reconstruction depth of ion-beam radiographs to assess the actual depth of a feature (Volz et al. 2024, Metzner et al. 2025b). The corresponding methodology is explained in section 3.10.

The 2.5D methodology was recently introduced in a publication with the focus on spatial-resolution improvements of ion radiography. In the simulation study of Volz et al. (2024), the depth detection was investigated for a proton-beam radiographs acquired with perfect detectors right at the phantom's surface. In this thesis, it is tested in simulations of our realistic setup together with a proton and helium-ion beam. In that way, the simulations and analysis can be used to compare the performance of the two ion types for the 2.5D imaging method. After these simulation-based studies, the 2.5D imaging technique is assessed experimentally with the same setup as in the simulations. The methodology is advanced to enable an application to clinically more realistic phantoms. As a last result, the potential of the 2.5D imaging approach is tested for an anthropomorphic phantom.

4.4.1 Monte Carlo simulations with a proton beam

To assess the 2.5D imaging method in a well-controlled setup, a simple phantom was used for the simulations which can also be realized in experiments. In the simulations, our detection system and the homogeneous PMMA phantom, which is described in detail in section 3.10, were emulated. To mimic an anatomical change, an air gap was inserted into the otherwise homogeneous phantom. Laterally, it was positioned such that the edge of the air gap was located in the middle of the FOV.

At first, a proton beam impinging on the detection system and the PMMA phantom was simulated to keep the ion type constant compared to Volz et al. (2024). In that way, the impact of the realistic detector setup and phantom can be assessed first and the investigation presented here can be connected with the one in Volz et al. (2024). Around 4.4×10^5 protons which crossed all six detectors were taken into account for the data analysis. The initial beam energy was set to 188.07 MeV/u.

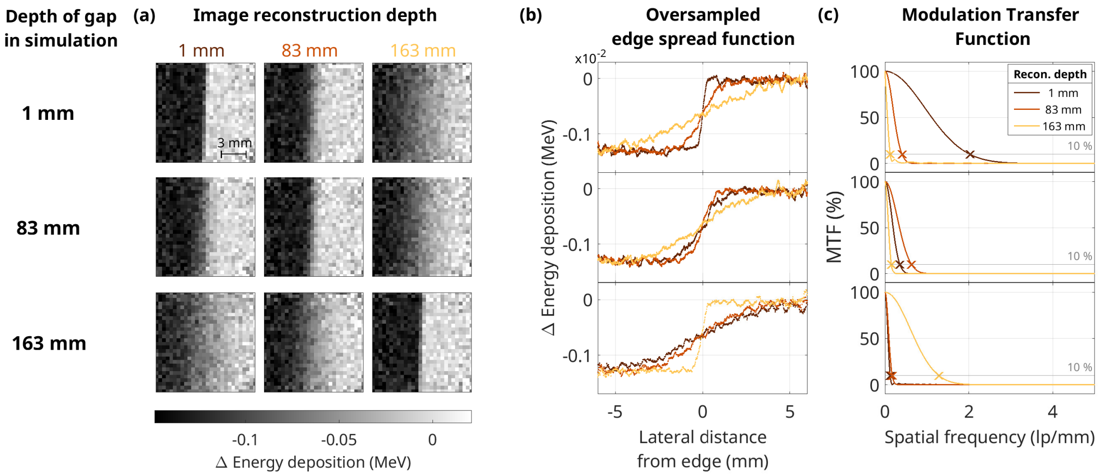

Figure 4.12: Demonstration of the 2.5D imaging method based on simulated proton-beam radiographs. An air gap was positioned at different depths of a homogeneous phantom (rows). (a) Difference images between the full phantom and the ones containing the air gap were reconstructed at different depths (columns). (b) The oversampled edge spread function (OSESF) and (c) the modulation transfer function (MTF) for the images in (a) are shown.

Proton-beam radiographs of the phantom containing the 1.9 mm thin air gap were simulated. The air gap was successively positioned at five different depths within the PMMA phantom: 1 mm, 40 mm, 83 mm, 123 mm and 163 mm, referring to the center of the air gap. Additionally, one radiograph of the completely homogeneous phantom was simulated to also obtain a reference image without the artificial anatomical change. If the images with the air insert are subtracted from the reference, an image of only the change, so the air gap, is obtained. This image is referred to as difference image in the following.

The resulting simulated proton-beam radiographs can be seen in fig. 4.12(a) for three of the simulated gap positions. Here, the difference plane-of-interest binned (PIB) images with respect to the full phantom are shown, where each row represents a separate simulation with a different air gap position. In the three columns, the difference images are shown at different reconstruction depths. Note that these images do not correspond to the slices of a CT, but still are projections. They only differ in the spatial distribution of the single-ion data which was binned into pixels depending on the lateral position of the ions at this certain depth according to their path estimate.
These difference radiographs are quantitative in terms of energy deposition since no calibration curves were established for the simulated setup. However, the calibrations are not required for the 2.5D imaging method.

In the difference images, two rather homogeneous regions can be seen. The region in the right half of the image has values around zero since no change in this region occurred. In the left half of the image, a change in form of an energy-deposition reduction can be detected, which is caused by the insertion of the air gap into that half of the phantom. The transition between the two rather homogeneous WET regions is oriented at an angle of 2° with respect to the vertical detector axis. This facilitates the determination of the spatial resolution through the slanted edge approach (Reichenbach et al. 1991, Fujita et al. 1992) (see section 3.10).

In fig. 4.12(b), the oversampled edge spread function (OSESF) of the images shown in fig. 4.12(a) is depicted. Figure 4.12(c) shows the corresponding modulation transfer functions (MTFs). If the MTF at 10 % contrast is evaluated, a measure for the spatial resolution can be obtained. This quantity can also be used to compare different imaging systems with each other.

In fig. 4.12(a), it can be seen by eye, that the images vary in sharpness and the images on the diagonal seem to resolve the edge best. This is also confirmed by the OSESFs and MTFs in (b-c) of the same figure. The hypothesis that the spatial resolution reaches a maximum where the reconstruction depth is similar to the actual depth of the feature seems to agree with the observations which can be made by means of this graph.

To investigate the evolution of spatial resolution over depth with finer sampling, in fig. 4.13, the spatial resolution is plotted against depth for 1 mm-spaced reconstruction depths. The actual simulated gap position is marked with a vertical bar each in the background. The spatial-resolution curve which was smoothed over depth by means of a Savitzky-Golay filter (line) (Savitzky and Golay 1964) and the corresponding 2σ uncertainty (envelope) are used to determine the depth of the maximum spatial resolution (triangle).
In this graph, it can be seen that each curve for the spatial resolution over depth exhibits a maximum. For all simulated gap positions, this maximum is reached at a reconstruction depth less than 5 mm away from the actual position. The maximum spatial resolution together with its corresponding reconstruction depth is listed in table 4.2 for all five simulated gap positions.

4.4.2 Monte Carlo simulations with a helium beam

Our research group primarily focuses on ion-beam radiographs acquired with helium beams due to their superior spatial resolution compared to proton-beam radiographs at the same dose (Gehrke et al. 2018a). This is also the reason why the 2.5D imaging

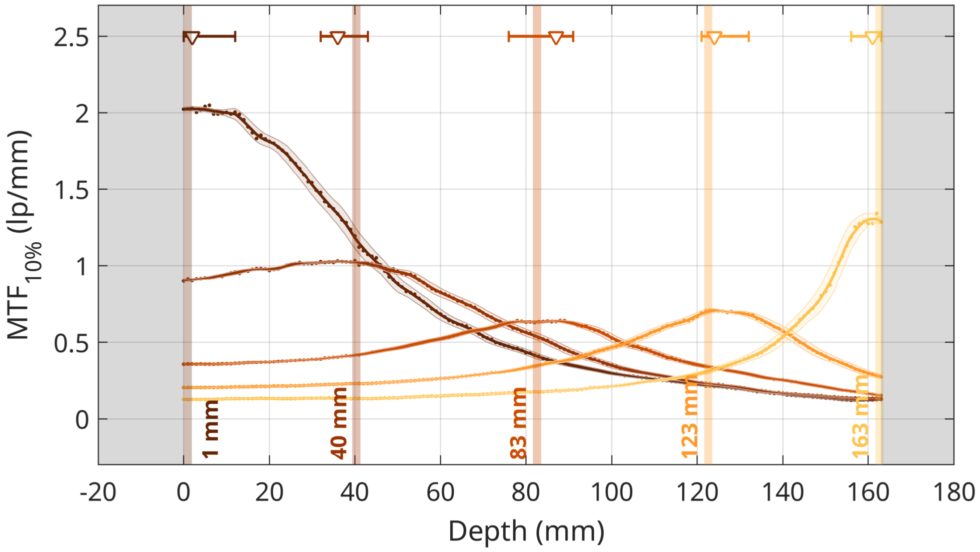

Figure 4.13: Spatial resolution against depth determined with the slanted edge method (Reichenbach et al. 1991, Fujita et al. 1992) for the simulated proton-beam radiographs. For all five positions of the air gap (denoted by vertical bars of different colors in the background) the spatial resolution for each reconstruction depth (dots) was determined. The lines represent the spatial resolution (SR) over depth after smoothing and the envelope the corresponding 2σ uncertainty. Triangles mark the depth of the maximum SR based on the smoothed lines.

method, which is considered an extension of the daily imaging with helium ions, should ideally also work with this type of ion.

Therefore, the simulations and analyses were repeated for a helium beam with the same energy per nucleon. Also, the detection system and phantom were exactly the same. The number of particles was reduced by a factor of four in comparison to the proton simulations in order to keep the dose approximately constant, resulting in around 1.1×10^5 particles crossing all detectors.

Analogously to fig. 4.12(a), in fig. 4.14(a) the difference PIB images extracting the air gap are shown. Furthermore, the OSESF and MTF are depicted to facilitate a comparison with the proton-beam radiographs. Figure 4.15 shows the spatial resolution against depth, where the vertical bars and the triangles show the actual and the estimated air gap positions, the latter being based on the maximum spatial resolution. The triangles mark the depth of the maximum spatial resolution.

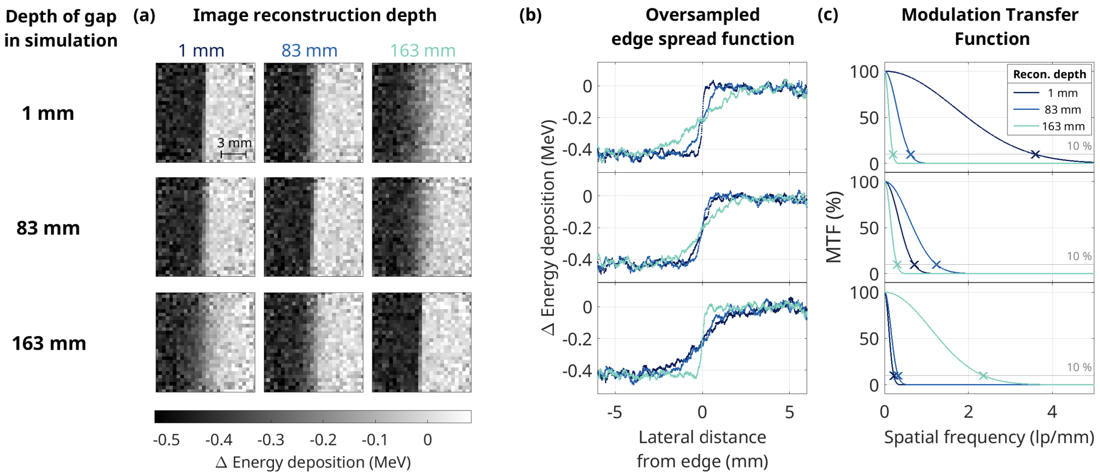

Figure 4.14: Demonstration of the 2.5D imaging method based on simulated helium-beam radiographs. An air gap was positioned at different depths of a homogeneous phantom (rows). (a) Difference images between the full phantom and the ones containing the air gap were reconstructed at different depths (columns). (b) The oversampled edge spread function (OSESF) and (c) the modulation transfer function (MTF) for the images in (a) are shown.

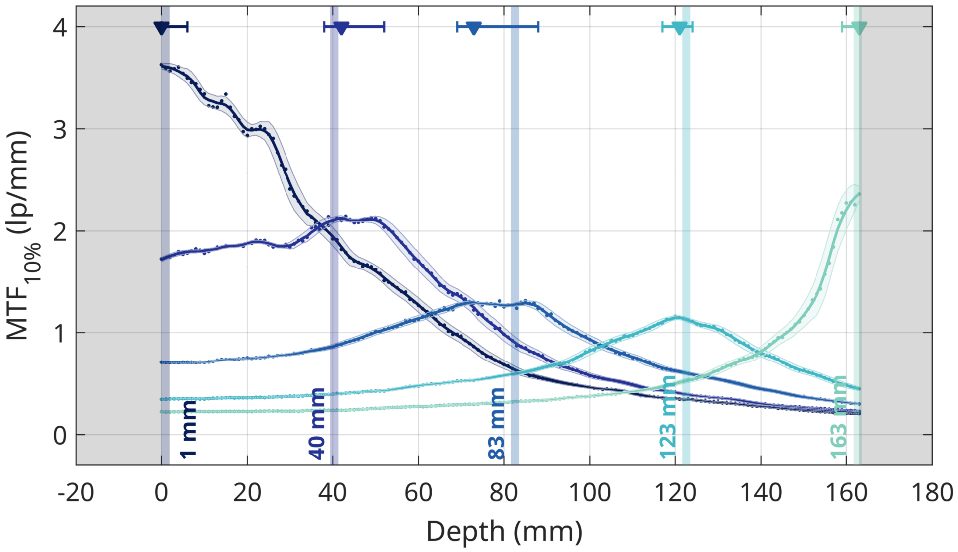

Figure 4.15: Spatial resolution against depth determined with the slanted edge method (Reichenbach et al. 1991, Fujita et al. 1992) for the simulated helium-beam radiographs. For all five positions of the air gap (denoted by vertical bars of different colors in the background) the spatial resolution for each reconstruction depth (dots) was determined. The lines represent the spatial resolution (SR) over depth after smoothing and the envelope the corresponding 2σ uncertainty. Triangles mark the depth of the maximum SR based on the smoothed lines.

Table 4.2: Maximum spatial resolution of air gap in simulated proton- and helium-beam radiographs. The air gap was positioned at five different depths. For each of the corresponding data sets, the maximum spatial resolution (SR) and the corresponding reconstruction depth (RD) were determined.

Depth of gap in simulation	Protons		Helium ions	
	Maximum SR	Corresponding RD	Maximum SR	Corresponding RD
(mm)	(lp/mm)	(mm)	(lp/mm)	(mm)
$0.0 - 1.9$	2.025 ± 0.014	2^{+10}_{-2}	3.612 ± 0.025	0^{+6}_{-0}
$39.4 - 42.3$	1.028 ± 0.005	36^{+7}_{-4}	2.122 ± 0.025	42^{+10}_{-4}
$81.7 - 83.6$	0.639 ± 0.006	87^{+4}_{-11}	1.297 ± 0.014	73^{+15}_{-4}
$121.7 - 123.6$	0.707 ± 0.011	124^{+8}_{-3}	1.146 ± 0.019	121^{+3}_{-4}
$161.7 - 163.6$	1.31 ± 0.04	161^{+2}_{-5}	2.36 ± 0.08	163^{+0}_{-4}

In table 4.2, the maximum spatial resolution for the helium-beam radiographs is listed for all five gap positions. Furthermore, the corresponding reconstruction depth is given there. For the helium-beam radiographs, the maxima of the spatial resolution occur at reconstruction depths within 10 mm of the actual depth of the air gap in the simulation. The depth estimates agree with the ground truth positions within the uncertainties for all gap positions.

4.4.3 Comparison of Monte Carlo simulations with proton and helium beam

Evaluating fig. 4.14, fig. 4.15 and table 4.2, it becomes apparent that the helium-beam radiographs overall exhibit a higher spatial resolution. While the maximum spatial resolution achieved with the proton beam is (2.025 ± 0.014) lp/mm, (3.612 ± 0.025) lp/mm were reached with the helium ions. Also, for the gap with the overall lowest spatial resolution the helium beam outperforms the proton beam: the helium-beam radiographs exhibit a spatial resolution of (1.146 ± 0.019) lp/mm for the gap at 123 mm while the one acquired with the proton-beam reaches (0.639 ± 0.006) lp/mm for the gap at 83 mm.

In fig. 4.16, the accuracy of the 2.5D imaging method based on both simulated ion types is compared for the five different air gap positions. The accuracy is defined as the difference between the 2.5D depth estimate and the actual depth of the gap in

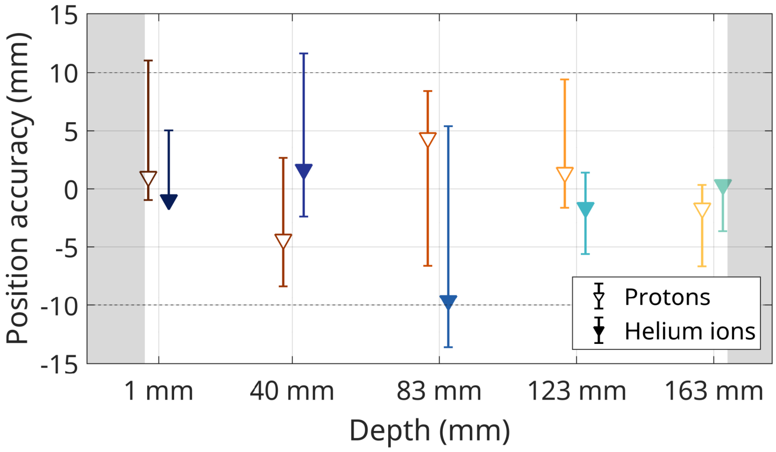

Figure 4.16: Accuracy of the 2.5D imaging method based on simulated proton- and helium-beam radiographs. The difference between the 2.5D depth estimate and the actual depth of the air gap within the phantom is presented for both the proton- and helium-beam radiographs for all five simulated gap positions. The uncertainty bands represent the precision and are based on the 2σ envelopes shown in figs. 4.13 and 4.15.

the simulation. In this graph, the accuracy values for both proton and helium-beam radiographs are shown for all five gap positions. Furthermore, the envisaged accuracy limit of 1 cm is marked with the dashed lines at ± 10 mm.

Most importantly, from this graph we can conclude that the 2.5D imaging approach also works for a realistic detector, emulating the one used for our experiments, and a realistic phantom. All accuracy values are below 10 mm. Furthermore, all depth estimates agree with the ground truth depth within the uncertainties.

Moreover, both proton and helium ions perform equally well in terms of accuracy and precision (defined as the uncertainty bands in fig. 4.16). Since helium ions deliver overall better image quality than protons, the experimental studies in the following section were conducted with helium only.

4.4.4 2.5D imaging experiments with a helium beam

This section is based on Metzner et al. (2025b).

To advance the 2.5D imaging approach towards applicability for anthropomorphic phantoms, it was tested experimentally with a helium beam in three steps:

- **Experimental verification of simulations:** At first, experiments with the same phantom as in the simulations were conducted. Employing the same phantom renders a comparison of the experiments and the simulations feasible. Furthermore, we can characterize the 2.5D imaging method quantitatively in this well-controlled setup.
- **Advancement of the methodology towards object-agnosticism:** To advance the methodology towards clinically more realistic phantoms, another methodology, which does not rely on a slanted edge within the image, is required. Therefore, the so-called Tenengrad metric is tested and benchmarked against the slanted edge technique for the data set acquired with the air gap phantom.
- **Application to anthropomorphic phantom:** In a last step, the 2.5D imaging method based on the Tenengrad metric was applied to an anthropomorphic phantom with a silicone insert in the nasopharyngeal cavity. By extracting the depth of the silicone insert within the phantom, we get an estimate for the depth accuracy of the 2.5D imaging approach in a clinically realistic setting in terms of phantom (i.e. anatomical complexity) and imaging dose.

Experimental verification of simulations

In fig. 4.17, the results of the experimentally acquired helium-beam radiographs are displayed in the same layout as in figs. 4.12 and 4.14. In the rows, the data of the different physical air gap positions is shown, whereas the columns in (a) represent different reconstruction depths of the difference images. In contrast to the simulations, these images are quantitative in terms of WET since calibration curves were established in experiments. In all nine images, the difference due to the air gap can be clearly distinguished from noise. The difference in WET due to the air gap amounts to (-2.057 ± 0.012) mm on average within the images. Compared to the WET determined by means of range-pullback measurements, the WET of the gap was determined with an accuracy value of (0.39 ± 0.20) %.

In fig. 4.17(b), the oversampled edge spread function (OSESF) is shown for the three reconstruction depths and fig. 4.17(c) shows the resulting MTF. The MTF evaluated at 10 % contrast is used as the measure for spatial resolution in the following analysis.

Analogously to fig. 4.13 and fig. 4.15, in fig. 4.18 the spatial resolution is plotted against depth for the experimentally acquired data. In this graph it is apparent that the 2.5D depth estimate agrees with the actual depth within the uncertainties. Only for the gap

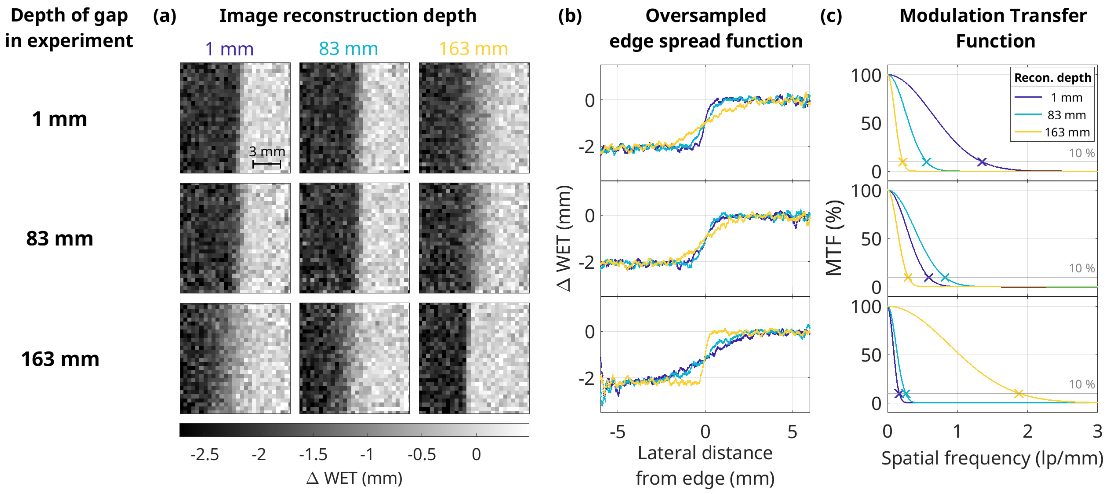

Figure 4.17: Demonstration of the 2.5D imaging method based on experimentally acquired helium-beam radiographs. An air gap was positioned at different depths of a homogeneous phantom (rows). (a) Difference images between the full phantom and the ones containing the air gap were reconstructed at different depths (columns). (b) The oversampled edge spread function (OSESF) and (c) the modulation transfer function (MTF) for the images in (a) are shown. Reprinted from Metzner et al. (2025b), CC BY 4.0.

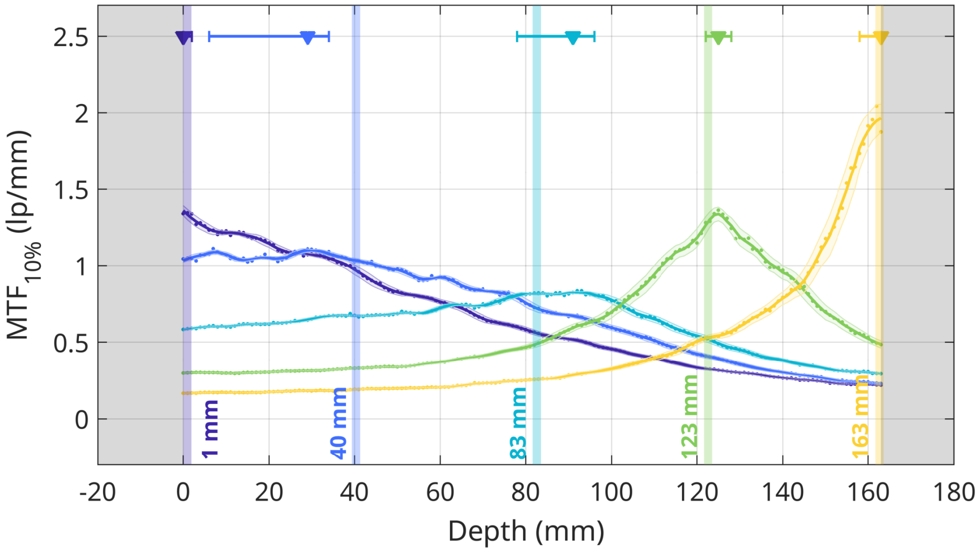

Figure 4.18: Spatial resolution against depth determined with the slanted edge method (Reichenbach et al. 1991, Fujita et al. 1992) for the experimentally acquired helium-beam radiographs. All data of one air gap position is marked with one color. For all five experiments with a certain position of the air gap (denoted by the vertical bar in the background) the spatial resolution for each reconstruction depth (dots) was determined. After smoothing the data (line) within the corresponding 2σ uncertainty (envelope), the depth yielding the maximum spatial resolution was determined (triangle). Reprinted from Metzner et al. (2025b), CC BY 4.0.

Table 4.3: Maximum spatial resolution of air gap. The air gap was positioned at five different depths. For each of the corresponding data sets, the maximum spatial resolution (SR) and the corresponding reconstruction depth (RD) were determined. Reprinted from Metzner et al. (2025b), CC BY 4.0.

Depth of gap in experiment (mm)	Maximum SR (lp/mm)	Corresponding RD (mm)
$0.0 - 1.9$	1.36 ± 0.04	0^{+2}_{-0}
$39.4 - 42.3$	1.099 ± 0.010	29^{+5}_{-23}
$81.7 - 83.6$	0.823 ± 0.007	91^{+5}_{-13}
$121.7 - 123.6$	1.34 ± 0.05	125^{+3}_{-3}
$161.7 - 163.6$	1.97 ± 0.09	163^{+0}_{-5}

at 40 mm, the estimate lies outside of the uncertainty interval. Additionally, all depth estimates deviate by less than 11 mm from the actual gap position.

In table 4.3, the maximum spatial resolution for the five gap positions is shown as well as the respective reconstruction depth. The qualitative trend of the spatial resolution for the different gap positions agrees with the one presented in table 4.2 for the simulations. Only the values in the first half of the phantom display a less pronounced decrease compared to the simulations. Qualitatively, the spatial resolution is overall worse than in the simulations. The reasons for these observations are discussed in section 5.4.2.

Advancement of the 2.5D imaging methodology towards object-agnosticism

Since the previously used methodology (sections 4.4.1 to 4.4.4) just works for images containing a slanted edge, the same data set was also evaluated with another approach: the Tenengrad metric (see section 3.10.4). It is based on the Sobel filter, which can be applied along both lateral directions to approximate the discrete first derivative within each pixel (Tenenbaum 1971, Schlag et al. 1983, Danielsson and Seger 1990). Since this method is solely based on matrix operations, it can be applied to any kind of image. Thus, in contrast to the slanted edge method, it is applicable to images of anthropomorphic phantoms.

Analogously to fig. 4.18, in fig. 4.19 the spatial resolution – now determined with the Tenengrad score – is plotted against depth. The depth of the maximum spatial resolution for each data set is marked with a diamond. Figure 4.19 exhibits visual similarity to fig. 4.18. The only obvious difference is that the Tenengrad data seems to be noisier.

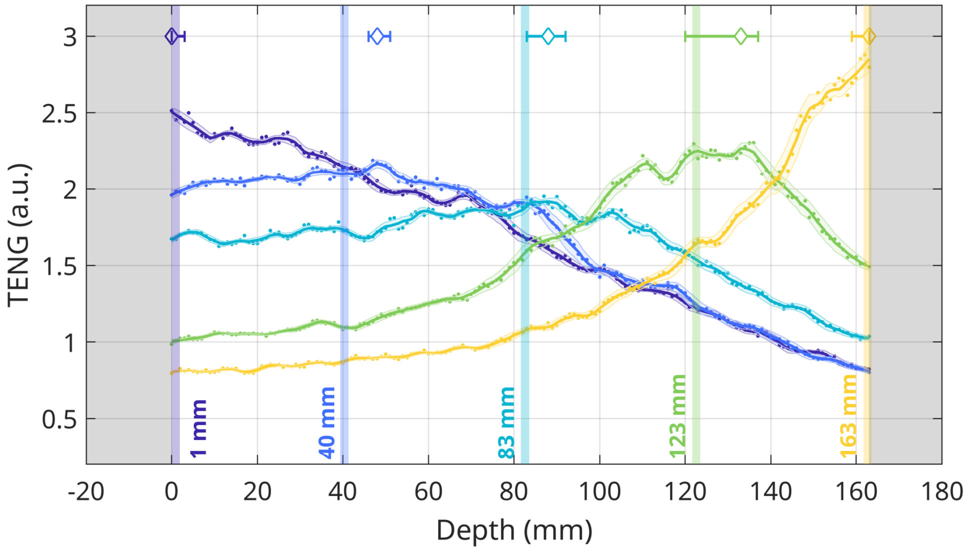

Figure 4.19: Spatial resolution against depth determined with the Tenengrad method (Tenenbaum 1971, Schlag et al. 1983) for the experimentally acquired helium-beam radiographs. All data of one air gap position is marked with one color. For all five experiments with a certain position of the air gap (denoted by the vertical bar in the background) the spatial resolution for each reconstruction depth (dots) was determined. After smoothing the data along depth (line) within the corresponding 2σ uncertainty (envelope), the depth yielding the maximum spatial resolution was determined (diamond). Reprinted from Metzner et al. (2025b), CC BY 4.0.

To compare the two methods quantitatively, in fig. 4.20, the accuracy values of the depth estimates are shown for both approaches. Here, the difference between the depth of the maximum spatial resolution and the actual experimental depth is plotted as a measure for accuracy. Additionally, the accuracy of ± 1 cm, which we are aiming to achieve for clinical use, is marked with the two dashed lines. All points agree with the ground truth depths within the uncertainty intervals except for the gap at 40 mm. Additionally, all accuracy values are below 11 mm and therefore are acceptable if a centimeter precision is aimed for.

Since both approaches, yield a similar accuracy, the Tenengrad score is a compelling alternative methodology for the 2.5D imaging method. It performs equally well compared to the well-established slanted edge method in the restricted scenario of application required by the latter. Since the Tenengrad score can be applied to a wider range of imaged objects, we continue with this approach to test the potential of the 2.5D imaging method for anthropomorphic phantoms.

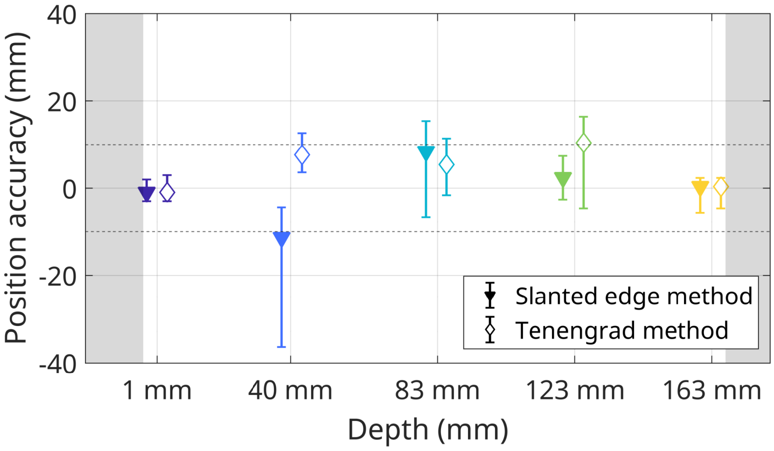

Figure 4.20: Accuracy of the 2.5D imaging method. The difference between the actual depth of the air gap within the phantom and the one determined with the 2.5D imaging method is shown for both the slanted edge and Tenengrad method for all five gap positions. Reprinted from Metzner et al. (2025b), CC BY 4.0.

2.5D imaging of anthropomorphic phantom

In fig. 4.21(a), the region of the anthropomorphic phantom which we imaged to test the 2.5D imaging method is marked with the red rectangle in the projection of a CT scan. In (b), the helium-beam radiograph of this region within the phantom in its standard configuration is shown. For this image, the along-path reconstruction was utilized in order to show the region with as little noise as possible[5]. For (c), the experiment was repeated. However, before the acquisition of this image, a silicone insert was positioned within the nasopharyngeal cavity (Schweins et al. 2025). Three pixels in the upper right corner of this image are empty. This is due to the image registration by means of which a rotation of 1.5 ° and translations of 0.01 mm and 0.20 mm were corrected after the repositioning of the modified phantom. If fig. 4.21(b) and (c) are compared with each other, the middle right of the picture seems to differ. Pixels in this region which were blue in (b) are yellow or green in (c). In (d), the difference image between (b) and (c) is shown, which extracts the WET of the anatomical change. Based on this image, it can be stated that the silicone insert, which had a maximum WET of around 8 mm along the beam direction, is easily visible. Anatomical changes of this size are therefore clearly detectable with the presented imaging system.

---

[5] The along-path reconstructed (APR) images contain less noise compared to the plane-of-interest binned (PIB) images used for the spatial resolution determination (Collins-Fekete et al. 2016, Gehrke et al. 2018a, Volz et al. 2020a)

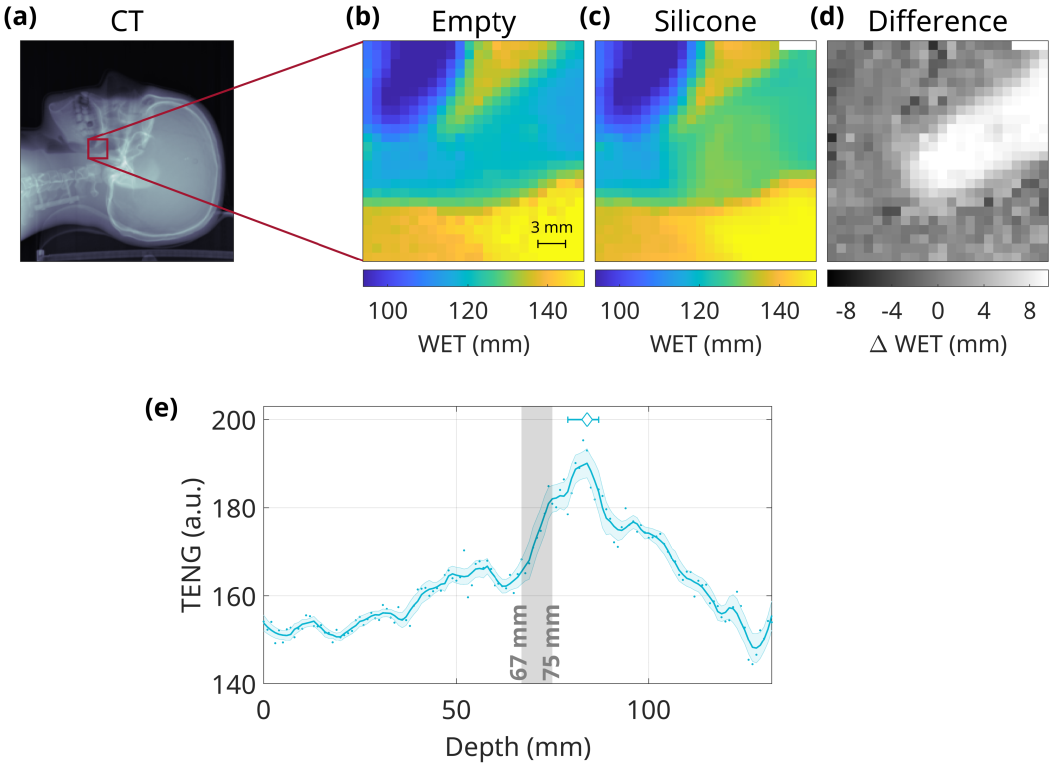

Figure 4.21: 2.5D imaging method demonstrated in an anthropomorphic phantom. (a) Imaged region of the phantom highlighted with a red rectangle in a projection of the CT scan, (b) helium-beam radiograph of the phantom with empty cavities, (c) helium-beam radiograph of the phantom with silicon insert in nasopharyngeal cavity, (d) difference image showing the change due to the silicone insert, (e) spatial resolution determined with the Tenengrad method (Tenenbaum 1971, Schlag et al. 1983) plotted against depth (dots). The smoothed curve (line) is shown together with its uncertainties (envelope) and the depth corresponding to the highest spatial resolution is marked with a diamond. The actual depth of the silicone insert within the phantom is marked by the vertical gray bar in the background. Reprinted from Metzner et al. (2025b), CC BY 4.0.

Based on the two data sets of the phantom with an empty and filled cavity, the Tenengrad analysis was conducted in the same way as for the PMMA phantom. First, the difference PIB images were reconstructed along the depth of the phantom with 1 mm spacing. Then, the spatial resolution was determined by means of the Tenengrad score. This score is shown in fig. 4.21(e) and marked by one dot per depth. The smoothed curve (line) together with its 2σ uncertainty (envelope) was calculated. Based on this, the maximum spatial resolution and the corresponding depth (diamond) were obtained as a measure for the actual depth of the anatomical change in the experiment.

In this way, a depth of 84^{+3}_{-5} mm was determined as the estimate based on the 2.5D imaging method. Comparing this value to the position of the center of the 8 mm thick silicone insert at a depth of (71 ± 2) mm, an accuracy value of 13^{+5}_{-7} mm was reached.

It was shown that the 2.5D imaging method is capable of extracting depth information from a change within helium-beam radiographs of an anthropomorphic phantom. The envisaged accuracy in the order of a centimeter could be approximately reached. Without causing additional dose to the patient, the 2.5D imaging method can be applied to judge whether or not an anatomical change detected by means of ion-beam radiography affects the dose distribution of an ion-beam radiotherapy treatment.

5 Discussion

This work established essential methods for a helium-beam radiography system based on thin detectors developing it towards applicability in the daily verification of patient anatomy prior to ion-beam radiotherapy treatments. Scatter filtering, energy painting, benchmarking of WET accuracy against clinical imaging modalities and 2.5D imaging were implemented and experimentally assessed within the scope of this PhD thesis. By presenting these methodological advancements, a potential clinical use of the system for detection, quantification and 3D localization of realistic anatomical changes was demonstrated.

In this chapter, the results presented in chapter 4 are discussed and interpreted regarding their relevance for a potential future application of the ion imaging system. Additionally, whenever feasible, the findings are compared quantitatively with peer-reviewed publications. The main sections follow a structure analogous to chapter 4, with an additional final section discussing the remaining limitations of the detection system that must be addressed before a potential clinical application.

5.1 Scatter filtering

This section is based on Metzner et al. (2024a).

Extent of scatter in data

To facilitate an assessment of the extent of scatter in our experimentally recorded data, the number of ions with specific reconstructed path lengths was shown in histograms in fig. 4.1 . It was concluded that only around 0.03% of the ions deviate by more than 1 mm from the shortest possible path.

Several reasons contribute to the small extent of scattering within our data. Most importantly, our data was recorded with a geometric bias: only ions which are detected on all six detectors are taken into account. Therefore, ion hits on the front tracker are discarded in case the ions scattered outside of the 2 cm^2 field of view, were not detected on the rear tracker or energy deposition unit and as such are incompletely sampled. Furthermore, we use higher initial beam energies for imaging than for treatments, even more so since we use an energy degrader (see section 3.3). Thus, the ions are fast within the phantom and not affected as much by scattering between the tracking units (see β dependence in eq. (2.1.15)).

Reconstructed ion paths with extraordinary length

In fig. 4.1(b), single entries for path lengths exceeding the minimum path by more than 90 mm (50 %) could be seen. This would correspond to a total traversed WET of around 285 mm within the phantom[1] and thus, an additional 39 mm within the detection system. Since an initial beam energy of 188.07 MeV/u was used for the experiments, the ions have a mean range of 235 mm. Hence, it is extremely unlikely that these ions indeed traveled along these long paths.

A more realistic explanation for these cases is large-angle scattering within the detectors. The path of these ions is reconstructed based on a wrong assumption for the incident or exiting angle and can therefore be bent by a large extent. Another explanation for these long paths is a mismatching of ion hits between the six detectors. The number of ions with these particularly long paths is on the order of the one expected for mismatched events.

In the images shown in fig. 4.2, it seems like data outside of the field of view of the detectors was recorded – which is by definition not possible. Instead, this outlying data is caused by the bent estimated paths of the ions within the phantom. Some ions first scatter out of the field of view and then back into it such that they still hit all detectors. Due to the along-path reconstruction (see section 3.4), one ion with a highly curved path, which laterally extends over many pixels, can contribute to 50 different pixels in the final image. Outside of the field of view, this can look like a "ray" of pixels with the same color as visible in fig. 4.2(a). Because no other ion contributed to these pixels, the mean energy deposition there equals the contribution of this one single ion.

Effect of scatter filtering on image characteristics

Figure 4.3 showed the effect on the image characteristics if a different number of ions is discarded based on their path length. In this logarithmically scaled plot, a plateau for

---

[1] Assuming the RSP of PMMA since it is very unlikely that ions which left the phantom scattered back towards the detectors.

SR, CNR and energy deposition could be seen for small filtering thresholds. If fig. 4.3 is plotted against a linear filtering threshold, the curve for both the SR and CNR reveals a linear dependency. In contrast to that, the negative slope of the energy deposition curve decreases with increasing linear filtering threshold. This is expected since the ions with very long paths have undergone mainly (non-charge-changing) nuclear interactions leading to high energy losses within the phantom and consequently in the sensitive volume of the detector. If these ions are filtered out, the mean energy deposition is influenced.

We can conclude that the spatial resolution does improve with an increasing filtering threshold. Unlike expected, no steep improvement for small thresholds can be observed. Probably, the lack of this effect is partly due to the inherent geometric filtering of our detection system with its small field of view. By choosing a filtering threshold of 1 %, we further removed extreme outliers including a very small number of wrongly matched signals, i.e. signals in the six detectors that share time stamps within the coincidence window but were not caused by a single helium ion. The reduction of outliers could be impressively seen in fig. 4.2.

Comparison to scatter filtering based on difference angle of Schulte et al. (2008)

In contrast to our filtering based on the path length, most other groups use filtering thresholds based on the difference angle between incident and exiting direction (Schulte et al. 2008). In fig. 5.1, the quantity that we use to filter our data is compared in a histogram with the approach used by Schulte et al. (2008).
Here, it can be seen that the majority of ions have small difference angles and path lengths close to the target thickness of 163.6 mm. Furthermore, a correspondence between the two quantities can be seen which is visualized by the white patch for high difference angles, but small path length. Here, not a single entry can be found. This is caused by the calculation of the path length: both entry and exit angles are used as input parameters together with the entry and exit positions. It is therefore mathematically not possible to use a large difference angle as input, but still obtain a short path.

However, as it can be seen in fig. 5.1 there are cases in which ions have rather long paths, but small difference angles. On the rear tracker, ions can be detected laterally far away from where one would expect them based on the position and angle measured at the front tracker. While the corresponding reconstructed paths in these cases reflect this scenario, the difference angle does not necessarily do so. In fig. 5.1, the 1 % filtering

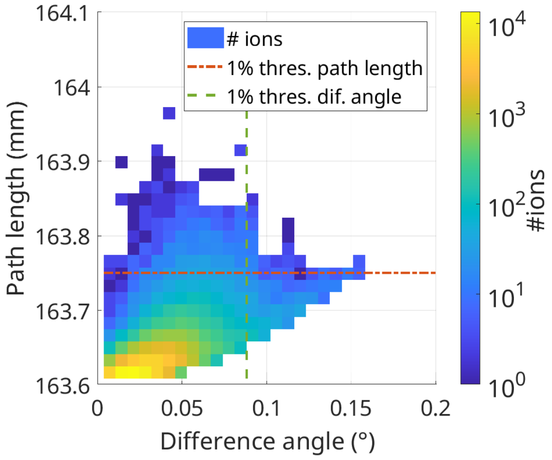

Figure 5.1: Comparison of the scatter filter criterion presented in this thesis vs. the widely adopted one of Schulte et al. (2008). In the bivariate histogram, all recorded ions are binned according to their reconstructed path length and difference angle between front and back tracker. Additionally, a 1 % filter threshold is shown for both criteria. The experiment was conducted with a 163.6 mm thick PMMA phantom. Path length and difference angles were calculated based on the measured tracking information.

thresholds for both criteria visualize that these cases are not filtered out if the approach of Schulte et al. (2008) is followed.

We can conclude that the two filtering quantities are both suitable for omitting most ions with a large extent of scattering. However, the filtering based on the difference angle does not incorporate any position information, which can also yield important information regarding scatter. We therefore recommend a filtering based on the path length to take all information available from the trackers into account.

5.2 Energy painting

This section and its sub-sections are based on Metzner et al. (2024b).

A fundamental challenge had to be addressed before the detection system could be advanced towards the imaging of anthropomorphic phantoms: the limited WET range within which a clinically sufficient precision can be achieved. This constraint is a consequence of building the detection system exclusively from thin detectors and, in turn, reducing its physical footprint and complexity.
To enable high precision WET imaging of heterogeneous phantoms, the energy painting

method was introduced utilizing multiple initial beam energies[2]. After the quantitative assessment of the required calibration curves, the energy painting method was tested for a wedge phantom and its performance was evaluated. The corresponding results from section 4.2 will be discussed in the following.

5.2.1 Calibration of detector signal for quantitative WET measurements

In order to be able to apply the energy painting algorithm and to obtain clinically relevant, quantitative images, calibration curves are required. These curves translate the detector signal to water-equivalent thickness (WET). The establishment and performance of calibration curves acquired with our system were already discussed in Knobloch et al. (2022), Metzner (2022). However, for the energy painting method presented in this work, completely new curves were acquired. Therefore, the resulting curves from section 4.2.1 are shortly discussed in this section.

The measured calibration curves shown in fig. 4.4(a) spanned a WET range from around 120 mm to 230 mm. The shape of the curves reflected the measurement principle of our detection system: the steep rising edge of the Bragg peak is probed with our thin detector. Thus, the energy steeply increased with increasing WET. The fit described the data points well. Consequently, the residuals of the fit were low with a maximum RMSD of 0.25 mm. This value is similar to the 0.18 mm reported in Knobloch et al. (2022) which confirms the reproducibility of the methodology.

The fact that the mean accuracy value showed a minor negative offset might originate from the symmetric 3σ cut in the asymmetric energy deposition distribution favoring lower WETs.
The precision values as a function of WET follow the expected pattern for each initial beam energy considering the course of the steepness in the rising edge of the Bragg peak. This trend reveals the need for the energy painting method in order to circumvent the deteriorating precision values for smaller WETs.

---

[2] Similar to Dickmann et al. (2021b), DeJongh et al. (2021), Telsemeyer et al. (2012), Sarosiek et al. (2021) who employed several energies to solve challenges connected to their specific detectors and applications.

Temporal stability and radiation hardness

Four independent measurements for the accuracy determination were acquired, 3 and 89 days later. The maximum accuracy value of $(0.29 \pm 0.08)\,\%$ indicates that no daily acquisition of calibration curves or correction of the detector signal is needed in contrast to other systems (Dickmann et al. 2021a) which represents a major advantage for clinical use. Within the 89 days, the detector responsible for the image contrast was irradiated with around 2 Gy. This corresponds approximately to the cumulative dose deposited in the detector by the acquisition of at least 100 helium-beam radiographs in case of a synchronization of the detector's dead time with the beam.

Comparison of accuracy with values in literature

Since the accuracy should theoretically not depend on the type of ion, we can put our accuracy values into perspective with values published for proton-beam radiographs. Sarosiek et al. (2021) reported 0.33 % for a phantom with a thickness of only around 60 mm, while Krah et al. (2018) obtained 0.7 % for a 200 mm phantom. Compared to them we reach competitive values. To the author's knowledge, no WET accuracy values were published for experiments with helium ions yet. Bär et al. (2022) reported a mean RSP accuracy of 0.3 % for their helium CT images acquired with the US pCT phase 2 scanner. Due to the homogeneity of their samples, this should translate to an equal accuracy in WET. In this case, their reported values are on par with ours, since both reached a similar WET accuracy of around 0.3 %.

No single-ion WET precision (SIWP) published for helium-beam radiography could be found. A comparison to precision values published by other groups for a proton beam is not as straightforward since the SIWP depends on the ion type, but will be presented nonetheless in the next section together with the precision of the energy painting data.

5.2.2 Experimental assessment of the energy painting method

The energy-painted radiograph of a wedge phantom was shown in fig. 4.6a. With the assumptions explained in section 3.6, the dose of this image was estimated to be around $(700 \pm 500)\,\mu\text{Gy}$.

The deviations of the profile from a linear fit exhibited a periodicity of 12 mm. This value corresponds to the lateral shift of the detector conducted in the experiments to obtain a radiograph larger than the detector's field of view. This indicates that the residuals are caused by detector inhomogeneities and edge effects. However, deviations were far below 1 % and the slope of the fit (1.1564 ± 0.0021) corresponded well to the expected RSP of 1.1611 ± 0.0028. Therefore, the deviations due to detector inhomogeneities were classified as being of secondary importance.

Precision improvement

The behavior of the calibration curves in fig. 4.4 demonstrated that the precision deteriorates if only one initial beam energy and a detection system based on thin detectors is used for the imaging of a heterogeneous object. The purpose of the energy painting algorithm is to facilitate high-precision imaging of all clinically relevant imaged objects with detection systems based on thin detectors.

In the respective analysis, it was shown that the energy painting approach improved the mean precision by a factor of 2.49 ± 0.16 compared to the monoenergetic acquisition method for the presented case. If instead the CNR is kept constant, this improvement in precision would enable imaging with a six times lower dose.

The single-ion WET precision (SIWP) was investigated for the energy-painted image in fig. 4.5(b), while a similar plot was shown for the calibration curves in fig. 4.4(d). Thus, the two results are displayed together in fig. 5.2. For both ways of analyzing the SIWP, similar values between 0.9 % and 4 % were reached in the WET interval of 150 mm to 220 mm.

Comparison of precision with values in literature

Analogous to Metzner (2022), a comparison of the single ion WET precision with values found in literature is shown in fig. 5.2.
No published SIWP values could be found, which were obtained from experimental data with a helium beam. In order to still facilitate a comparison, the values achieved with the state-of-the-art US pCT phase2 scanner, a proton beam and two different phantoms (Bashkirov et al. 2016, Dickmann et al. 2019) can be considered. Since the aim is to compare the precision capabilities of different detection systems, effects stemming from a different choice of ion type should be eliminated. Therefore, the values reported for the US pCT system are converted to pseudo-helium values in the following.

Two effects need to be considered for this translation. First, protons provide overall worse precision due to the increased range straggling σ_{RS} compared to helium ions. Secondly, fragmentation of helium ions can lead to increased noise. Since it is difficult to predict the influence of the second factor, we neglect it and assume the US pCT

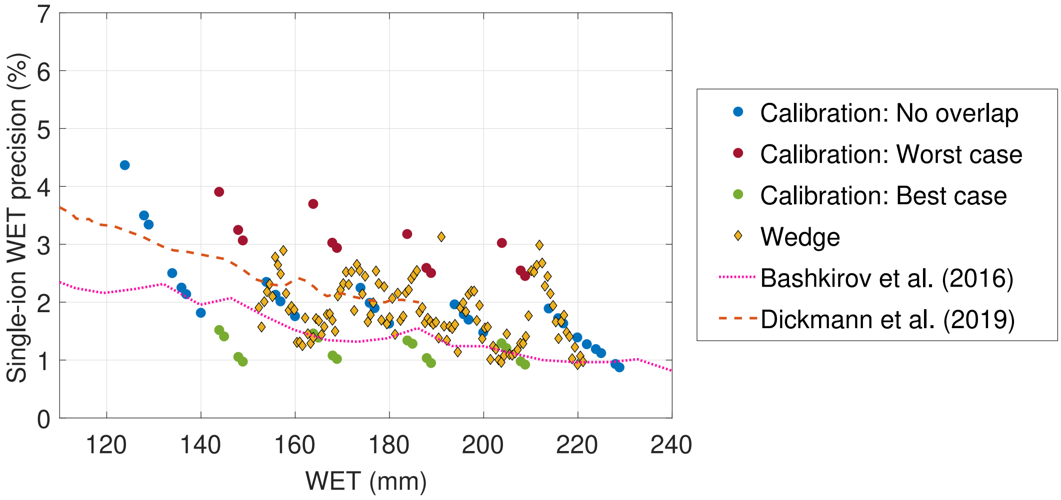

Figure 5.2: Comparison of single-ion WET precision (SIWP) determined with calibration (fig. 4.4(d)) and wedge phantom (fig. 4.5(b)) with values from literature. The values of Bashkirov et al. (2016), Dickmann et al. (2019), which were acquired with the pCT phase 2 scanner and a proton beam, were adjusted such that the uncertainty due to range straggling of protons is reduced to that of helium ions.

phase2 scanner to perform equally well for helium ions. We therefore obtain a rather conservative estimate assuming there is solely an improvement for the US pCT scanner due to reduced range straggling when changing from proton to helium-ion beams. For the conversion, we obtain (Knobloch et al. 2022, Metzner 2022, Metzner et al. 2024b)

$$\sigma_{\mathrm{WET},\alpha} \approx \sqrt{\sigma^2_{\mathrm{WET},p} - 0.75\,\sigma^2_{\mathrm{RS},p}}\,. \tag{5.2.1}$$

In fig. 5.2, the converted data from Bashkirov et al. (2016), Dickmann et al. (2019) is compared to the one achieved within this thesis. The curves obtained from the US pCT scanner are overall more stable over WET since they used only one initial beam energy in a combination with a calorimeter/range detector. The oscillating pattern in their curves is caused by the different stages of the calorimeter (Bashkirov et al. 2016).

If we use our calibration curves for the highest WETs only, we can exceed the precision of the US pCT scanner and achieve even lower precision values than this system. For most of the WETs however, our system performs less precisely than the conservatively converted US pCT scanner in the scenario of Bashkirov et al. (2016). Comparing our values to the study of Dickmann et al. (2019), on average both systems perform approximately equally well. Consequently, our developed imaging system exhibits a WET precision competitive with this state-of-the-art imaging system.

Further improvements and considerations

The precision of our system could be improved further by increasing the number of used initial beam energies. In that way, the interval of the steep rising edge of the Bragg peak utilized for imaging is reduced even further, leading to overall greater WET sensitivity. However, the practicability also must be kept in mind. The energy switching times of the accelerator and the high calibration effort must be balanced against the gain in precision, which was already shown to be competitive with the US pCT scanner as state-of-the-art detection system.

The current implementation of the energy painting method is based on the subsequent acquisition of ROIs with initial beam energies tailored to the WET distribution expected from the planning CT. If the ROI is inhomogeneous, several initial energies must be used and some of the data must be discarded during the post-processing to ensure that only WET values within the high-precision interval are taken into account. The energy painting approach could be improved by the segmentation into smaller ROIs, preferably with a size of the FWHM of the narrowest pencil beam. In that way, the limits for the single energies could be realized by means of the beam plan instead of the post-processing and the dose could be reduced even further.

The application of the energy painting algorithm requires an estimate of the WET distribution within the imaged region as this information is essential for optimizing the choice of initial beam energies. Consequently, without this prior knowledge, energy painting cannot be employed for high-precision imaging.
The foreseen clinical use for our helium-beam radiography system would be daily monitoring of the patient's anatomy before each ion-beam radiotherapy treatment fraction. Thus, the X-ray planning CT, which is acquired of each patient before the first fraction of the treatment, can be used to obtain this prior knowledge. Hence, it is no limitation for the envisaged clinical application.

In case a severe anatomical change occurs between the planning CT and the acquisition of the radiograph, the chosen energies might not match the WET distribution anymore. In order for this to happen, WET changes of more than 10 mm have to occur. In these cases, the image quality might be negatively impacted. However, the image could still be used to deduce that a severe anatomical change occurred thus still fulfilling its purpose.

So far, the energy painting method was only used for the imaging of static targets due to the limited speed of the detection system (see section 5.5) and a future clinical application is envisaged in body parts with negligible intra-fractional motion, accordingly. For moving targets, motion artifacts might occur. If the data of each energy is acquired subsequently, there could be shifts or more complex transformations between the mono-energetic images. How the energy painting method can be applied to moving targets should be studied in future investigations.

Relevance for future clinical application

The energy painting method was experimentally assessed and shown to enlarge the WET interval within which high-precision imaging is feasible with the presented helium-beam imaging system. The method therefore overcomes a limitation of the system which prevented imaging of anthropomorphic phantoms so far and therefore advances the system towards imaging of clinically more relevant phantoms.

5.3 Imaging of anthropomorphic phantom and comparison to clinical X-ray CT modalities

This section and its sub-sections are based on Metzner et al. (2025a).

After the thorough validation of the energy painting method in the previous sections, it was finally applied to image an anthropomorphic phantom. The resulting helium-beam radiograph was compared to WET-maps based on clinically used X-ray CT modalities.

We chose the imaged region at the skull base due to several reasons. First of all, it is a relevant site for ion-beam radiotherapy treatments. Furthermore, it is a heterogeneous region containing many different tissue types, which cause interesting and complex structures within the image. Because of the cavities present in the imaged region, also significant changes can occur during treatments, e.g., due to tissue swelling or mucus. This makes the region especially relevant for our envisaged clinical application of monitoring the patients' anatomy. Moreover, the heterogeneity of tissue within the region makes accurate imaging especially challenging causing our estimate to rather represent a cautious estimate for the accuracy of our system in anthropomorphic phantoms avoiding understating the quantity.

The accuracy of the helium-beam radiograph presented in fig. 4.7 was shown to be competitive with the ones based on the two X-ray CT modalities. The gamma analysis revealed similar passing rates above 70 % despite strict criteria based on the uncertainties of the reference scan. If the criteria are relaxed to 2 %, 2 mm or 3 %, 3 mm, approximately 95 % or 99 % of the pixels of all three modalities pass.

Compared to the WET accuracy determined with the calibration and wedge phantom in the previous sections, the value of $(1.46 \pm 0.06)\,\%$ for the helium-beam radiograph of the anthropomorphic phantom is significantly higher. However, due to the increase in complexity of the phantom, the value still seems plausible. For the same region, a WET accuracy of $(1.19 \pm 0.05)\,\%$ and $(1.30 \pm 0.06)\,\%$ was reached for DECT-DirectSPR and SECT-HLUT, respectively.

In general, a strong correlation of the deviations in WET with a high abundance of low-density materials in the beam path was found for all three imaging modalities under investigation. The WET was often overestimated where a large fraction of sinus cavity and air occurred. Similarly, a strong anti-correlation with high-density materials was observed, e.g., for cortical bone. Both observations agree with the findings of Wohlfahrt et al. (2018), who determined the same tendency for their SECT-HLUT and DECT-DirectSPR scans.

Choice of imaging modalities for comparison

It would be interesting to compare the WET accuracy of our helium-beam imager to that of cone-beam CT since this is another imaging modality foreseen for daily positioning and anatomy verification. Therefore, these modalities, which compete for closing the same gap in the workflow of ion-beam radiotherapy treatments, would be better suited for a direct comparison in all parameters.
Unfortunately, to my knowledge, no standardized procedure is established yet for the verification of the patient's anatomy based on cone-beam CTs (Herrick et al. 2023). Therefore, we decided to compare our WET accuracy to X-ray CT scans complying with the recently established consensus guide (Peters et al. 2023). These scans are meaningful for our comparison since the guidelines are used to standardize the CT acquisition protocols for many centers. Previously, the inter-center variation in RSP prediction based on SECT-HLUT was found to be above 2 % (Peters et al. 2021) and might still be similar for the currently used cone-beam CTs. Therefore, we opted for a comparison with the standardized CT scans, accepting their advantages as a consequence of the higher radiation dose.

Dose

The helium-beam radiograph in this work was acquired with a dose of $(290 \pm 190)\,\mu\mathrm{Gy}$, which is a dose comparable to that of X-ray projections used in some centers for the patient positioning right before treatment start (Steiner et al. 2013). Therefore, it is perceived as a realistic dose for the envisaged purpose of clinical daily positioning and simultaneous verification of the patients' anatomy. If we reconstruct the image with a dose of around 100 µGy, the RMSPE marginally increases from (1.46 ± 0.06) % to (1.52 ± 0.07) %.

The dose of the X-ray CT modalities used for the presented assessment of WET accuracy was nearly 100 times higher, amounting to 24.9 mGy (SECT-HLUT) and 11.1/12.7 mGy (DECT-DirectSPR), respectively. Naturally, these scans have a much wider variety of possible use cases (e.g., diagnosis, treatment planning), primarily due to them obtaining 3D information. It is, of course, reasonable that these tomographic scans cause a higher dose to the patient than a single helium-beam radiograph. Still, considering the dose for our comparison regarding the WET accuracy, it is an important fact to be pointed out.

Comparison of WET accuracy for anthropomorphic phantoms with literature

Since we could not find published WET accuracy values achieved for experimentally acquired helium-beam radiographs of anthropomorphic phantoms, we need to consider related quantities in order to facilitate a comparison. As we are interested in WET, which corresponds to the integrated RSP along beam direction, the range is an interesting quantity to compare it with. It corresponds to the WET the ions had traversed until they stopped. Therefore, only the integration interval is what differs between the two quantities.

Volz et al. (2021) found a range accuracy of -0.29 % (helium CT), -1.40 % (SECT) and -0.45 % (DECT) for a total range amounting to around 80 - 90 mm. Wohlfahrt et al. (2018) published values ranging between -0.3 % and 0.1 % for SECT-HLUT and 1.1 % to 1.7 % for DECT-DirectSPR considering approximately the same particle range as Volz et al. (2021).
Of course, these reported values were determined for different geometries and beam paths and in the case of Volz et al. (2021) even a different phantom. Most importantly, they were determined for overall shorter integration intervals. Thus, we consider our accuracy of 1.46 % for a mean WET of 135 mm to be approximately on par with these published ones.

Interestingly, the RMSPE found in our study for the SECT-HLUT scans is smaller than the often-cited range uncertainties of 1.5 % – 1.7 % (Paganetti 2012)[3]. Furthermore, it is very similar to the one of DECT-DirectSPR, which opposes the findings of many studies

---

[3] In the original publication of Paganetti (2012) they report 2.3 % – 2.6 % for a 1.5σ interval. Since we report 1σ intervals, we converted the values correspondingly.

(Van Elmpt et al. 2016, Bär et al. 2017, 2018, Wohlfahrt and Richter 2020, Longarino et al. 2022).
A reason for this could be that the tissue-equivalent materials in the phantom might have been very similar to the ones which were used to establish the HLUT. Therefore, the materials lie closer to the interpolated lines than human tissue would. This fact unnaturally improves the accuracy of the SECT-HLUT.

Contributions of reference to WET deviations

In the study at hand, it was assumed that the reference scan represents the ground truth RSP map facilitating the assessment of the accuracy between different imaging modalities. However, especially in fig. 4.8 and fig. 4.9 it becomes apparent that all imaging modalities deviate from the reference scan with the same trend. This raises the hypothesis that the reference scan might have caused a non-negligible part of the deviations rather than the imaging modalities themselves. Three facts supporting this hypothesis are presented in the following:

- The reference data set consists of only nine discrete RSP values which leads to a perfectly sharp WET-map. However, voxels at interfaces of different materials are likely to contain a mixture of several materials. Still, during the segmentation, these voxels are assigned one of the nine RSP values. This partial volume effect can therefore lead to slightly shifted edges between two materials and therefore deviations in WET from the ground truth. However, this effect should be minor due to the very small original voxel size (0.5 mm in all three dimensions) of the reference scan.

- Some of the differences between the imaging modalities and the reference are caused by a different spatial resolution. Due to scattering of X-rays and ions in matter, the spatial resolution of the imaging modalities under investigation is naturally impaired. In contrast to these, the reference map is only limited by its voxel size as the assigned RSP values of the nine involved materials can be assumed to be perfectly known. Figure 4.10 indicated that the reduced spatial resolution of the SECT-HLUT and DECT-DirectSPR scan causes an underestimation of high-RSP materials and an overestimation of low-RSP materials due to blurring. This effect can therefore explain the deviations to some extent.

  In our original study, we did not want to compare the imaging modalities to a reference, which had been artificially blurred to exclude effects stemming from the spatial resolution. Instead, we wanted to present an end-to-end WET-accuracy

assessment explicitly keeping effects related to spatial resolution as part of the investigation.
However, to facilitate a discussion of the effect of the spatial resolution on the WET accuracy, in section A.1 in the appendix the corresponding plots for a reference with decreased spatial resolution are shown. In the results presented there, we can clearly see that the blurring of the reference changes the results and reduces the WET deviations between all investigated modalities and the reference (see table A.1). Furthermore, the high-density materials as measured by αRad are less underestimated and vice-versa for the low-density materials. We can therefore conclude that the difference in spatial resolution is responsible for the deviations in WET to some extent. However, the blurring does not compensate for all deviations.

- Wohlfahrt et al. (2018) verified the reference RSP data set with multi-layer ionization chambers finding a MAPE and RMSPE corresponding to around 0.8 % and 1 %, respectively[4]. Comparing these values with the ones determined for our imaging modalities, we can state that the uncertainty of the reference itself reaches a contribution of around 60 % - 80 % of the MAPE and RMSPE.
  Despite these substantial uncertainties, the reference established by Wohlfahrt et al. (2018) is currently considered to yield the gold standard RSP values for anthropomorphic phantoms. This lack of RSP references for heterogeneous objects with uncertainties significantly lower than the ones of the imaging modalities under investigation indicates the latter to yield an accuracy close to the limit of what is currently technically achievable.

Relevance for future clinical application

A helium-beam radiograph of an anthropomorphic phantom was acquired utilizing the energy painting method. While depositing a low dose in the phantom (290 µGy), it still reached a WET accuracy competitive with the one of clinically used CT modalities. The RMSPE of the helium-beam radiograph of (1.46 ± 0.06) % is less than the usually applied safety margin around the tumor volume (commonly around 3.5 %) (Paganetti 2012, Taasti et al. 2018). This indicates that the presented helium-beam imager is a promising imaging modality for low-dose daily verification of patient anatomy. Thus, it opens up the possibility of reducing the safety margins used for ion-beam radiotherapy treatments.

---

[4] Estimated for the distribution in Figure 3, Half head Field A in Wohlfahrt et al. (2018) which is most similar to our field geometry.

5.4 2.5D Imaging

Enabled by the advancements demonstrated within the previous chapters, ion-beam radiographs acquired with our compact system could be used for the quantification and lateral localization of anatomical changes right before the treatment. With this information, the impact of a change on the treatment can be assessed in a well-informed way. The only information lacking to attain a fully comprehensive assessment of the situation is whether the change happened within the treatment field or behind it, where it would only affect the ions used for imaging and hence would not be relevant for the treatment quality.

Thus, the 2.5D imaging method was investigated in section 4.4 to enable a rough depth estimation based on helium-beam radiographs with an accuracy on the order of a centimeter. At first, the potential performance was assessed in simulations to advance the preceding work of Volz et al. (2024). Then, the 2.5D imaging approach was evaluated in experiments with two different phantoms of increasing complexity. The respective results presented in section 4.4 will be discussed in the following.

5.4.1 Monte Carlo simulations with a proton and helium beam

In a recent publication, the 2.5D imaging method had been investigated in simulations with a proton beam and perfect detectors right at the surface of a water phantom with homogeneous bone cubes inside (Volz et al. 2024). There, the method yielded promising results.

To bridge the gap to more realistic conditions, ion-beam radiographs with a setup which was later also realized in experiments were simulated in this PhD project. For this purpose, an implementation of our detection system and the homogeneous PMMA phantom with an air gap were used, which were both previously established by Amato et al. (2020), Hermle (2025). Furthermore, the distances between all simulated parts were chosen such that they were also realistically achievable in experiments. Note that the distance between tracking detectors and imaged object can be expected to have a relevant effect on SR, especially in the context of 2.5D imaging, since pixelation and scattering uncertainties of the tracking grow linearly with distance. Since Volz et al. (2024) conducted the analysis for protons, this ion type was employed as well in our analysis to facilitate a direct comparison of the idealized and realistic setups. Eventually, the results were compared to the ones achieved with a helium beam since this ion type is foreseen for use in clinical imaging due to its overall better spatial resolution.

First and foremost, the 2.5D imaging method was demonstrated to work for the realistic geometry in the simulations. The depth of the change in the form of a 1.9 mm air gap could be determined for all five gap positions. The accuracy value of the depth estimate was below 1 cm, which fulfills the requirements for clinical use (see table 4.2 and fig. 4.16).

The simulated radiographs were quantitative in terms of energy deposition since no dE-WET-calibrations were established in the simulations. For helium ions, the experimentally obtained calibration curve could be applied to the simulated energy depositions as well. However, due to the uncertainty on the depleted volume of the detector, the resulting WET cannot be guaranteed to be accurate. Since no calibration curves are needed for the 2.5D imaging approach, this step was skipped in the post-processing of the simulations. In the difference images in fig. 4.12 and fig. 4.14, the $\Delta\mathrm{WET}$ caused by the insertion of the air gap translated to different $\Delta \mathrm{d}E$. For protons, we could observe $\Delta \mathrm{d}E \approx 0.12$ MeV, for helium $\Delta \mathrm{d}E \approx 0.42$ MeV. The around four times higher difference in energy deposition of helium ions corresponds to the theoretically expected value due to their twice as high atomic charge and therefore overall four times higher energy deposition (see eq. (2.1.2)).

Role of ion type for 2.5D imaging

Interestingly, protons and helium ions performed equally well. At first, this might seem counterintuitive since protons scatter more within the phantom, which is an important prerequisite for the method to work. However, not only the scattering but also the uncertainties on the path estimate play a crucial role for the depth accuracy. Overall, the sharpness of the spatial resolution peak determines the precision of the method, which indeed was similar for both ion types.

The 2.5D imaging method could be tested for even more ion types. There is a high interest in carbon imaging, primarily for integrating systems but also for the list-mode systems relevant for 2.5D imaging. Since carbon ions scatter even less than helium ions, it would be interesting to see how the 2.5D imaging method performs with these ions.

Comparison of contrast-to-noise ratio and spatial resolution obtained from simulations to values in literature

The mean CNR over all five gap positions was found to be 2.78 ± 0.06 in the simulated difference proton-beam radiographs reconstructed at the depth where the gap was actually located. The difference images based on the helium-beam radiographs exhibited a CNR

of 2.62 ± 0.06.
In the experimental findings of Gehrke et al. (2018a) with a different phantom and number of particles, slightly higher CNR was reached with the helium-beam radiographs compared to the ones acquired with a proton beam at the same dose. However, in the theoretical considerations of Gehrke et al. (2018a), the CNR of the two ion types was predicted to be equal. Since the difference in CNR between the two ion types is only marginal, the values are considered to be in agreement with Gehrke et al. (2018a).

The mean spatial resolution over all gap positions improved from (1.14 ± 0.26) lp/mm for protons to (2.1 ± 0.5) lp/mm for helium ions. This increase of spatial resolution of around 80 % agrees well with the 79 % reported by Gehrke et al. (2018a) for their simulated PIB radiographs. This again encourages the use of helium ions for imaging.

If we compare the absolute spatial resolution values to the ones published by Gehrke et al. (2018a) who used the same simulation pipeline, but with a slightly modified detection system and lower initial beam energies, we obtain similar trends, but up to 80 % higher spatial resolution values. This is expected, since the mentioned modification of the system was introduced in order to increase the spatial resolution (Amato et al. 2020).

Numerous other publications exist which report on the spatial resolution of proton-beam radiographs, among them Seco et al. (2013), Khellaf et al. (2022), Volz et al. (2024). However, the resulting values very much depend on the simulated phantoms and detectors, which is why a comparison is in general difficult.

5.4.2 2.5D imaging experiments with a helium beam

In the simulations, the 2.5D imaging method was shown to yield a similar depth accuracy for protons and helium ions at equal dose, while the images acquired with helium ions exhibited overall better spatial resolution. Consequently, all experiments were conducted with a helium-beam.
First, experiments were conducted using the PMMA phantom containing the 1.9 mm air gap at varying depths, as previously studied in the simulations. Afterwards, the method was modified for an application to an anthropomorphic phantom.

To study the feasibility of the 2.5D imaging method in these initial experiments, the doses of these images of the air gap phantom were chosen rather high (between (0.8 ± 0.6) mGy and (1.2 ± 0.8) mGy) (Metzner et al. 2025b).
Since experimentally acquired calibration curves were available, the difference images in fig. 4.17(a) are quantitative in terms of WET. The WET difference of (2.24 ± 0.10) mm caused by our emulated anatomical change is clearly visible in all radiographs. Therefore, it can be concluded that our system is evidently capable of resolving a 2 mm air

gap within a phantom of in total more than 180 mm WET, which confirms previous statements for the same detection system (Gehrke et al. 2018b,a). The WET of the geometric phantom could be determined with an accuracy of (0.39 ± 0.20) %, which is sufficient to classify the impact of an anatomical change on the dose distribution.

Comparison of 2.5D imaging experiments and simulations

As expected, the spatial resolution observed in the experiments was overall lower than that in the simulations. The main reason for this is the uncertainties introduced by the tracking detectors (Bopp et al. 2014), which measure the impact coordinates of the ions with a finite precision. For the front tracker, the pixelation of the detector plays a crucial role. Here, the ions deposit much less energy due to the behavior of stopping power over depth resulting in signals spreading over a few pixels only. Since bigger clusters of pixels improve the precision of the impact position measurements and the direction estimate, the front tracker is especially affected by the pixelation. On the rear tracker, the clusters span over many more pixels. Therefore, the spatial resolution in the back of the phantom is not as drastically reduced in the experiments compared to the simulations.

Another factor which contributes to an overall decreased spatial resolution is the alignment of the detectors along the beam path. Small lateral shifts and rotations of the detectors cannot be eliminated completely in a real experimental setup. Although we correct for small shifts in our post-processing, the imperfections in the alignment worsen the spatial resolution.

Additionally, in experiments we can obtain incorrect matches of the impact points on all six detectors, which is by definition not the case with the chosen settings in our simulations. Furthermore, in the simulations, we only score helium ions. In the experiment, we filter fragments based on the ion identification technique developed by Hartmann et al. (2017), Gehrke et al. (2018b). However, minor contributions of fragments with wrong path estimates cannot be ruled out completely.

Comparison of experimentally achieved spatial resolution to values in literature

This section is based on Metzner et al. (2025b).

To compare our spatial resolution values achieved in experiments with previously published ones, we can first refer to Gehrke et al. (2018a). Compared with their helium-beam radiographs acquired with a slightly modified detection system and different distances between trackers and phantom (spatial resolution between 0.5 to 2 lp/mm), we reach similar results. However, the spatial resolution in the back of the phantom is particularly improved compared to their reported values (2 lp/mm vs. 1.4 lp/mm) (Metzner et al. 2025b). This is caused by the introduction of the energy degrader between rear tracker and energy deposition detector and the respective use of higher initial beam energies (Amato et al. 2020). Due to this change, the spatial resolution is improved substantially, mainly in the back of the phantom, where the ions were previously strongly affected by scattering due to their low velocities at the end of their range.

For the ProtonVDA scanner built from scintillating fiber tracking-planes and a single-stage residual energy detector (DeJongh et al. 2021), spatial resolution values for an experimentally acquired PIB ion-beam radiograph were reported in Sarosiek et al. (2021). They reached values of up to 1.13 lp/mm in the middle of the phantom even though they used a proton beam offering inherently lower spatial resolution. On the other hand, their phantom was only 6 cm thin. In comparison to our 16.5 cm phantom this leads to a significant decrease in scatter and thus higher spatial resolution. Because of these different imaging parameters, a direct quantitative comparison with this published value is difficult.

Advancement of the 2.5D imaging methodology towards object-agnosticism

This section is based on Metzner et al. (2025b).

Since the 2.5D imaging method was successfully tested for the PMMA phantom both in simulations and experiments, a translation of the methodology towards an applicability to anthropomorphic phantoms was tested subsequently. To enable 2.5D imaging of anthropomorphic objects, which naturally do not exhibit slanted edges, the Tenengrad score was applied and compared with the previous approach.

The accuracy values of both methods were shown to lie below 11 mm for all gap positions in the PMMA phantom complying with the targeted accuracy for clinics on the order of a centimeter. All depth estimates agreed with the ground truth depth within their uncertainties, except for the gap at 40 mm. Due to the rather flat shape of spatial resolution in the front of the phantom in fig. 4.18, noise has a great impact on the depth estimate of features in the first centimeters behind the front surface. Interestingly, also Volz et al. (2024) reported the least accurate depth estimate for their shallowly positioned feature at 50 mm depth.

In this study, designed to benchmark the 2.5D imaging based on the Tenengrad score against the well-accepted slanted edge method, both approaches yielded a similar depth accuracy. Since the slanted-edge method is limited to simple objects, the Tenengrad score is concluded as a valid metric for object-agnostic imaging to proceed with.

2.5D imaging of anthropomorphic phantom

This section is based on Metzner et al. (2025b).

Lastly, the 2.5D imaging approach based on the Tenengrad score was tested for an anthropomorphic head phantom. In fig. 4.21, the resulting helium-beam radiographs with a dose of $(270 \pm 170)\,\mu\mathrm{Gy}$ were presented.
In the difference image, the additional material caused by the silicone insert can be distinctly seen. Also, its WET of up to 8 mm can be quantified by means of this image and its position can be localized laterally. Outside of the region with the silicone insert, noise is present which could stem from slightly different beam axes for the acquisition of the two radiographs since the phantom had to be taken apart and repositioned in between. Furthermore, the rather low number of particles compared to the experiments with the geometric phantom causes a higher level of noise to be present within the image.

Even for the anthropomorphic change, the Tenengrad score still exhibits a clear maximum of spatial resolution for the difference radiographs reconstructed at different depths. The maximum is slightly shifted towards greater depths compared to the actual depth where the silicone was inserted. The depth accuracy value in the anthropomorphic phantom was determined as 13^{+5}_{-7} mm, which is still in agreement with the envisaged accuracy of about a centimeter for a clinical application.

One possible explanation for the shift of maximum spatial resolution towards greater depths than that of the silicone insert is the presence of large air-filled cavities along the beam path. In tissue with water-like properties, the ion trajectories are well described by the cubic-spline path model. However, our used path formalism does not account for tissue heterogeneity and, as a result, the actual ion paths deviate from the estimated path after traversing a cavity. They gradually converge back towards the true path when approaching the rear tracker. In the reference image, the whole nasopharyngeal cavity was empty resulting in larger deviations of the path estimates than in the second image, where the rear half of the cavity was filled with the silicone insert. Therefore, the spatial resolution of the images in the depths behind the first half of the cavity slightly differ. This results in a marginally perturbed difference images with reduced spatial resolution in these depths, which could explain the shift of the maximum towards greater depths.

The piece of silicone was inserted into the nasopharyngeal cavity of the phantom since it is the only cavity which is not covered by any material if the phantom is taken apart. To image this cavity, we decided on a clinically realistic beam geometry which is often used in combination with an opposing field for the treatment of skull base tumors. The induced change of around 6 g of silicone was rather substantial. However, changes of around 8 mm in WET can occur for fast responding or growing tumors over the course of an ion-beam treatment (Barker Jr et al. 2004) and are therefore perceived as realistic.

Before the 2.5D imaging approach can be used clinically, it needs to be tested for more scenarios such that the limits of the method can be identified.
If several laterally separated changes occur within a patient, the analysis of the Tenengrad score could be performed independently for these regions. If the changes do overlap, it must be tested until which extent and distance they can both be resolved and how the methodology can be adjusted to also cover these more complicated scenarios.

The 2.5D imaging approach can be used together with any list-mode ion-imaging system. Probably, both front and rear trackers are needed in order to make the method work reliably. However, investigating the method for a variety of systems should be subject of future investigations.

In summary, the 2.5D imaging method was successfully tested in simulations and experiments with a realistic detection system for the first time. This proof-of-principle motivates further testing of the method to investigate its performance for a wide range of scenarios in order to advance the method towards clinical use.

Relevance for future clinical application

By means of the example in fig. 4.21, it was demonstrated how the detection system for helium-beam imaging could be used in clinics. It was successfully shown that an anatomical change can be detected, quantified and localized along all three spatial dimensions. This information, which could be obtained from one single low-dose helium-beam radiograph prior to each treatment fraction, could help to make ion-beam radiotherapy treatments more precise.

5.5 Further steps to align the detection system with clinical requirements

The aim of this PhD project was to develop the helium-beam imaging system based on thin silicon pixel detectors towards a future clinical use. In this thesis, I presented crucial methodological advancements and demonstrated the system's potential to serve as a low-dose imaging modality for pre-treatment verification of patient anatomy. However, some caveats remain before the system can be used in clinics.

Most importantly, the long imaging time needs to be addressed. Currently, the mono-energetic acquisition of a radiograph with the size of the detector's field of view takes around 5 minutes. The acquisition of an energy-painted radiograph with a larger size scales with the number of sub-regions and energies and can therefore take up to several hours (e.g., 2-3 h for the radiograph in fig. 4.7 with 35 acquisitions, see fig. 3.9).
The long imaging times are mainly due to the dead time of the first generation's Timepix detector. After each measured frame, the whole detector matrix is read out, which accounts for 97 % of the imaging duration (30 ms dead time per 1 ms active time). Thus, an upgrade to a newer and faster generation is inevitable before the system can be used in clinics.
Instead of a frame-based one, Timepix3 and 4 detectors (Poikela et al. 2014, Llopart et al. 2022) operate a data-driven readout. Here, only the hit pixels are read out while the vast majority of the pixels stay active. This improvement of the readout electronics practically removes the dead time causing an acceleration of the imaging process by a factor of at least 30.
An upgrade of the detection system towards higher detector generations is planned. With this new imaging system, imaging times on the order of minutes seem realistic even for large images of anthropomorphic phantoms.

Still, this upgraded setup could only be applied for static targets. In order to acquire images of moving tumor sites like the lung, the imaging times have to be further decreased towards the order of a second or even lower.
One effective measure to decrease the imaging times is to increase the intensity of the beam. With the new Timepix generations, particle intensities of around 100 kHz - 1 MHz are realistic (Knobloch et al. 2022), which must however be validated experimentally first. Furthermore, faster imaging could be achieved by using an overall lower number of primary helium ions, which would also decrease the dose to the patient. Future investigations should focus on finding a minimum imaging dose with still acceptable image characteristics.

Another limiting factor for the applicability in terms of body sites could result from available helium beam energies. The synchrotron at HIT was dimensioned and equipped with a magnetic rigidity for the acceleration of carbon ions with penetration depths of 30 mm in water. Therefore, apart from the therapeutic helium beams with up to 220.51 MeV/u, also helium beams with up to 430 MeV/u can be produced (Schömers et al. 2022). These highly energetic beams enable imaging of even the thickest body parts (e.g., pelvic region) (Knobloch et al. 2022). However, for other centers with more compact accelerators, the field geometries eligible for imaging might be limited to thinner projections of the body.

To obtain images with a larger size than the field of view of the Timepix detectors, currently, the phantoms must be moved laterally between the tracking units of the static detection system, which is no long-term solution. To ensure the patient's comfort, a movement of the detectors in synchronization with the scanning beam would be the preferred option. Alternatively, building large detector arrays from Timepix4 detectors, which are the first generation to be 4-side buttable (Llopart et al. 2022), is conceivable. However, these detector arrays would be rather expensive.

Another requirement for clinical use is a particle detection rate of at least 1 MHz (Schulte et al. 2004, Johnson 2024) to be able to operate the system at clinical intensities. Currently, we operate at around 10-100 kHz, which corresponds to an intensity far lower than the lowest clinically commissioned one and is only available for research purposes at HIT. In other centers, these rates are not achievable, which would prevent a widespread use of our detection system. As already mentioned, with a system based on Timepix3 or Timepix4 detectors, particle rates of 1 MHz could be within reach (Knobloch et al. 2022).

The availability of helium beams in general is also a factor which needs to be considered. Currently, only few centers worldwide operate a commissioned helium beam (Mairani et al. 2022). After pioneering helium treatments in the last century (Castro and Quivey 1977, Saunders et al. 1985), the first raster-scanned helium patient was just treated in 2021 (Tessonnier et al. 2023) and since then, there has been a growing interest in helium therapy (Mairani et al. 2022). Additionally, compact designs for helium accelerators are investigated (Jongen et al. 2010, Graeff et al. 2023), which could enable a more widespread use of helium beams for therapy.
If the lack of centers operating a helium beam should be a limiting factor for helium-beam radiography, the system as is could also be used for proton-beam radiography. The system had been shown to be functional for this ion type as well (Gehrke et al. 2018a).

The radiation hardness of Timepix detectors has been studied already in detail (Berke 2016). There, it was found that all pixels stayed functional after being irradiated with 330 Gy, which corresponds to the acquisition of around 10^6 radiographs (Gehrke 2018). To protect the imager from the high treatment doses, the imager could be mounted on robotic arms in the ceiling similar to the X-ray panels or cone-beam CTs. Since the ion beam is used for imaging and for the subsequent treatment, no uncertainties would arise from the robotic arm moving the detection system in and out. This contrasts other imaging modalities which need to be registered to the beam isocenter in some way. If the presented helium-beam imager is moved out of the beam during treatments, the accumulated imaging doses should not prevent a use of Timepix detectors in terms of functionality. However, the necessity of recalibrations for maintaining high WET accuracy should be investigated (Gehrke 2018).

6 Conclusion

This thesis demonstrated the potential of a lightweight and compact helium-beam radiography system for the detection, quantification and localization of anatomical changes in anthropomorphic phantoms.

Before the start of this PhD project, a prototype imaging system based on Timepix detectors of the first generation was available and proven to be functional. It yielded sufficient image characteristics in terms of CNR, spatial resolution and water-equivalent thickness (WET) resolution, but could be only used for imaging of simple phantoms. The objective of my PhD project was to enable the detection, quantification and localization of anatomical changes in clinically relevant phantoms with this helium-beam radiography system to advance it from initial proof-of-principle experiments towards the envisaged future clinical application.

After an introduction of a scatter filter technique and the establishment of calibration curves for multiple initial beam energies, the energy-painting method was experimentally assessed. This method is necessary to overcome the inherently limited WET range of the detection system that can be imaged with high precision. Utilizing several initial beam energies adjusted to the expected WET of the object, the methodology was thoroughly tested with a PMMA wedge phantom. Compared to the previous monoenergetic approach, an improvement of the mean precision by a factor of around 2.5 was found.

After the energy painting method had been shown to enable high-precision imaging of objects with large variations in WET, it was applied to image the skull-base region of an anthropomorphic head phantom. The water-equivalent thickness (WET) accuracy of the resulting helium-beam radiograph (αRad) was assessed utilizing a reference data set based on a segmented high-resolution X-ray CT scan and range-pullback measurements of all materials in the phantom. The found mean absolute percentage error of 1.16 % was then compared to the one reached by clinically used X-ray CT modalities and found to be competitive (DECT-DirectSPR 0.95 %, SECT-HLUT 1.05 %). For the purpose of pre-treatment verification of the patient's anatomy, helium-beam radiography thus emerges as a low-dose imaging modality (αRad: 290 µGy, DECT-DirectSPR: 23800 µGy and SECT-HLUT: 24900 µGy) with sufficient WET accuracy on the 1 % level.

To enable the localization of anatomical changes even along the direction of projection, the so-called 2.5D imaging approach was tested in simulations with a proton and helium beam. Since they provided a similar depth-detection accuracy, an experimental study based on helium-beam radiographs, which generally provide superior spatial resolution compared to proton images, followed. Along the beam direction, a localization accuracy of around 1 cm was reached in experiments with a slab phantom, which fulfills the foreseen requirements for clinical use. Spatial resolution values between 0.8 lp/mm and 2 lp/mm were obtained within the image plane depending on the depth of a feature.

Finally, the 2.5D methodology was tested for a realistic anatomical change in a head phantom applying a clinically acceptable dose of around 300 µGy. Apart from the accurate quantification and lateral localization of the change in the nasopharyngeal cavity, its position along the beam axis could be determined with an accuracy of 13 mm. This accuracy allows for an assessment of whether an anatomical change happened within the planned field of the subsequent treatment fraction or at greater depths, with only the former having consequences on treatment accuracy.

With the successful conclusion of this study, the aim of the thesis to enable detection, quantification and localization of anatomical changes was realized. Excellent accuracy and precision were reached in the investigated cases demonstrating the system's potential for daily verification of the patient's anatomy prior to ion-beam radiotherapy treatments.

7 Outlook

This thesis demonstrated how the compact helium-beam radiography system based on thin silicon pixel detectors could be applied for pre-treatment verification of the patient's anatomy. At imaging doses below 300 µGy, a WET accuracy and spatial resolution sufficient for clinical application were reached. While an anatomical change in an anthropomorphic phantom could be detected, quantified and localized in 3D, the system in its current state cannot yet be used for that purpose in clinics due to technical limitations (see section 5.5). Therefore, besides testing the shown methodology for a variety of phantom body sites and anatomical changes, it is now of major importance to mitigate the factors inhibiting the system from being used in clinics.

First and foremost, operation at higher beam intensities and shorter imaging times must be achieved in order to meet the clinical requirements. Furthermore, either large detector arrays must be built or the detection system has to be moved synchronously with the scanning beam to be able to keep the patient static for high imaging speeds.

Currently, a master's student in our group, Dierk Schulz, is working on building a new system based on Timepix3 detectors. This new system offers several improvements over the previous one.
Most importantly, the detection system will shorten the measurement times towards the order of minutes. This drastic improvement is due to the novel data-driven readout protocol which mitigates the current dead time of around 30 ms per 1 ms active time completely. The system will be tested with particle rates of 100 kHz to 1 MHz and will be mounted on a moving stage in order to move together with the beam and enable a static positioning of the phantom.
Moreover, the Timepix3 detectors can provide time and energy deposition information simultaneously. Therefore, also on the tracking detectors, energy deposition is available. This information could be incorporated into a more robust WET determination and will reduce the uncertainties of the impact positions of each single ion, since an energy-weighting of the center of mass can be implemented.

The methodological advancements presented in this thesis were developed for list-mode detection systems employing energy deposition measurements by thin detectors and are

readily applicable to the upgraded system as well.
Recently, the system based on Timepix3 detectors has been successfully used for first calibration measurements. Following measurement campaigns will focus on the reproduction of the WET accuracy, spatial resolution and depth detection accuracy presented in this thesis at significantly reduced measurement times ($\approx$ factor 30). If the new detection system is shown to meet the requirements for clinical operation, the helium-beam imaging system based on thin pixelated detectors could be applied in a clinical study.

Besides the envisaged clinical application for monitoring of the patient anatomy right before the treatment start, there are other interesting use cases for our helium-beam imaging system. Among these are, e.g., mixed helium-carbon beams for simultaneous treatment and imaging (Graeff et al. 2018, Mazzucconi et al. 2018, Volz et al. 2020b, Hardt et al. 2024), imaging of patients with metal implants (Civinini et al. 2020) or patient-specific CT calibrations obtained from ion-beam radiographs (Schneider et al. 2005, Doolan et al. 2015, Collins-Fekete et al. 2017a, Gianoli et al. 2020).

Regardless of the specific use case, ion-beam radiography has strong potential to serve as an imaging modality for ion-beam radiotherapy treatments. After the remaining technical aspects are addressed, the detection system represents a promising candidate for future clinical implementation given the advantages of its compact design and the achieved image characteristics for anthropomorphic objects.

A Appendix

A.1 Effect of adjusted spatial resolution on comparison with reference

To investigate the effect of spatial resolution on the differences between reference and the three imaging modalities under investigation (helium-beam radiography (αRad), dual-energy computed tomography (DECT-DirectSPR), single-energy computed tomography (SECT-HLUT)), some results of section 4.3 are repeated here with an artificially worsened spatial resolution of the reference image. The reference is blurred with a Gaussian kernel (σ of 0.7 mm, corresponding to the approximate spatial resolution of the three imaging modalities). In fig. A.1, the WET-maps, the gamma analysis and the relative difference images are shown analogously to fig. 4.7 with the blurred reference. The metrics summarizing the WET deviations from the references with different spatial resolution are presented in table A.1.

Table A.1: Metrics to compare water-equivalent thickness (WET) accuracy for reference and blurred reference. The gamma index, mean absolute percentage error (MAPE) and root-mean-square percentage error (RMSPE) are calculated for the images based on helium-beam radiography (αRad), dual-energy computed tomography (DECT-DirectSPR) and single-energy computed tomography (SECT-HLUT) relative to the reference with and without blurring.

Metric	αRad	DECT-DirectSPR	SECT-HLUT
Reference			
γ index (%)	73.9 ± 0.9	78.7 ± 0.7	74.1 ± 0.8
MAPE (%)	1.16 ± 0.05	0.95 ± 0.05	1.05 ± 0.06
RMSPE (%)	1.46 ± 0.06	1.19 ± 0.05	1.30 ± 0.06
Blurred Reference			
γ index (%)	83.9 ± 0.6	92.8 ± 0.4	87.2 ± 0.5
MAPE (%)	0.98 ± 0.05	0.74 ± 0.05	0.87 ± 0.05
RMSPE (%)	1.22 ± 0.06	0.91 ± 0.05	1.05 ± 0.06

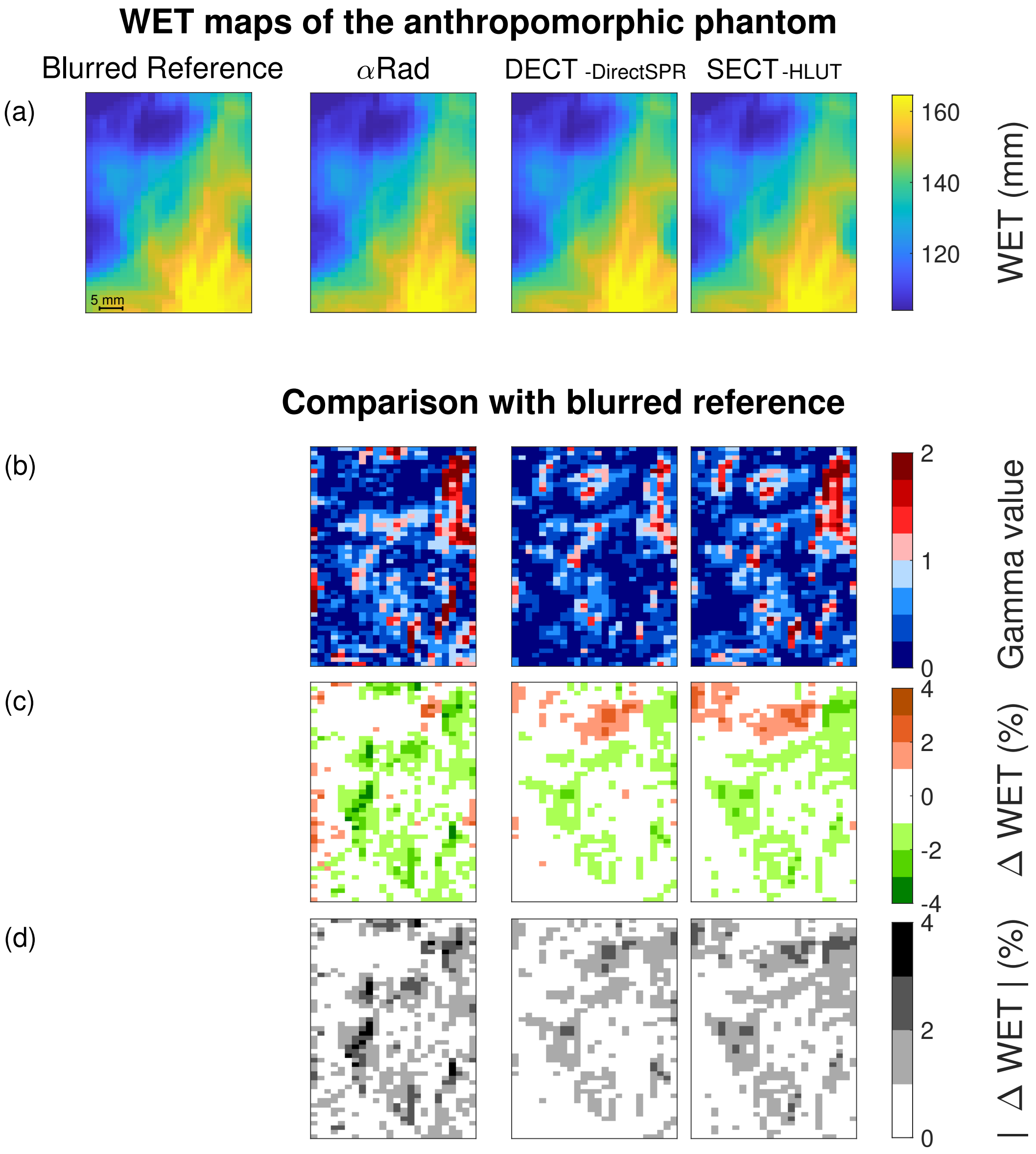

Figure A.1: WET-maps and comparison with blurred reference (c.f. fig. 4.7) (a) WET-maps of skull base region of the anthropomorphic phantom determined with different imaging modalities: reference blurred with σ of 0.7 mm, helium-beam radiograph (αRad), and projections based on dual-energy computed tomography (DECT-DirectSPR), and single-energy computed tomography (SECT-HLUT) scans. (b) Gamma analysis between imaging modalities and reference with the criteria 1 mm and 0.7 %. (c,d) Relative and absolute percentage difference between imaging modalities and blurred reference.

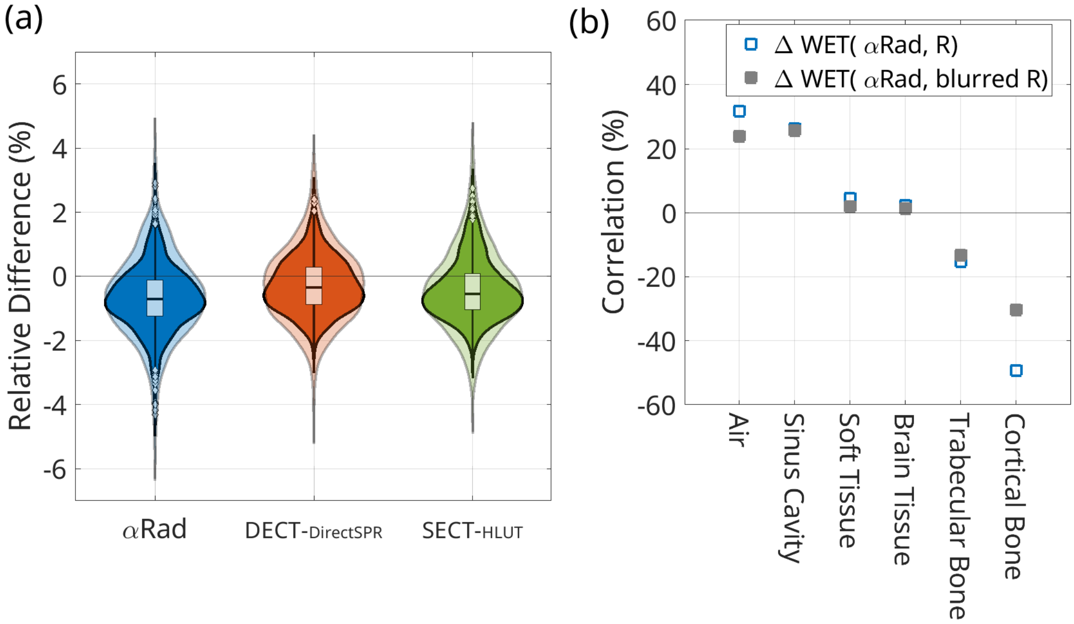

Figure A.2: Effect of spatial resolution of reference on quantitative comparison. The analysis of fig. 4.8(b) and fig. 4.11(b) was repeated, however with a reference scan which was blurred with a Gaussian ($\sigma = 0.7\,\text{mm}$) to assimilate the spatial resolution to the one of the other images. In (a), the violin plots show the distribution of relative WET deviations in fig. A.1(c). The outlines in the background show the distributions obtained with the non-blurred reference. In (b), the correlation between abundance of a material in a pixel channel and WET deviations of αRad are plotted for both blurred and non-blurred reference (R).

Figure A.2 repeats the violin plot (fig. 4.8(b)) for the blurred reference. Here, the relative WET deviations of the images in fig. A.1(c) are shown as distributions. In the background, the outline of the violin plots of the sharp reference of fig. 4.8(b) is repeated.

In fig. A.2(b), the correlation between material occurrence in the pixel channel and WET deviations is shown both for the blurred reference and the original reference without blurring. For the sake of clarity only the values of αRad are presented here.

From fig. A.1, fig. A.2 and especially table A.1, it can be concluded that the extent of deviations is reduced if the spatial resolution of the reference is artificially decreased to approximately match the one of the three other imaging modalities. For a discussion, please refer to section 5.3.

A.2 Comparison of kernels for 2.5D imaging

This section is based on Metzner et al. (2025b).

The Laplacian which Volz et al. (2024) used for the determination of image sharpness is prone to noise as also pointed out by the authors themselves. Therefore, Volz et al. (2024) used a Gaussian smoothing kernel before applying the Laplacian.
Guided by theoretical reasoning, we exchanged both kernels by alternative ones as also listed in table A.2. First, we selected a median filter (Tukey 1977) for smoothing of the image instead of the Gaussian one. This choice was reasoned by the edge-preservation ability of the median filter[1] which is important for the 2.5D imaging approach.
The Laplacian's sensitivity to noise is mainly based on the twofold differentiation. Therefore, we replaced it by the Tenengrad score[2], which is based on the Sobel operator (Danielsson and Seger 1990) and thus the first derivative.

In fig. A.3, I applied the two sets of kernels to the data set acquired with the air gap phantom and compared their performance regarding their depth detection capabilities. In order to facilitate a fair comparison, I optimized the kernel sizes separately in terms of accuracy and precision. The kernel sizes which delivered the best results are listed in table A.2 and the respective curves are shown in fig. A.3(a). The upper panel displays the result obtained with the Gaussian and Laplacian, the lower panel repeats the results shown in the main body (fig. 4.19) which were obtained with the median and Tenengrad. The dots represent the respective scores determined for the image reconstructed in this depth. The solid line represents the smoothed data with the envelope marking the uncertainties. The depth of the maximum spatial resolution is marked by star symbols (Laplacian) and diamonds (Tenengrad), respectively. In fig. A.3(b) the accuracy of both sets of kernels is displayed. The error bars of the accuracy denote the precision. Here, it can be seen that the overall precision is improved due to the use of the median and Tenengrad. The mean precision over all gap positions could be enhanced by around 44 % due to the use of this alternative set of kernels as it can be seen in table A.2.

---

[1] The idea for the median filter stemmed from Patrice Schlegel, personal communication, 26.02.2025

[2] Also the idea of using the Tenengrad stemmed from Patrice Schlegel, personal communication with Annika Schlechter, 05.04.2023

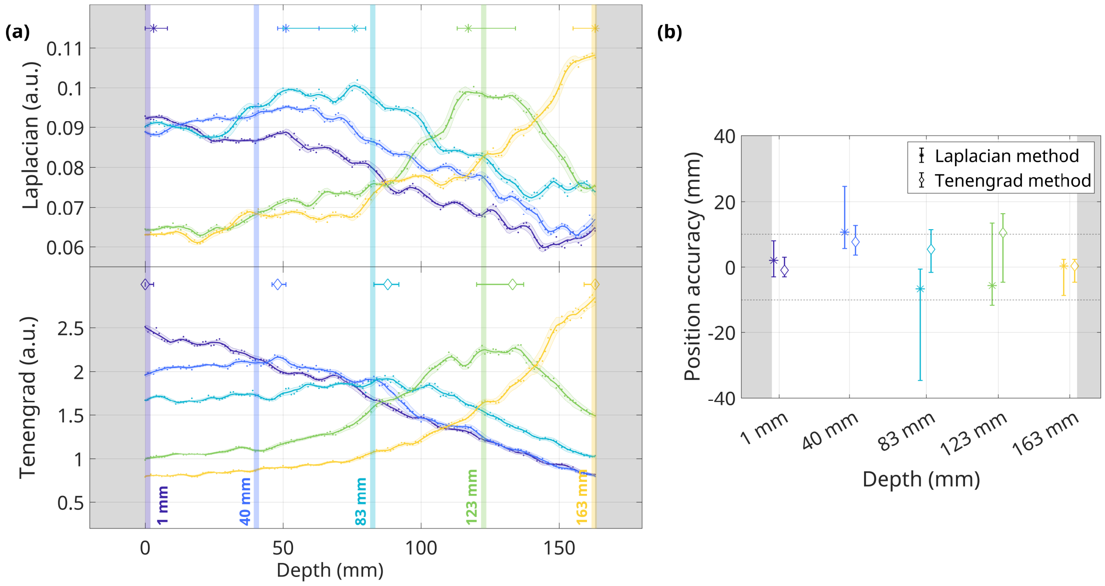

Figure A.3: 2.5D imaging methodology used in this thesis compared to the one of Volz et al. (2024). Both sets of kernels (c.f. table A.2) are applied to the data set with the different air gap positions within the PMMA phantom (a) Laplacian (upper panel) versus Tenengrad (lower panel) for gradient determination, which were smoothed beforehand with a Gaussian and median filter, respectively. (b) Accuracy for both sets of kernels, where error bars denote precision. Reprinted from Metzner et al. (2025b), CC BY 4.0.

Table A.2: 2.5D imaging methodology used in this thesis compared to the one of Volz et al. (2024). Adapted from Metzner et al. (2025b), CC BY 4.0. Two tables were merged into one.

	Volz et al. (2024)	**This thesis**
Kernels		
Noise reduction	Gaussian (3 px × 3 px)	Median (7 px × 7 px)
Gradient determination	Laplacian (7 px × 7 px)	Sobel (3 px × 3 px)
Metrics for data in fig. A.3		
Mean absolute error	5.1 mm	5.0 mm
Mean precision	20.0 mm	11.2 mm

B List of Abbreviations

APR	along-path reconstruction	39
αRad	helium-beam radiography	34
αRad	helium-beam radiograph	53
ASIC	application-specific integrated circuit	31
CERN	European Organization for Nuclear Research	31
CNR	contrast-to-noise ratio	28
CSDA	continuous slowing down approach	13
CT	computed tomography	5
CTN	CT numbers	22
DECT	dual-energy computed tomography	23
DECT-DirectSPR	dual-energy computed tomography	51
FWHM	full width at half maximum	31
FOV	field of view	51
FPGA	field-programmable gate array	33
HIT	Heidelberg Ion-beam Therapy center	29
HLUT	Hounsfield look-up table	23
iCT	ion-beam CT	25
iRad	ion-beam radiograph	26
MAPE	mean absolute percentage error	54
MCS	multiple Coulomb scattering	15
MIP	minimum ionizing particle	11
MLP	most likely path	38
MTF	modulation transfer function	59
OSESF	oversampled edge spread function	59
PET	positron emission tomography	24
PIB	plane-of-interest binning	39
PMMA	polymethyl methacrylate	44
RMSD	root-mean-square deviation	70
RMSPE	root-mean-square percentage error	54
ROI	region of interest	40

RSP	relative stopping power	14
SECT	single-energy computed tomography	23
SECT-HLUT	single-energy computed tomography	51
SIWP	single-ion WET precision	45
SOBP	spread-out Bragg peak	20
SR	spatial resolution	28
ToA	Time of Arrival	32
TOF	time of flight	27
ToT	Time over Threshold	32
WET	water-equivalent thickness	2

C List of Figures

D List of Tables

E Statement on the use of AI-based aids

Following the "Stellungnahme des Präsidiums der Deutschen Forschungsgemeinschaft (DFG) zum Einfluss generativer Modelle für die Text- und Bilderstellung auf die Wissenschaften und das Förderhandeln der DFG"[1] (September 2023), I hereby report to have utilized ChatGPT and DeepL to search for synonyms, rephrase single sentences and fix grammar or punctuation mistakes during the writing process of my thesis. I want to further declare, that I reviewed the output of these AI-based aids and that I am solely responsible for the content of my thesis.

---

[1] `https://www.dfg.de/resource/blob/289674/230921-stellungnahme-praesidium-ki-ai.pdf`, Accessed: 28.08.2025

F List of publications

Publications in peer-reviewed journals

Published during my PhD project:

- **M. Metzner**, D. Zhevachevska, A. Schlechter, F. Kehrein, J. Schlecker, C. Murillo, S. Brons, O. Jäkel, M. Martišíková, and T. Gehrke.
  "Energy painting: helium-beam radiography with thin detectors and multiple beam energies".
  Physics in Medicine & Biology, 69(5):055002, 2024.
  `https://doi.org/10.1088/1361-6560/ad247e`
- **M. Metzner**, F. K. Longarino, B. Ackermann, A. Schlechter, M. Saphörster, Y. Xu, J. Schlecker, P. Wohlfahrt, C. Richter, S. Brons, J. Debus, O. Jäkel, M. Martišíková, and T. Gehrke.
  "Accuracy of a helium-beam radiography system based on thin pixel detectors for an anthropomorphic head phantom".
  Medical physics, 52(6):4757-4768, 2025.
  `https://doi.org/10.1002/mp.17786`
- **M. Metzner**, A. Schlechter, D. Zhevachevska, P. Schlegel, O. Jäkel, M. Martišíková, and T. Gehrke.
  "2.5D Imaging: Obtaining depth information from 2D helium-beam radiographs".
  Physics in Medicine & Biology. Accepted for publication: 3rd of September 2025, Advance online publication.
  `https://doi.org/10.1088/1361-6560/ae02de`

All three listed publications have been used in this thesis. For more details please refer to section 1.4. Furthermore, the respective sections contain a note if they were based on one of these publications.

Published during my Master's thesis project:

- C. Knobloch, **M. Metzner**, F. Kehrein, C. Schömers, S. Scheloske, S. Brons, R. Hermann, A. Peters, O. Jäkel, M. Martišíková, and T. Gehrke.
  "Experimental helium-beam radiography with a high-energy beam: Water-equivalent thickness calibration and first image-quality results".
  Medical Physics 49(8):5347-5362, 2022.
  `https://doi.org/10.1002/mp.15795`

This publication is only cited in this thesis.

Conference Contributions

As presenting author:

- Y. Xu, **M. Metzner**, D. Zhevachevska, A. Schlechter, S. Schaumann, R. Floca, B. Ackermann, O. Jäkel, M. Martišíková, and T. Gehrke. Investigating the feasibility of patient positioning based on a helium-beam radiograph acquired with thin silicon pixel detectors. 61st Annual Conference of the Particle Therapy Co-Operative Group (PTCOG), Madrid, Spain, 2023, **Oral presentation**.

- **M. Metzner**, F. Kehrein, C. Knobloch, M. Raza, B. Ackermann, S. Brons, M. Matouš, O. Jäkel, M. Martišíková and T. Gehrke. Quantitative helium-beam radiograph of a head and neck model and comparison to X-ray CT projections. 24th International Workshop on Radiation Imaging Detectors (iWoRiD), Oslo, Norway, 2023, **Oral presentation**.

- **M. Metzner**, D. Zhevachevska, A. Schlechter, F. Kehrein, J. Schlecker, C. Murillo, S. Brons, O. Jäkel, M. Martišíková and T. Gehrke. Energy painting with several initial beam energies and thin silicon pixel detectors for imaging of objects with wide WET ranges. 4th Ion Imaging Workshop, London, UK, 2023, **Oral presentation**.

- **M. Metzner**, F. K. Longarino, B. Ackermann, A. Schlechter, M. Saphörster, J. Schlecker, P. Wohlfahrt, C. Richter, S. Brons, O. Jäkel, M. Martišíková and T. Gehrke. Water-equivalent thickness accuracy of a helium-beam radiograph showing an anthropomorphic head phantom in comparison to projections of a reference data set and X-ray CT modalities. 5th Ion Imaging Workshop, Vienna, Austria, 2024, **Oral presentation**.

- **M. Metzner**, A. Schlechter, C. Amato, O. Jäkel, M. Martišíková and T. Gehrke. Helium-beam radiography for precise cancer irradiation: Impact of scatter rejection on image quality. IEEE Nuclear Science Symposium and Medical Imaging Conference, Tampa, USA, 2024, **Oral presentation**.

- **M. Metzner**, A. Schlechter, D. Zhevachevska, P. Schlegel, O. Jäkel, M. Martišíková, and T. Gehrke. 3D-Lokalisierung von anatomischen Veränderungen anhand von 2D Heliumstrahlradiografien. 56. Jahrestagung der Deutschen Gesellschaft für Medizinische Physik, Berlin, Germany, 2025, **Poster presentation**.

In addition, I contributed to 6 oral and 1 poster presentation as co-author.

Contributions to other scientific events

- **M. Metzner**, F. Kehrein, C. Knobloch, G. Echner, A. Runz, B. Ackermann, S. Brons, O. Jäkel, M. Martišíková and Tim Gehrke. Ions instead of X-rays? - Imaging with Helium-ion beams. 5th scientific Retreat of the National Center for Radiation Oncology (NCRO), Heidelberg, Germany, 2023, **Oral presentation**.
- **M. Metzner**, F. K. Longarino, B. Ackermann, D. Zhevachevska, A. Schlechter, M. Saphörster, F. Kehrein, J. Schlecker, C. Murillo, S. Brons, J. Debus, P. Wohlfahrt, C. Richter, O. Jäkel, M. Martišíková and T. Gehrke. Ion imaging of humanlike phantoms with multiple initial beam energies and thin silicon pixel detectors, 2nd HGSFP Summer School, Molveno, Italy, 2024, **Poster presentation**.
- **M. Metzner**, F. K. Longarino, B. Ackermann, D. Zhevachevska, A. Schlechter, M. Saphörster, F. Kehrein, J. Schlecker, C. Murillo, S. Brons, J. Debus, P. Wohlfahrt, C. Richter, O. Jäkel, M. Martišíková and T. Gehrke. Helium-beam radiography of an anthropomorphic head phantom using thin silicon pixel detectors and multiple beam energies. 2024 German Cancer Research Center (DKFZ) PhD Poster Presentation, Heidelberg, Germany, 2024, **Poster presentation**.
- **M. Metzner**, O. Jäkel, M. Martišíková and T. Gehrke. Helium ion beam imaging with Timepix1 detectors for cancer treatment with ion beams. Medipix Meeting, CERN, Geneva, Switzerland, 2024, **Oral presentation**.

G Bibliography

F. Albertini, M. Casiraghi, S. Lorentini, B. Rombi, and A. J. Lomax. Experimental verification of IMPT treatment plans in an anthropomorphic phantom in the presence of delivery uncertainties. *Physics in Medicine & Biology*, 56(14):4415, 2011. doi:10.1088/0031-9155/56/14/012. (Cited on page 50)

C. Amato, M. Martišíková, and T. Gehrke. A technique for spatial resolution improvement in helium-beam radiography. *Medical physics*, 47(5):2212–2221, 2020. doi:10.1002/mp.14051. (Cited on pages 3, 34, 35, 36, 38, 40, 57, 111, 113, and 115)

N. Arbor, D. Dauvergne, G. Dedes, J. M. Létang, K. Parodi, C. Quiñones, E. Testa, and S. Rit. Monte Carlo comparison of x-ray and proton CT for range calculations of proton therapy beams. *Physics in Medicine & Biology*, 60(19):7585, 2015. doi:10.1088/0031-9155/60/19/7585. (Cited on pages 2 and 26)

G. Aricò, T. Gehrke, J. Jakůbek, R. Gallas, S. Berke, O. Jäkel, A. Mairani, A. Ferrari, and M. Martišíková. Investigation of mixed ion fields in the forward direction for 220.5 MeV/u helium ion beams: comparison between water and PMMA targets. *Physics in Medicine & Biology*, 62(20):8003, 2017. doi:10.1088/1361-6560/aa875e. (Cited on page 38)

F. Ballarini, K. Batkov, G. Battistoni, M. G. Bisogni, T. T. Böhlen, M. Campanella, M. P. Carante, D. Chen, A. De Gregorio, P. V. Degtiarenko, et al. The FLUKA code: Overview and new developments. *EPJ Nuclear Sciences & Technologies*, 10:16, 2024. doi:10.1051/epjn/2024015. (Cited on page 57)

E. Bär, A. Lalonde, G. Royle, H.-M. Lu, and H. Bouchard. The potential of dual-energy CT to reduce proton beam range uncertainties. *Medical physics*, 44(6):2332–2344, 2017. doi:10.1002/mp.12215. (Cited on page 109)

E. Bär, A. Lalonde, R. Zhang, K.-W. Jee, K. Yang, G. Sharp, B. Liu, G. Royle, H. Bouchard, and H.-M. Lu. Experimental validation of two dual-energy CT methods for proton therapy using heterogeneous tissue samples. *Medical physics*, 45(1):48–59, 2018. doi:10.1002/mp.12666. (Cited on page 109)

E. Bär, L. Volz, C.-A. Collins-Fekete, S. Brons, A. Runz, R. W. Schulte, and J. Seco. Experimental comparison of photon versus particle computed tomography to predict tissue relative stopping powers. *Medical Physics*, 49(1):474–487, 2022. doi:10.1002/mp.15283. (Cited on pages 25 and 102)

J. L. Barker Jr, A. S. Garden, K. K. Ang, J. C. O'Daniel, H. Wang, L. E. Court, W. H. Morrison, D. I. Rosenthal, K. C. Chao, S. L. Tucker, et al. Quantification of volumetric and geometric changes occurring during fractionated radiotherapy for head-and-neck cancer using an integrated CT/linear accelerator system. *International Journal of Radiation Oncology* Biology* Physics*, 59(4):960–970, 2004. doi:10.1016/j.ijrobp.2003.12.024. (Cited on page 117)

V. Bashkirov, R. W. Schulte, R. Hurley, R. Johnson, H.-W. Sadrozinski, A. Zatserklyaniy, T. Plautz, and V. Giacometti. Novel scintillation detector design and performance for proton radiography and computed tomography. *Medical physics*, 43(2):664–674, 2016. doi:10.1118/1.4939255. (Cited on pages 70, 103, 104, and 134)

G. Battistoni, F. Cerutti, A. Fasso, A. Ferrari, S. Muraro, J. Ranft, S. Roesler, and P. Sala. The FLUKA code: Description and benchmarking. In *AIP Conference proceedings*, volume 896, pages 31–49. American Institute of Physics, 2007. doi:10.1063/1.2720455. (Cited on page 57)

G. Battistoni, J. Bauer, T. T. Boehlen, F. Cerutti, M. P. Chin, R. Dos Santos Augusto, A. Ferrari, P. G. Ortega, W. Kozłowska, G. Magro, et al. The FLUKA code: an accurate simulation tool for particle therapy. *Frontiers in oncology*, 6:116, 2016. doi:10.3389/fonc.2016.00116. (Cited on page 57)

M. J. Berger. Monte Carlo calculation of the penetration and diffusion of fast charged particles. *Methods in Computational Physics*, 135, 1963. (Cited on page 17)

M. J. Berger, J. S. Coursey, M. A. Zucker, and J. Chang. ESTAR, PSTAR, and ASTAR: computer programs for calculating stopping-power and range tables for electrons, protons, and helium ions (version 2.0.1). 2017. doi:10.18434/T4NC7P. Accessed: 2022-08-11. (Cited on page 10)

S. Berke. Investigation of the detector response of Timepix detector in therapeutic ion beam. Master's thesis, Heidelberg University, 2016. (Cited on page 119)

H. Bethe. Zur Theorie des Durchgangs schneller Korpuskularstrahlen durch Materie. *Annalen der Physik*, 397(3):325–400, 1930. doi:10.1002/andp.19303970303. (Cited on page 10)

H. Bichsel. Passage of charged particles through matter. 1969. doi:10.2172/6675902. (Cited on page 23)

T. Böhlen, F. Cerutti, M. Chin, A. Fassò, A. Ferrari, P. G. Ortega, A. Mairani, P. R. Sala, G. Smirnov, and V. Vlachoudis. The FLUKA code: developments and challenges for high energy and medical applications. *Nuclear data sheets*, 120:211–214, 2014. doi:10.1016/j.nds.2014.07.049. (Cited on page 57)

C. Bopp, R. Rescigno, M. Rousseau, and D. Brasse. The impact of tracking system properties on the most likely path estimation in proton ct. *Physics in Medicine & Biology*, 59(23):N197, 2014. doi:10.1088/0031-9155/59/23/N197. (Cited on page 114)

T. Bortfeld. An analytical approximation of the Bragg curve for therapeutic proton beams. *Medical physics*, 24(12):2024–2033, 1997. doi:10.1118/1.598116. (Cited on pages 13, 44, 45, and 70)

H. Bradt and B. Peters. The heavy nuclei of the primary cosmic radiation. *Physical Review*, 77(1):54, 1950. doi:10.1103/PhysRev.77.54. (Cited on page 16)

W. Bragg. Lxxiii. on the absorption of α rays, and on the classification of the α rays from radium. *The London, Edinburgh, and Dublin Philosophical Magazine and Journal of Science*, 8(48):719–725, 1904. doi:10.1080/14786440409463245. (Cited on page 13)

W. H. Bragg and R. Kleeman. Xxxix. on the α particles of radium, and their loss of range in passing through various atoms and molecules. *The London, Edinburgh, and Dublin Philosophical Magazine and Journal of Science*, 10(57):318–340, 1905. doi:10.1080/14786440509463378. (Cited on pages 1 and 13)

C. Bussolati, A. Fiorentini, and G. Fabri. Energy for electron-hole pair generation in silicon by electrons and α particles. *Physical Review*, 136(6A):A1756, 1964. doi:10.1103/PhysRev.136.A1756. (Cited on page 18)

J. R. Castro. Results of heavy ion radiotherapy. *Lawrence Berkeley National Laboratory*, LBNL Report #: LBL-35723, 1994. URL `https://escholarship.org/uc/item/9md1x98x`. (Cited on page 1)

J. R. Castro and J. M. Quivey. Clinical experience and expectations with helium and heavy ion irradiation. *International Journal of Radiation Oncology* Biology* Physics*, 3:127–131, 1977. doi:10.1016/0360-3016(77)90238-3. (Cited on page 119)

C. Civinini, M. Scaringella, M. Brianzi, M. Intravaia, N. Randazzo, V. Sipala, M. Rovituso, F. Tommasino, M. Schwarz, and M. Bruzzi. Relative stopping power measurements and prosthesis artifacts reduction in proton CT. *Physics in Medicine & Biology*, 65(22):225012, 2020. doi:10.1088/1361-6560/abb0c8. (Cited on pages 26 and 124)

C.-A. Collins-Fekete, P. Doolan, M. F. Dias, L. Beaulieu, and J. Seco. Developing a phenomenological model of the proton trajectory within a heterogeneous medium required for proton imaging. *Physics in Medicine & Biology*, 60(13):5071, 2015. doi:10.1088/0031-9155/60/13/5071. (Cited on pages 38 and 39)

C.-A. Collins-Fekete, S. Brousmiche, S. K. Portillo, L. Beaulieu, and J. Seco. A maximum likelihood method for high resolution proton radiography/proton CT. *Physics in Medicine & Biology*, 61(23):8232, 2016. doi:10.1088/0031-9155/61/23/8232. (Cited on pages 39 and 93)

C.-A. Collins-Fekete, S. Brousmiche, D. C. Hansen, L. Beaulieu, and J. Seco. Pretreatment patient-specific stopping power by combining list-mode proton radiography and x-ray CT. *Physics in Medicine & Biology*, 62(17):6836, 2017a. doi:10.1088/1361-6560/aa7c42. (Cited on pages 26 and 124)

C.-A. Collins-Fekete, L. Volz, S. K. Portillo, L. Beaulieu, and J. Seco. A theoretical framework to predict the most likely ion path in particle imaging. *Physics in Medicine & Biology*, 62(5):1777, 2017b. doi:10.1088/1361-6560/aa58ce. (Cited on page 38)

Computerized Imaging Reference Systems, Inc. Proton Therapy Dosimetry Head, Model 731-HN. `http://www.cirsinc.com/wp-content/uploads/2020/12/731-HN-UG-072220.pdf`. Accessed: 2022-04-07. (Cited on page 50)

P.-E. Danielsson and O. Seger. Generalized and separable sobel operators. *Machine Vision for Three-Dimensional Scenes*, pages 347–379, 1990. doi:10.1016/B978-0-12-266722-0.50016-6. (Cited on pages 62, 91, and 128)

G. Dedes and K. Parodi. Monte Carlo simulations of particle interactions with tissue in carbon ion therapy. *International Journal of Particle Therapy*, 2(3):447–458, 2015. doi:10.14338/IJPT-15-00021. (Cited on page 17)

S. Deffet, M. Cohilis, K. Souris, K. Salvo, T. Depuydt, E. Sterpin, and B. Macq. openPR—a computational tool for CT conversion assessment with proton radiography. *Medical Physics*, 48(1):387–396, 2021. doi:10.1002/mp.14571. (Cited on page 26)

E. A. DeJongh, D. F. DeJongh, I. Polnyi, V. Rykalin, C. Sarosiek, G. Coutrakon, K. L. Duffin, N. T. Karonis, C. E. Ordoñez, M. Pankuch, et al. A fast and monolithic prototype clinical proton radiography system optimized for pencil beam scanning. *Medical physics*, 48(3):1356–1364, 2021. doi:10.1002/mp.14700. (Cited on pages 3, 27, 43, 101, and 115)

G. Delaney, S. Jacob, C. Featherstone, and M. Barton. The role of radiotherapy in cancer treatment: estimating optimal utilization from a review of evidence-based clinical guidelines. *Cancer: Interdisciplinary International Journal of the American Cancer Society*, 104(6):1129–1137, 2005. doi:10.1002/cncr.21324. (Cited on page 1)

N. Depauw and J. Seco. Sensitivity study of proton radiography and comparison with kV and MV x-ray imaging using GEANT4 Monte Carlo simulations. *Physics in Medicine & Biology*, 56(8):2407, 2011. doi:10.1088/0031-9155/56/8/006. (Cited on pages 2 and 26)

J. Dickmann, P. Wesp, M. Rädler, S. Rit, M. Pankuch, R. Johnson, V. Bashkirov, R. Schulte, K. Parodi, G. Landry, et al. Prediction of image noise contributions in proton computed tomography and comparison to measurements. *Physics in Medicine & Biology*, 64(14):145016, 2019. doi:10.1088/1361-6560/ab2474. (Cited on pages 70, 103, 104, and 134)

J. Dickmann, C. Sarosiek, S. Götz, M. Pankuch, G. Coutrakon, R. P. Johnson, R. W. Schulte, K. Parodi, G. Landry, and G. Dedes. An empirical artifact correction for proton computed tomography. *Physica Medica*, 86:57–65, 2021a. doi:10.1016/j.ejmp.2021.05.018. (Cited on page 102)

J. Dickmann, C. Sarosiek, V. Rykalin, M. Pankuch, G. Coutrakon, R. P. Johnson, V. Bashkirov, R. W. Schulte, K. Parodi, G. Landry, et al. Proof of concept image artifact reduction by energy-modulated proton computed tomography (empct). *Physica Medica*, 81:237–244, 2021b. doi:10.1016/j.ejmp.2020.12.012. (Cited on pages 43 and 101)

H. J. Dobbs, R. Parker, N. Hodson, P. Hobday, and J. E. Husband. The use of CT in radiotherapy treatment planning. *Radiotherapy and oncology*, 1(2):133–141, 1983. doi:10.1016/S0167-8140(83)80016-4. (Cited on page 2)

P. Doolan, M. Testa, G. Sharp, E. Bentefour, G. Royle, and H. Lu. Patient-specific stopping power calibration for proton therapy planning based on single-detector proton radiography. *Physics in Medicine & Biology*, 60(5):1901, 2015. doi:10.1088/0031-9155/60/5/1901. (Cited on pages 26 and 124)

M. Durante and J. Debus. Heavy charged particles: does improved precision and higher biological effectiveness translate to better outcome in patients? In *Seminars in radiation oncology*, pages 160–167. Elsevier, 2018. doi:10.1016/j.semradonc.2017.11.004. (Cited on pages 1 and 20)

M. Durante and H. Paganetti. Nuclear physics in particle therapy: a review. *Reports on Progress in Physics*, 79(9):096702, 2016. doi:10.1088/0034-4885/79/9/096702. (Cited on page 15)

M. Durante, A. Golubev, W.-Y. Park, and C. Trautmann. Applied nuclear physics at the new high-energy particle accelerator facilities. *Physics Reports*, 800:1–37, 2019. doi:10.1016/j.physrep.2019.01.004. Licensed under CC BY-NC-ND 4.0. (Cited on pages 20 and 132)

M. Durante, J. Debus, and J. S. Loeffler. Physics and biomedical challenges of cancer therapy with accelerated heavy ions. *Nature Reviews Physics*, 3(12):777–790, 2021. doi:10.1038/s42254-021-00368-5. (Cited on page 21)

A. Ferrari, J. Ranft, P. R. Sala, and A. Fassò. *FLUKA: A multi-particle transport code (Program version 2005)*. Number CERN-2005-10. Cern, 2005. doi:10.5170/CERN-2005-010. (Cited on page 57)

G. H. Fletcher. Regaud lecture perspectives on the history of radiotherapy. *Radiotherapy and Oncology*, 12(4):253–271, 1988. doi:10.1016/0167-8140(88)90015-1. (Cited on page 20)

R. Floca. Matchpoint: on bridging the innovation gap between algorithmic research and clinical use in image registration. In *World Congress on Medical Physics and Biomedical Engineering, September 7-12, 2009, Munich, Germany: Vol. 25/4 Image Processing, Biosignal Processing, Modelling and Simulation, Biomechanics*, pages 1105–1108. Springer, 2009. doi:10.1007/978-3-642-03882-2_294. (Cited on pages 53 and 61)

E. Fogazzi, M. Bruzzi, E. D'Amato, P. Farace, R. Righetto, M. Scaringella, M. Scarpa, F. Tommasino, and C. Civinini. Proton CT on biological phantoms for x-ray CT calibration in proton treatment planning. *Physics in Medicine & Biology*, 69(13): 135009, 2024. doi:10.1088/1361-6560/ad56f5. (Cited on page 26)

P. Freislederer, M. Kügele, M. Öllers, A. Swinnen, T.-O. Sauer, C. Bert, D. Giantsoudi, S. Corradini, and V. Batista. Recent advances in surface guided radiation therapy. *Radiation Oncology*, 15(1):187, 2020. doi:10.1186/s13014-020-01629-w. (Cited on page 24)

H. Fujita, D.-Y. Tsai, T. Itoh, K. Doi, J. Morishita, K. Ueda, and A. Ohtsuka. A simple method for determining the modulation transfer function in digital radiography. *IEEE Transactions on medical imaging*, 11(1):34–39, 1992. doi:10.1109/42.126908. (Cited on pages 59, 84, 85, 86, and 90)

T. Gehrke. *Helium-beam radiography with a fully pixelated silicon detection system*. PhD thesis, Heidelberg University, 2018. URL `https://katalog.ub.uni-heidelberg.de/titel/68291548`. (Cited on pages 34, 36, and 119)

T. Gehrke, L. Burigo, G. Aricó, S. Berke, J. Jakůbek, D. Tureček, T. Tessonnier, A. Mairani, and M. Martišíková. Energy deposition measurements of single 1H, 4He and 12C ions of therapeutic energies in a silicon pixel detector. *Journal of Instrumentation*, 12(04):P04025, 2017. doi:10.1088/1748-0221/12/04/P04025. (Cited on pages 33, 36, 37, 38, and 57)

T. Gehrke, C. Amato, S. Berke, and M. Martišíková. Theoretical and experimental comparison of proton and helium-beam radiography using silicon pixel detectors. *Physics in Medicine & Biology*, 63(3):035037, 2018a. doi:10.1088/1361-6560/aaa60f. (Cited on pages 27, 28, 31, 34, 35, 38, 39, 55, 56, 57, 84, 93, 113, 114, and 119)

T. Gehrke, R. Gallas, O. Jäkel, and M. Martišíková. Proof of principle of helium-beam radiography using silicon pixel detectors for energy deposition measurement, identification, and tracking of single ions. *Medical physics*, 45(2):817–829, 2018b. doi:10.1002/mp.12723. (Cited on pages 3, 28, 32, 37, and 114)

M. Geurts. 1D, 2D, or 3D gamma computation in MATLAB, July 2024. URL `https://doi.org/10.5281/zenodo.12735618`. (Cited on pages 54 and 77)

L. Ghesquiere-Dierickx, A. Schlechter, R. Félix-Bautista, T. Gehrke, G. Echner, L. Kelleter, and M. Martišíková. Investigation of suitable detection angles for carbon-ion radiotherapy monitoring in depth by means of secondary-ion tracking. *Frontiers in Oncology*, 11:780221, 2021. doi:10.3389/fonc.2021.780221. (Cited on page 25)

C. Gianoli, M. Göppel, S. Meyer, P. Palaniappan, M. Rädler, F. Kamp, C. Belka, M. Riboldi, and K. Parodi. Patient-specific CT calibration based on ion radiography for different detector configurations in 1H, 4He and 12C ion pencil beam scanning. *Physics in Medicine & Biology*, 65(24):245014, 2020. doi:10.1088/1361-6560/aba319. (Cited on pages 26 and 124)

C. Gianoli, J. Bortfeldt, and R. Schulte. Ion imaging in particle therapy. In *Imaging in Particle Therapy: Current practice and future trends*, pages 6–1. IOP Publishing Bristol, UK, 2024. doi:10.1088/978-0-7503-5117-1ch6. (Cited on pages 2, 3, and 27)

C. Graeff, U. Weber, C. Schuy, N. Saito, L. Volz, P. Piersimoni, J. Seco, and M. Kraemer. [OA027] Helium as a range probe in carbon ion therapy. *Physica Medica: European Journal of Medical Physics*, 52:11, 2018. doi:https://doi.org/10.1016/j.ejmp.2018.06.099. (Cited on pages 26 and 124)

C. Graeff, L. Volz, and M. Durante. Emerging technologies for cancer therapy using accelerated particles. *Progress in particle and nuclear physics*, 131:104046, 2023. doi:10.1016/j.ppnp.2023.104046. (Cited on page 119)

C. Granja, J. Jakůbek, S. Polansky, V. Zach, P. Krist, D. Chvatil, J. Stursa, M. Sommer, O. Ploc, S. Kodaira, et al. Resolving power of pixel detector Timepix for wide-range electron, proton and ion detection. *Nuclear Instruments and Methods in Physics Research Section A: Accelerators, Spectrometers, Detectors and Associated Equipment*, 908:60–71, 2018. doi:10.1016/j.nima.2018.08.014. (Cited on pages 19 and 32)

C. Grau, M. Durante, D. Georg, J. A. Langendijk, and D. C. Weber. Particle therapy in europe. *Molecular oncology*, 14(7):1492–1499, 2020. doi:10.1002/1878-0261.12677. Licensed under CC BY 4.0. (Cited on pages 12 and 132)

T. W. Griffin. Fast neutron radiation therapy. *Critical reviews in oncology/hematology*, 13(1):17–31, 1992. doi:10.1016/1040-8428(92)90014-H. (Cited on page 1)

D. E. Groom, N. V. Mokhov, and S. I. Striganov. Muon stopping power and range tables 10 MeV-100 TeV. *Atomic Data and Nuclear Data Tables*, 78(2):183–356, 2001. doi:10.1006/adnd.2001.0861. (Cited on page 10)

T. Haberer, W. Becher, D. Schardt, and G. Kraft. Magnetic scanning system for heavy ion therapy. *Nuclear Instruments and Methods in Physics Research Section A: Accelerators, Spectrometers, Detectors and Associated Equipment*, 330(1-2):296–305, 1993. doi:10.1016/0168-9002(93)91335-K. (Cited on page 20)

T. Haberer, J. Debus, H. Eickhoff, O. Jäkel, D. Schulz-Ertner, and U. Weber. The Heidelberg ion therapy center. *Radiotherapy and Oncology*, 73:S186–S190, 2004. doi:10.1016/S0167-8140(04)80046-X. (Cited on page 30)

A. Haghighat. *Monte Carlo methods for particle transport*. Crc Press, 2020. doi:10.1201/9780429198397. (Cited on page 17)

C. W. Hall. *Laws and models: science, engineering, and technology*. CRC Press, 2018. doi:10.1201/9781315219585. (Cited on page 13)

A. Hammi, S. König, D. C. Weber, B. Poppe, and A. J. Lomax. Patient positioning verification for proton therapy using proton radiography. *Physics in Medicine & Biology*, 63(24):245009, 2018. doi:10.1088/1361-6560/aadf79. (Cited on pages 2 and 26)

J. J. Hardt, A. A. Pryanichnikov, N. Homolka, E. A. DeJongh, D. F. DeJongh, R. Cristoforetti, O. Jäkel, J. Seco, and N. Wahl. The potential of mixed carbon–helium beams for online treatment verification: a simulation and treatment planning study. *Physics in Medicine & Biology*, 69(12):125028, 2024. doi:10.1088/1361-6560/ad46db. (Cited on pages 26 and 124)

B. Hartmann, P. Soukup, C. Granja, J. Jakůbek, S. Pospíšil, O. Jäkel, and M. Martišíková. Distortion of the per-pixel signal in the Timepix detector observed in high energy carbon ion beams. *Journal of Instrumentation*, 9(09):P09006, 2014. doi:10.1088/1748-0221/9/09/P09006. (Cited on page 32)

B. Hartmann, C. Granja, J. Jakůbek, T. Gehrke, R. Gallas, S. Pospíšil, O. Jäkel, and M. Martišíková. A novel method for fragmentation studies in particle therapy: principles of ion identification. *International Journal of Particle Therapy*, 3(4):439–449, 2017. doi:10.14338/IJPT-15-00003.1. (Cited on pages 37 and 114)

W. F. Hartsell, C. B. Simone II, D. Godes, J. Maggiore, M. P. Mehta, S. J. Frank, J. M. Metz, and J. I. Choi. Temporal evolution and diagnostic diversification of patients receiving proton therapy in the united states: A ten-year trend analysis (2012 to 2021) from the national association for proton therapy. *International Journal of Radiation Oncology* Biology* Physics*, 119(4):1069–1077, 2024. doi:10.1016/j.ijrobp.2023.12.041. (Cited on page 19)

Y. Hayakawa, J. Tada, N. Arai, K. Hosono, M. Sato, T. Wagai, H. Tsuji, and H. Tsujii. Acoustic pulse generated in a patient during treatment by pulsed proton radiation beam. *Radiation Oncology Investigations*, 3(1):42–45, 1995. doi:10.1002/roi.2970030107. (Cited on page 25)

M. Hermle. Evaluating ion path reconstruction methods for ion-beam radiography based on Monte Carlo simulations, 2025. (Cited on pages 7, 57, and 111)

M. Herrick, S. Penfold, A. Santos, and K. Hickson. A systematic review of volumetric image guidance in proton therapy. *Physical and Engineering Sciences in Medicine*, 46(3):963–975, 2023. doi:10.1007/s13246-023-01301-z. (Cited on page 107)

S. Hickling, L. Xiang, K. C. Jones, K. Parodi, W. Assmann, S. Avery, M. Hobson, and I. El Naqa. Ionizing radiation-induced acoustics for radiotherapy and diagnostic radiology applications. *Medical physics*, 45(7):e707–e721, 2018. doi:10.1002/mp.12929. (Cited on page 25)

V. L. Highland. Some practical remarks on multiple scattering. *Nuclear Instruments and Methods*, 129(2):497–499, 1975. doi:10.1016/0029-554X(75)90743-0. (Cited on page 15)

M. Hoheisel. Review of medical imaging with emphasis on x-ray detectors. *Nuclear Instruments and Methods in Physics Research Section A: Accelerators, Spectrometers, Detectors and Associated Equipment*, 563(1):215–224, 2006. doi:10.1016/j.nima.2006.01.123. (Cited on page 64)

V. Ivanchenko and L. Pandola. The Monte Carlo method and its application to heavily charged particle therapy. In *Monte Carlo in Heavy Charged Particle Therapy*, pages 1–13. CRC Press, 2024. doi:10.1201/9781003023920-1. (Cited on page 17)

D. F. Jackson and D. J. Hawkes. X-ray attenuation coefficients of elements and mixtures. *Physics Reports*, 70(3):169–233, 1981. doi:10.1016/0370-1573(81)90014-4. (Cited on page 22)

D. A. Jaffray, D. G. Drake, M. Moreau, A. A. Martinez, and J. W. Wong. A radiographic and tomographic imaging system integrated into a medical linear accelerator for localization of bone and soft-tissue targets. *International Journal of Radiation Oncology* Biology* Physics*, 45(3):773–789, 1999. doi:10.1016/S0360-3016(99)00118-2. (Cited on page 24)

J. Jakůbek. Semiconductor pixel detectors and their applications in life sciences. *Journal of Instrumentation*, 4(03):P03013, 2009. doi:10.1088/1748-0221/4/03/P03013. (Cited on page 19)

J. Jakůbek. Precise energy calibration of pixel detector working in time-over-threshold mode. *Nuclear Instruments and Methods in Physics Research Section A: Accelerators, Spectrometers, Detectors and Associated Equipment*, 633:S262–S266, 2011. doi:10.1016/j.nima.2010.06.183. (Cited on pages 33 and 35)

J. Jakůbek, C. Granja, O. Jäkel, M. Martišíková, and S. Pospíšil. Detection and track visualization of primary and secondary radiation in hadron therapy beams with the pixel detector Timepix. In *IEEE Nuclear Science Symposium & Medical Imaging Conference*, pages 1967–1969. IEEE, 2010. doi:10.1109/NSSMIC.2010.5874118. (Cited on page 19)

H.-S. Jans, A. Syme, S. Rathee, and B. Fallone. 3D interfractional patient position verification using 2D-3D registration of orthogonal images. *Medical physics*, 33(5): 1420–1439, 2006. doi:10.1118/1.2192907. (Cited on page 24)

R. P. Johnson. Meeting the detector challenges for pre-clinical proton and ion computed tomography. *Physics in Medicine & Biology*, 69(11):11TR02, 2024. doi:10.1088/1361-6560/ad42fc. (Cited on pages 3 and 119)

M. C. Joiner and S. M. Bentzen. Fractionation: the linear-quadratic approach. In *Basic clinical radiobiology*, pages 99–111. CRC press, 2018. doi:10.1201/9781003278337. (Cited on page 20)

Y. Jongen, M. Abs, A. Blondin, W. Kleeven, S. Zaremba, D. Vandeplassche, V. Aleksandrov, S. Gursky, O. Karamyshev, G. Karamysheva, et al. Compact superconducting cyclotron C400 for hadron therapy. *Nuclear Instruments and Methods in Physics Research Section A: Accelerators, Spectrometers, Detectors and Associated Equipment*, 624(1):47–53, 2010. doi:10.1016/j.nima.2010.09.028. (Cited on page 119)

P. Karvelis and oyvindlr. daviolinplot - beautiful violin and raincloud plots: v3.2.4, July 2024. URL `https://doi.org/10.5281/zenodo.12749045`. (Cited on pages 54 and 77)

L. Kelleter, L. Marek, G. Echner, P. Ochoa-Parra, M. Winter, S. Harrabi, J. Jakůbek, O. Jäkel, J. Debus, and M. Martišíková. An in-vivo treatment monitoring system for ion-beam radiotherapy based on 28 Timepix3 detectors. *Scientific reports*, 14(1): 15452, 2024. doi:10.1038/s41598-024-66266-9. (Cited on page 25)

F. Khellaf, N. Krah, J. M. Létang, and S. Rit. Projection deconvolution for proton CT using the spatially variant path uncertainty. *IEEE Transactions on Radiation and Plasma Medical Sciences*, 6(8):847–858, 2022. doi:10.1109/TRPMS.2022.3167334. (Cited on pages 55, 56, and 113)

C. Knobloch, M. Metzner, F. Kehrein, C. Schömers, S. Scheloske, S. Brons, R. Hermann, A. Peters, O. Jäkel, M. Martišíková, and T. Gehrke. Experimental helium-beam radiography with a high-energy beam: Water-equivalent thickness calibration and first image-quality results. *Medical Physics*, 49(8):5347–5362, 2022. doi:10.1002/mp.15795. (Cited on pages 3, 34, 35, 36, 44, 68, 101, 104, 118, and 119)

A.-C. Knopf and A. Lomax. In vivo proton range verification: a review. *Physics in Medicine & Biology*, 58(15):R131, 2013. doi:10.1088/0031-9155/58/15/R131. (Cited on page 25)

A. M. Koehler. Proton radiography. *Science*, 160(3825):303–304, 1968. doi:10.1126/science.160.3825.303. (Cited on page 2)

N. Krah, L. De Marzi, A. Patriarca, G. Pittá, and I. Rinaldi. Proton radiography with a commercial range telescope detector using dedicated post processing methods. *Physics in Medicine & Biology*, 63(20):205016, 2018. doi:10.1088/1361-6560/aae043. (Cited on page 102)

N. Krah, V. Patera, S. Rit, A. Schiavi, and I. Rinaldi. Regularised patient-specific stopping power calibration for proton therapy planning based on proton radiographic images. *Physics in Medicine & Biology*, 64(6):065008, 2019. doi:10.1088/1361-6560/ab03db. (Cited on page 26)

N. Krah, D. Dauvergne, J. M. Létang, S. Rit, and E. Testa. Relative stopping power resolution in time-of-flight proton CT. *Physics in Medicine & Biology*, 67(16):165004, 2022. doi:10.1088/1361-6560/ac7191. (Cited on page 27)

V. Kraus, M. Holik, J. Jakůbek, M. Kroupa, P. Soukup, and Z. Vykydal. FITPix—fast interface for Timepix pixel detectors. *Journal of Instrumentation*, 6(01):C01079, 2011. doi:10.1088/1748-0221/6/01/C01079. (Cited on page 33)

M. Kroupa, S. Hoang, N. Stoffle, P. Soukup, J. Jakůbek, and L. Pinsky. Energy resolution and power consumption of Timepix detector for different detector settings and saturation of front-end electronics. *Journal of Instrumentation*, 9(05):C05008, 2014. doi:10.1088/1748-0221/9/05/C05008. (Cited on page 32)

G. Landry and C.-h. Hua. Current state and future applications of radiological image guidance for particle therapy. *Medical Physics*, 45(11):e1086–e1095, 2018. doi:10.1002/mp.12744. (Cited on page 24)

S. A. Lane, J. M. Slater, and G. Y. Yang. Image-guided proton therapy: A comprehensive review. *Cancers*, 15(9):2555, 2023. doi:10.3390/cancers15092555. (Cited on page 2)

S. G. Laskar, S. Sinha, R. Krishnatry, C. Grau, M. Mehta, and J. P. Agarwal. Access to radiation therapy: from local to global and equality to equity. *JCO global oncology*, 8:e2100358, 2022. doi:10.1200/GO.21.00358. (Cited on page 1)

J. E. Leeman, P. B. Romesser, Y. Zhou, S. McBride, N. Riaz, E. Sherman, M. A. Cohen, O. Cahlon, and N. Lee. Proton therapy for head and neck cancer: expanding the therapeutic window. *The lancet oncology*, 18(5):e254–e265, 2017. doi:10.1016/S1470-2045(17)30179-1. (Cited on pages 1 and 20)

S. Lehrack, W. Assmann, D. Bertrand, S. Henrotin, J. Herault, V. Heymans, F. Vander Stappen, P. G. Thirolf, M. Vidal, J. Van de Walle, et al. Submillimeter ionoacoustic range determination for protons in water at a clinical synchrocyclotron. *Physics in Medicine & Biology*, 62(17):L20, 2017. doi:10.1088/1361-6560/aa81f8. (Cited on page 25)

B. Li, H. Lee, X. Duan, C. Shen, L. Zhou, X. Jia, and M. Yang. Comprehensive analysis of proton range uncertainties related to stopping-power-ratio estimation using dual-energy CT imaging. *Physics in Medicine & Biology*, 62(17):7056, 2017. doi:10.1088/1361-6560/aa7dc9. (Cited on page 24)

D. Liljequist. On the sampling of step length in Monte Carlo simulation of trajectories with very small mean free path. *Radiation Physics and Chemistry*, 81(11):1703–1709, 2012. doi:10.1016/j.radphyschem.2012.06.058. (Cited on page 17)

X. Llopart, R. Ballabriga, M. Campbell, L. Tlustos, and W. Wong. Timepix, a 65k programmable pixel readout chip for arrival time, energy and/or photon counting measurements. *Nucl. Instrum. Methods Phys. Res.*, 581:485–485, 2007. doi:10.1016/j.nima.2007.08.079. (Cited on pages 31, 32, and 34)

X. Llopart, J. Alozy, R. Ballabriga, M. Campbell, R. Casanova, V. Gromov, E. Heijne, T. Poikela, E. Santin, V. Sriskaran, et al. Timepix4, a large area pixel detector readout chip which can be tiled on 4 sides providing sub-200 ps timestamp binning. *Journal of Instrumentation*, 17(01):C01044, 2022. doi:10.1088/1748-0221/17/01/C01044. (Cited on pages 40, 118, and 119)

A. J. Lomax. Myths and realities of range uncertainty. *The British journal of radiology*, 93(1107):20190582, 2020. doi:10.1259/bjr.20190582. (Cited on page 2)

F. K. Longarino, A. Kowalewski, T. Tessonnier, S. Mein, B. Ackermann, J. Debus, A. Mairani, and W. Stiller. Potential of a second-generation dual-layer spectral CT for dose calculation in particle therapy treatment planning. *Frontiers in oncology*, 12: 853495, 2022. doi:10.3389/fonc.2022.853495. (Cited on page 109)

F. K. Longarino, C. Herpel, T. Tessonnier, S. Mein, B. Ackermann, J. Debus, F. S. Schwindling, W. Stiller, and A. Mairani. Dual-energy CT-based stopping power prediction for dental materials in particle therapy. *Journal of Applied Clinical Medical Physics*, 24(8):e13977, 2023. doi:https://doi.org/10.1002/acm2.13977. (Cited on page 51)

D. A. Low, W. B. Harms, S. Mutic, and J. A. Purdy. A technique for the quantitative evaluation of dose distributions. *Medical physics*, 25(5):656–661, 1998. doi:10.1118/1.598248. (Cited on page 54)

G. R. Lynch and O. I. Dahl. Approximations to multiple coulomb scattering. *Nuclear Instruments and Methods in Physics Research Section B: Beam Interactions with Materials and Atoms*, 58(1):6–10, 1991. doi:10.1016/0168-583X(91)95671-Y. (Cited on page 15)

A. Mairani, S. Mein, E. Blakely, J. Debus, M. Durante, A. Ferrari, H. Fuchs, D. Georg, D. R. Grosshans, F. Guan, et al. Roadmap: helium ion therapy. *Physics in Medicine & Biology*, 67(15):15TR02, 2022. doi:10.1088/1361-6560/ac65d3. (Cited on pages 28 and 119)

M. Martišíková, T. Gehrke, S. Berke, G. Aricó, and O. Jäkel. Helium ion beam imaging for image guided ion radiotherapy. *Radiation oncology*, 13:1–17, 2018. doi:10.1186/s13014-018-1046-6. (Cited on pages 26, 28, and 32)

D. Mattes, D. R. Haynor, H. Vesselle, T. K. Lewellyn, and W. Eubank. Nonrigid multimodality image registration. In *Medical imaging 2001: image processing*, volume 4322, pages 1609–1620. Spie, 2001. doi:10.1117/12.431046. (Cited on page 53)

D. Mazzucconi, S. Agosteo, M. Ferrarini, L. Fontana, V. Lante, M. Pullia, and S. Savazzi. Mixed particle beam for simultaneous treatment and online range verification in carbon ion therapy: Proof-of-concept study. *Medical physics*, 45(11):5234–5243, 2018. doi:10.1002/mp.13219. (Cited on pages 26 and 124)

C. H. McCollough, S. Leng, L. Yu, and J. G. Fletcher. Dual-and multi-energy CT: principles, technical approaches, and clinical applications. *Radiology*, 276(3):637–653, 2015. doi:10.1148/radiol.2015142631. (Cited on page 23)

T. Mee, N. F. Kirkby, N. N. Defourny, K. J. Kirkby, and N. G. Burnet. The use of radiotherapy, surgery and chemotherapy in the curative treatment of cancer: results from the FORTY (Favourable Outcomes from RadioTherapY) project. *The British journal of radiology*, 96(1152):20230334, 2023. doi:10.1259/bjr.20230334. (Cited on page 1)

A. Meijers, C. Seller Oria, J. Free, J. A. Langendijk, A. C. Knopf, and S. Both. First report on an in vivo range probing quality control procedure for scanned proton beam therapy in head and neck cancer patients. *Medical Physics*, 48(3):1372–1380, 2021. doi:10.1002/mp.14713. (Cited on pages 3 and 27)

N. Metropolis and S. Ulam. The monte carlo method. *Journal of the American statistical association*, 44(247):335–341, 1949. doi:10.1080/01621459.1949.10483310. (Cited on page 17)

M. Metzner. Helium-beam radiography using thin silicon pixel detectors: Establishment of calibration curves and quantitative imaging of an anthropomorphic head phantom. Master's thesis, Heidelberg University, 2022. (Cited on pages 5, 40, 44, 46, 101, 103, and 104)

M. Metzner, A. Schlechter, C. Amato, O. Jäkel, M. Martišíková, and T. Gehrke. Helium-beam radiography for precise cancer irradiation: Impact of scatter rejection on image quality. In *2024 IEEE Nuclear Science Symposium (NSS), Medical Imaging Conference (MIC) and Room Temperature Semiconductor Detector Conference (RTSD)*, pages 1–2. IEEE, 2024a. doi:10.1109/NSS/MIC/RTSD57108.2024.10656569. (Cited on pages 5, 41, 64, and 97)

M. Metzner, D. Zhevachevska, A. Schlechter, F. Kehrein, J. Schlecker, C. Murillo, S. Brons, O. Jäkel, M. Martišíková, and T. Gehrke. Energy painting: helium-beam radiography with thin detectors and multiple beam energies. *Physics in Medicine & Biology*, 69(5):055002, 2024b. doi:10.1088/1361-6560/ad247e. © Institute of Physics and Engineering in Medicine. All rights reserved. (Cited on pages 5, 32, 34, 35, 36, 37, 38, 40, 41, 42, 43, 45, 46, 47, 48, 49, 68, 69, 70, 72, 74, 100, 104, 132, 133, and 134)

M. Metzner, F. K. Longarino, B. Ackermann, A. Schlechter, M. Saphörster, Y. Xu, J. Schlecker, P. Wohlfahrt, C. Richter, S. Brons, J. Debus, O. Jäkel, M. Martišíková, and T. Gehrke. Accuracy of a helium-beam radiography system based on thin pixel detectors for an anthropomorphic head phantom. *Medical physics*, 52(6):4757–4768, 2025a. doi:10.1002/mp.17786. Licensed under CC BY 4.0. (Cited on pages 6, 50, 51, 52, 53, 54, 75, 76, 77, 81, 106, and 133)

M. Metzner, A. Schlechter, D. Zhevachevska, P. Schlegel, O. Jäkel, M. Martišíková, and T. Gehrke. 2.5D Imaging: Obtaining depth information from 2D helium-beam radiographs. *Physics in Medicine & Biology*, Advance online publication, 2025b. doi:10.1088/1361-6560/ae02de. Licensed under CC BY 4.0. (Cited on pages 6, 54, 55, 56, 57, 59, 60, 61, 62, 82, 88, 90, 91, 92, 93, 94, 113, 114, 115, 116, 128, 129, 133, and 134)

S. Meyer, F. Kamp, T. Tessonnier, A. Mairani, C. Belka, D. J. Carlson, C. Gianoli, and K. Parodi. Dosimetric accuracy and radiobiological implications of ion computed tomography for proton therapy treatment planning. *Physics in Medicine & Biology*, 64(12):125008, 2019. doi:10.1088/1361-6560/ab0fdf. (Cited on pages 2 and 26)

C. Miller, B. Altoos, E. A. DeJongh, M. Pankuch, D. F. DeJongh, V. Rykalin, C. E. Ordoñez, N. T. Karonis, J. R. Winans, G. Coutrakon, et al. Reconstructed and real proton radiographs for image-guidance in proton beam therapy. *Journal of radiation oncology*, 8(1):97–101, 2019. doi:10.1007/s13566-019-00376-0. (Cited on pages 2 and 26)

G. Molière. Theorie der Streuung schneller geladener Teilchen ii Mehrfach-und Vielfachstreuung. *Zeitschrift für Naturforschung A*, 3(2):78–97, 1948. doi:10.1515/zna-1948-0203. (Cited on page 15)

S. Navas, C. Amsler, T. Gutsche, C. Hanhart, J. Hernández-Rey, C. Lourenço, A. Masoni, M. Mikhasenko, R. Mitchell, C. Patrignani, et al. Review of particle physics. *Physical Review D*, 110(3):030001, 2024. doi:10.1103/PhysRevD.110.030001. Chapter 34. Passage of Particles Through Matter. (Cited on pages 10, 11, and 15)

D. Ondreka and U. Weinrich. The Heidelberg Ion Therapy (HIT) accelerator coming into operation. *European Physical Society Accelerator Group, Proceedings of EPAC*, pages 23–27, 2008. doi:10.1063/1.3120065. (Cited on page 29)

H. Paganetti. Range uncertainties in proton therapy and the role of Monte Carlo simulations. *Physics in Medicine & Biology*, 57(11):R99, 2012. doi:10.1088/0031-9155/57/11/R99. (Cited on pages 2, 21, 23, 108, and 110)

H. Paganetti, B. S. Athar, M. Moteabbed, J. A. Adams, U. Schneider, and T. I. Yock. Assessment of radiation-induced second cancer risks in proton therapy and IMRT for organs inside the primary radiation field. *Physics in Medicine & Biology*, 57(19): 6047, 2012. doi:10.1088/0031-9155/57/19/6047. (Cited on pages 1 and 20)

P. Palaniappan, S. Meyer, F. Kamp, C. Belka, M. Riboldi, K. Parodi, and C. Gianoli. A 2D-3D Deformable image registration framework for proton radiographies in adaptive radiation therapy. In *2019 IEEE Nuclear Science Symposium and Medical Imaging Conference (NSS/MIC)*, pages 1–3. IEEE, 2019. doi:10.1109/NSS/MIC42101.2019.9059647. (Cited on page 26)

P. Palaniappan, S. Meyer, F. Kamp, C. Belka, M. Riboldi, K. Parodi, and C. Gianoli. Deformable image registration of the treatment planning ct with proton radiographies in perspective of adaptive proton therapy. *Physics in Medicine & Biology*, 66(4): 045008, 2021. doi:10.1088/1361-6560/ab8fc3. (Cited on page 26)

Å. Palm and K.-A. Johansson. A review of the impact of photon and proton external beam radiotherapy treatment modalities on the dose distribution in field and out-of-field; implications for the long-term morbidity of cancer survivors. *Acta oncologica*, 46(4):462–473, 2007. doi:10.1080/02841860701218626. (Cited on pages 1 and 20)

K. Parodi. Imaging for ion beam therapy: current trends and future perspectives. *Health and Technology*, 14(5):895–901, 2024. doi:10.1007/s12553-024-00853-8. (Cited on pages 2, 14, 24, and 25)

K. Parodi and W. Assmann. Ionoacoustics. In *Modern Applications of 3D/4D Ultrasound Imaging in Radiotherapy*, pages 11–1. IOP Publishing Bristol, UK, 2021. doi:10.1088/978-0-7503-2552-3ch11. (Cited on page 25)

N. Peters, P. Wohlfahrt, C. V. Dahlgren, L. de Marzi, M. Ellerbrock, F. Fracchiolla, J. Free, C. Gomà, J. Góra, M. F. Jensen, et al. Experimental assessment of inter-centre variation in stopping-power and range prediction in particle therapy. *Radiotherapy and Oncology*, 163:7–13, 2021. doi:10.1016/j.radonc.2021.07.019. (Cited on page 107)

N. Peters, P. Wohlfahrt, C. Hofmann, C. Möhler, S. Menkel, M. Tschiche, M. Krause, E. G. Troost, W. Enghardt, and C. Richter. Reduction of clinical safety margins in proton therapy enabled by the clinical implementation of dual-energy CT for direct stopping-power prediction. *Radiotherapy and Oncology*, 166:71–78, 2022. doi:10.1016/j.radonc.2021.11.002. (Cited on page 24)

N. Peters, V. T. Taasti, B. Ackermann, A. Bolsi, C. V. Dahlgren, M. Ellerbrock, F. Fracchiolla, C. Gomà, J. Góra, P. C. Lopes, et al. Consensus guide on CT-based prediction of stopping-power ratio using a Hounsfield look-up table for proton therapy. *Radiotherapy and Oncology*, 184:109675, 2023. doi:10.1016/j.radonc.2023.109675. (Cited on pages 23 and 107)

T. Poikela, J. Plosila, T. Westerlund, M. Campbell, M. De Gaspari, X. Llopart, V. Gromov, R. Kluit, M. Van Beuzekom, F. Zappon, et al. Timepix3: a 65k channel hybrid pixel readout chip with simultaneous ToA/ToT and sparse readout. *Journal of instrumentation*, 9(05):C05013, 2014. doi:10.1088/1748-0221/9/05/C05013. (Cited on pages 40 and 118)

G. Poludniowski, N. M. Allinson, and P. M. Evans. Proton radiography and tomography with application to proton therapy. *The British journal of radiology*, 88(1053): 20150134, 2015. doi:10.1259/bjr.20150134. (Cited on pages 2, 3, and 27)

PTCOG. Particle Therapy Patient Statistics (per end of 2023, provisional). https://www.ptcog.site/images/Statistics/Patientstatistics-provisional_Dec2023.pdf, 2023. Accessed: 2025-04-15. (Cited on pages 19 and 29)

PTCOG. Facilities under construction. https://ptcog.online/facilities-under-construction/, 2025a. Accessed: 2025-08-22. (Cited on page 19)

PTCOG. Facilities in clinical operation. https://ptcog.online/facilities-in-clinical-operation/, 2025b. Accessed: 2025-08-22. (Cited on pages 19 and 28)

PTCOG. Particle therapy facilities in a planning stage. https://ptcog.online/facilities-in-planning-stage/, 2025c. Accessed: 2025-08-22. (Cited on page 19)

A. Qubala, A. Schwahofer, S. Jersemann, S. Eskandarian, S. Harrabi, P. Naumann, M. Winter, M. Ellerbrock, J. Shafee, S. Abtehi, et al. Optimizing the patient positioning workflow of patients with pelvis, limb, and chest/spine tumors at an ion-beam gantry based on optical surface guidance. *Advances in Radiation Oncology*, 8(2): 101105, 2023. doi:10.1016/j.adro.2022.101105. (Cited on page 24)

D. Raeside. Monte Carlo principles and applications. *Physics in Medicine & Biology*, 21(2):181, 1976. doi:10.1088/0031-9155/21/2/001. (Cited on page 17)

S. E. Reichenbach, S. K. Park, and R. Narayanswamy. Characterizing digital image acquisition devices. *Optical Engineering*, 30(2):170–177, 1991. doi:10.1117/12.55783. (Cited on pages 59, 84, 85, 86, and 90)

S. Rit, G. Dedes, N. Freud, D. Sarrut, and J. M. Létang. Filtered backprojection proton CT reconstruction along most likely paths. *Medical physics*, 40(3):031103, 2013. doi:10.1118/1.4789589. (Cited on pages 39, 55, and 56)

J. Romero, J. Osborne, F. Brady, W. Caskey, D. Cebra, M. Partlan, B. Kusko, R. King, I. Mirshad, H. Kubo, et al. Patient positioning for protontherapy using a proton range telescope. *Nuclear Instruments and Methods in Physics Research Section A: Accelerators, Spectrometers, Detectors and Associated Equipment*, 356(2-3):558–565, 1995. (Cited on page 26)

E. Rosenblatt, E. Fidarova, E. H. Zubizarreta, M. B. Barton, G. W. Jones, W. J. Mackillop, L. Cordero, J. Yarney, G. Lim, J. V. Gan, et al. Radiotherapy utilization in developing countries: An IAEA study. *Radiotherapy and oncology*, 128(3):400–405, 2018. doi:10.1016/j.radonc.2018.05.014. (Cited on page 1)

R. Rutherford, B. Pullan, and I. Isherwood. Measurement of effective atomic number and electron density using an EMI scanner. *Neuroradiology*, 11(1):15–21, 1976. doi:10.1007/BF00327253. (Cited on page 22)

C. Sarosiek, E. A. DeJongh, G. Coutrakon, D. F. DeJongh, K. L. Duffin, N. T. Karonis, C. E. Ordoñez, M. Pankuch, V. Rykalin, J. R. Winans, et al. Analysis of characteristics of images acquired with a prototype clinical proton radiography system. *Medical physics*, 48(5):2271–2278, 2021. doi:10.1002/mp.14801. (Cited on pages 26, 43, 101, 102, and 115)

W. Saunders, J. Castro, G. Chen, J. Collier, S. Zink, S. Pitluck, T. Phillips, D. Char, P. Gutin, G. Gauger, et al. Helium-ion radiation therapy at the Lawrence Berkeley Laboratory: Recent results of a Northern California Oncology Group clinical trial. *Radiation research*, 104(2s):S227–S234, 1985. doi:10.2307/3576652. (Cited on page 119)

A. Savitzky and M. J. Golay. Smoothing and differentiation of data by simplified least squares procedures. *Analytical chemistry*, 36(8):1627–1639, 1964. doi:10.1021/ac60214a047. (Cited on pages 59, 62, and 84)

D. Schardt, T. Elsässer, and D. Schulz-Ertner. Heavy-ion tumor therapy: Physical and radiobiological benefits. *Reviews of modern physics*, 82(1):383, 2010. doi:10.1103/RevModPhys.82.383. (Cited on pages 1, 10, and 20)

J. F. Schlag, A. C. Sanderson, C. P. Neuman, and F. C. Wimberly. *Implementation of automatic focusing algorithms for a computer vision system with camera control*. Carnegie-Mellon University, The Robotics Institute, 1983. (Cited on pages 62, 91, 92, and 94)

A. Schlechter. 2.5D imaging: accessing 3D information of a 2D ion-beam radiograph. Master's thesis, Heidelberg University, 2024. (Cited on pages 6, 55, 57, 59, 60, 61, and 62)

W. Schlegel, C. P. Karger, and O. Jäkel. *Medizinische Physik: Grundlagen–Bildgebung–Therapie–Technik*. Springer-Verlag, 2018. doi:10.1007/978-3-662-54801-1. (Cited on pages 12, 13, and 16)

U. Schneider and E. Pedroni. Multiple coulomb scattering and spatial resolution in proton radiography. *Medical physics*, 21(11):1657–1663, 1994. doi:10.1118/1.597212. (Cited on pages 39, 55, and 56)

U. Schneider and E. Pedroni. Proton radiography as a tool for quality control in proton therapy. *Medical physics*, 22(4):353–363, 1995. doi:10.1118/1.597470. (Cited on pages 2 and 26)

U. Schneider, E. Pedroni, and A. Lomax. The calibration of CT Hounsfield units for radiotherapy treatment planning. *Physics in Medicine & Biology*, 41(1):111, 1996. doi:10.1088/0031-9155/41/1/009. (Cited on pages 22, 23, and 51)

U. Schneider, P. Pemler, J. Besserer, E. Pedroni, A. Lomax, and B. Kaser-Hotz. Patient specific optimization of the relation between CT-Hounsfield units and proton stopping power with proton radiography. *Medical physics*, 32(1):195–199, 2005. doi:10.1118/1.1833041. (Cited on pages 26 and 124)

W. Schneider, T. Bortfeld, and W. Schlegel. Correlation between CT numbers and tissue parameters needed for Monte Carlo simulations of clinical dose distributions. *Physics in Medicine & Biology*, 45(2):459–478, 2000. doi:10.1088/0031-9155/45/2/314. (Cited on page 51)

C. Schömers, S. Brons, R. Cee, A. Peters, S. Scheloske, and T. Haberer. Beam properties beyond the therapeutic range at HIT. *Published online*, 2022. doi:10.18429/JACoW-IPAC2023-THPM064. (Cited on page 118)

R. Schulte, V. Bashkirov, T. Li, Z. Liang, K. Mueller, J. Heimann, L. R. Johnson, B. Keeney, H.-W. Sadrozinski, A. Seiden, et al. Conceptual design of a proton computed tomography system for applications in proton radiation therapy. *IEEE Transactions on Nuclear Science*, 51(3):866–872, 2004. doi:10.1109/TNS.2004.829392. (Cited on page 119)

R. Schulte, S. Penfold, J. Tafas, and K. Schubert. A maximum likelihood proton path formalism for application in proton computed tomography. *Medical physics*, 35(11): 4849–4856, 2008. doi:10.1118/1.2986139. (Cited on pages 38, 41, 99, 100, and 134)

R. W. Schulte, V. Bashkirov, M. C. Loss Klock, T. Li, A. J. Wroe, I. Evseev, D. C. Williams, and T. Satogata. Density resolution of proton computed tomography. *Medical physics*, 32(4):1035–1046, 2005. doi:10.1118/1.1884906. (Cited on pages 2 and 26)

D. Schulz-Ertner and H. Tsujii. Particle radiation therapy using proton and heavier ion beams. *Journal of clinical oncology*, 25(8):953–964, 2007. doi:10.1200/JCO.2006.09.7816. (Cited on pages 1 and 20)

L. Schweins, R. Kirchgässner, P. Ochoa-Parra, M. Winter, S. Harrabi, A. Mairani, O. Jäkel, J. Debus, M. Martišíková, and L. Kelleter. Detection of an internal density change in an anthropomorphic head phantom via tracking of charged nuclear fragments in carbon-ion radiotherapy. *Medical Physics*, 52(4):2399–2411, 2025. doi:10.1002/mp.17590. (Cited on pages 60, 61, and 93)

J. Seco, M. Oumano, N. Depauw, M. F. Dias, R. P. Teixeira, and M. F. Spadea. Characterizing the modulation transfer function (MTF) of proton/carbon radiography using Monte Carlo simulations. *Medical physics*, 40(9):091717, 2013. doi:10.1118/1.4819816. (Cited on page 113)

S. M. Seltzer and M. J. Berger. Evaluation of the collision stopping power of elements and compounds for electrons and positrons. *The International Journal of Applied Radiation and Isotopes*, 33(11):1189–1218, 1982. doi:10.1016/0020-708X(82)90244-7. (Cited on pages 22 and 23)

R. Serber. Nuclear reactions at high energies. *Physical Review*, 72(11):1114, 1947. doi:10.1103/PhysRev.72.1114. (Cited on page 16)

H. Spieler. *Semiconductor detector systems*, volume 12. Oxford university press, 2005. ISBN 978-0198527848. (Cited on pages 18 and 19)

E. Steiner, M. Stock, B. Kostresevic, A. Ableitinger, U. Jelen, H. Prokesch, A. Santiago, P. Trnková, A. Wolf, A. Wittig, et al. Imaging dose assessment for IGRT in particle beam therapy. *Radiotherapy and Oncology*, 109(3):409–413, 2013. doi:10.1016/j.radonc.2013.09.007. (Cited on page 107)

V. Taasti, C. Bäumer, C. Dahlgren, A. Deisher, M. Ellerbrock, J. Free, J. Gora, A. Kozera, T. Lomax, L. d. Marzi, et al. Inter-center variability in CT-to-SPR conversion in particle therapy: Survey-based evaluation. *Radiotherapy and Oncology*, 2018. doi:10.1016/j.phro.2018.04.006. (Cited on page 110)

J. Telsemeyer, O. Jäkel, and M. Martišíková. Quantitative carbon ion beam radiography and tomography with a flat-panel detector. *Physics in Medicine & Biology*, 57(23): 7957, 2012. doi:10.1088/0031-9155/57/23/7957. (Cited on pages 43 and 101)

J. Telsemeyer, B. Ackermann, S. Ecker, O. Jäkel, and M. Martišíková. Experimental verification of ion range calculation in a treatment planning system using a flat-panel detector. *Physics in Medicine & Biology*, 59(14):3737–3747, 2014. doi:10.1088/0031-9155/59/14/3737. (Cited on page 51)

J. M. Tenenbaum. *Accommodation in computer vision*. Stanford University, 1971. (Cited on pages 62, 91, 92, and 94)

T. Tessonnier, S. Ecker, J. Besuglow, J. Naumann, S. Mein, F. K. Longarino, M. Ellerbrock, B. Ackermann, M. Winter, S. Brons, et al. Commissioning of helium ion therapy and the first patient treatment with active beam delivery. *International Journal of Radiation Oncology* Biology* Physics*, 116(4):935–948, 2023. doi:10.1016/j.ijrobp.2023.01.015. (Cited on pages 1, 29, and 119)

H. Thames. Early fractionation methods and the origins of the NSD concept. *Acta Oncologica*, 27(2):89–103, 1988. doi:10.3109/02841868809090329. (Cited on page 20)

D. J. Thomas. ICRU report 85: fundamental quantities and units for ionizing radiation. *Radiation Protection Dosimetry*, 150(4):550–552, 05 2012. ISSN 0144-8420. doi:10.1093/rpd/ncs077. (Cited on page 9)

L. Townsend and J. Wilson. Energy-dependent parameterization of heavy-ion absorption cross sections. *Radiation research*, pages 283–287, 1986. doi:10.2307/3576735. (Cited on page 16)

R. Tripathi, F. A. Cucinotta, and J. W. Wilson. Accurate universal parameterization of absorption cross sections. *Nuclear Instruments and Methods in Physics Research Section B: Beam Interactions with Materials and Atoms*, 117(4):347–349, 1996. doi:10.1016/0168-583X(96)00331-X. (Cited on page 16)

J. G. Trump, K. Wright, W. Evans, J. Anson, H. Hare, J. Fromer, G. Jacque, and K. Horne. High energy electrons for the treatment of extensive superficial malignant lesions. *The American journal of roentgenology, radium therapy, and nuclear medicine*, 69(4): 623–629, 1953. (Cited on page 1)

C. Tschalär and H. Maccabee. Energy-straggling measurements of heavy charged particles in thick absorbers. *Physical Review B*, 1(7):2863, 1970. doi:10.1103/PhysRevB.1.2863. (Cited on page 15)

J. W. Tukey. *Exploratory data analysis*, volume 2. Springer, 1977. ISBN 978-0201076165. (Cited on pages 62 and 128)

D. Tureček, T. Holy, J. Jakůbek, S. Pospíšil, and Z. Vykydal. Pixelman: a multi-platform data acquisition and processing software package for Medipix2, Timepix and Medipix3 detectors. *Journal of Instrumentation*, 6(01):C01046, 2011. doi:10.1088/1748-0221/6/01/C01046. (Cited on page 33)

F. Ulrich-Pur, T. Bergauer, A. Burker, A. Hirtl, C. Irmler, S. Kaser, F. Pitters, and S. Rit. Feasibility study of a proton CT system based on 4D-tracking and residual energy determination via time-of-flight. *Physics in Medicine & Biology*, 67(9):095005, 2022. doi:10.1088/1361-6560/ac628b. (Cited on page 27)

F. Ulrich-Pur, T. Bergauer, T. Galatyuk, A. Hirtl, M. Kausel, V. Kedych, M. Kis, Y. Kozymka, W. Krüger, S. Linev, et al. First experimental time-of-flight-based proton radiography using low gain avalanche diodes. *Physics in Medicine & Biology*, 69(7):075031, 2024. doi:10.1088/1361-6560/ad3326. (Cited on page 27)

T. A. Van De Water, A. J. Lomax, H. P. Bijl, M. E. De Jong, C. Schilstra, E. B. Hug, and J. A. Langendijk. Potential benefits of scanned intensity-modulated proton therapy versus advanced photon therapy with regard to sparing of the salivary glands in oropharyngeal cancer. *International Journal of Radiation Oncology - Biology - Physics*, 79(4):1216–1224, 2011. doi:10.1016/j.ijrobp.2010.05.012. (Cited on pages 1 and 20)

W. Van Elmpt, G. Landry, M. Das, and F. Verhaegen. Dual energy CT in radiotherapy: current applications and future outlook. *Radiotherapy and Oncology*, 119(1):137–144, 2016. doi:10.1016/j.radonc.2016.02.026. (Cited on page 109)

V. Vlachoudis. Flair: A powerful but user friendly graphical interface for FLUKA. *International Conference on Mathematics, Computational Methods & Reactor Physics 2009*, pages 790–800, 2009. (Cited on page 57)

L. Volz, P. Piersimoni, V. A. Bashkirov, S. Brons, C.-A. Collins-Fekete, R. P. Johnson, R. W. Schulte, and J. Seco. The impact of secondary fragments on the image quality of helium ion imaging. *Physics in Medicine & Biology*, 63(19):195016, 2018. doi:10.1088/1361-6560/aadf25. (Cited on page 28)

L. Volz, P. Piersimoni, R. P. Johnson, V. A. Bashkirov, R. W. Schulte, and J. Seco. Improving single-event proton CT by removing nuclear interaction events within the energy/range detector. *Physics in Medicine & Biology*, 64(15):15NT01, 2019. doi:10.1088/1361-6560/ab2671. (Cited on page 28)

L. Volz, C.-A. Collins-Fekete, J. R. Sølie, and J. Seco. Theoretical considerations on the spatial resolution limit of single-event particle radiography. *Biomedical Physics & Engineering Express*, 6(5):055002, 2020a. doi:10.1088/2057-1976/ab9c3f. (Cited on pages 39, 55, 56, and 93)

L. Volz, L. Kelleter, S. Brons, L. Burigo, C. Graeff, N. Niebuhr, R. Radogna, S. Scheloske, C. Schömers, S. Jolly, et al. Experimental exploration of a mixed helium/carbon beam for online treatment monitoring in carbon ion beam therapy. *Physics in Medicine & Biology*, 65(5):055002, 2020b. doi:10.1088/1361-6560/ab6e52. (Cited on pages 26 and 124)

L. Volz, C. Collins-Fekete, E. Bär, S. Brons, C. Graeff, R. Johnson, A. Runz, C. Sarosiek, R. Schulte, and J. Seco. The accuracy of helium ion CT based particle therapy range prediction: an experimental study comparing different particle and x-ray CT modalities. *Physics in Medicine & Biology*, 66(23):235010, 2021. doi:10.1088/1361-6560/ac33ec. (Cited on pages 25 and 108)

L. Volz, C. Graeff, M. Durante, and C.-A. Collins-Fekete. Focus stacking single-event particle radiography for high spatial resolution images and 3D feature localization. *Physics in Medicine & Biology*, 69(2):024001, 2024. doi:10.1088/1361-6560/ad131a. (Cited on pages 55, 56, 57, 59, 61, 62, 82, 111, 113, 115, 128, 129, and 134)

R. R. Wilson. Radiological use of fast protons. *Radiology*, 47(5):487–491, 1946. doi:10.1148/47.5.487. (Cited on pages 1, 9, and 13)

T. Winkelmann, R. Cee, T. Haberer, B. Naas, A. Peters, and J. Schreiner. Status Report at the Heidelberg Ion-Beam Therapy (HIT) Ion Sources and the Testbench. In *Proc. 21st Int. Workshop on ECR Ion Sources (ECRIS'14)*, pages 49–51, 2014. URL `https://accelconf.web.cern.ch/ECRIS2014/papers/mopph004.pdf`. Licensed under CC BY 3.0. (Cited on pages 30 and 132)

P. Wohlfahrt and C. Richter. Status and innovations in pre-treatment CT imaging for proton therapy. *The British journal of radiology*, 93(1107):20190590, 2020. doi:10.1259/bjr.20190590. (Cited on pages 2, 22, 23, 24, and 109)

P. Wohlfahrt, C. Möhler, C. Richter, and S. Greilich. Evaluation of stopping-power prediction by dual-and single-energy computed tomography in an anthropomorphic ground-truth phantom. *International Journal of Radiation Oncology* Biology* Physics*, 100 (1):244–253, 2018. doi:10.1016/j.ijrobp.2017.09.025. (Cited on pages 50, 54, 75, 77, 107, 108, and 110)

A. J. Wroe, D. A. Bush, R. W. Schulte, and J. D. Slater. Clinical immobilization techniques for proton therapy. *Technology in Cancer Research & Treatment*, 14(1): 71–79, 2015. doi:10.7785/tcrt.2012.500398. (Cited on page 24)

M. Yang, X. R. Zhu, P. C. Park, U. Titt, R. Mohan, G. Virshup, J. E. Clayton, and L. Dong. Comprehensive analysis of proton range uncertainties related to patient stopping-power-ratio estimation using the stoichiometric calibration. *Physics in Medicine & Biology*, 57(13):4095, 2012. doi:10.1088/0031-9155/57/13/4095. (Cited on page 23)

R. Zhang, P. J. Taddei, M. M. Fitzek, and W. D. Newhauser. Water equivalent thickness values of materials used in beams of protons, helium, carbon and iron ions. *Physics in Medicine & Biology*, 55(9):2481, 2010. doi:10.1088/0031-9155/55/9/004. (Cited on page 13)

H Acknowledgment

I first want to thank Prof. Dr. Oliver Jäkel for welcoming me as a PhD student in the department, for serving as a TAC member and as referee of the thesis. Thank you for taking the time to always proofread my contributions and for supporting me with my travels and any other matter. Despite a busy schedule, you have always been really approachable. Thank you for always appreciating my accomplishments and for valuing them sincerely.

I want to thank the formal supervisors of my thesis who enabled a PhD at the physics faculty: Prof. Dr. Dr. Debus, who supervised the first half of my PhD, and Prof. Dr. Mark Ladd, who took over in the second half and served as independent referee and TAC member. Thanks to both for always being supportive. Furthermore, I would like to thank Jun. Prof. Dr. Loredana Gastaldo for serving as my second co-advisor at the physics faculty. It was always a pleasure to show you my progress, discuss my research with you and feel your support. After our meetings, I always felt uplifted and encouraged. Also, thanks to Prof. Dr. Julia Bauer for being my TAC member and for providing valuable feedback on my research, but also on me as a researcher and academic. I really appreciate that you also saw me as a person and gave my TACs a bit of a personal touch.

I would like to express my sincere gratitude to Dr. Mária Martišíková, my group leader, who supported me throughout my whole PhD journey. Your expertise and insightful feedback have been instrumental in shaping me as a researcher. I am really grateful for your feedback on my project and the valuable discussions. Thanks for your guidance with the publication processes, for your clever strategic decisions, and your extensive proofreading. Thanks for always making time when I needed your support or just wanted to share my thoughts or feelings.

I am deeply grateful for the guidance provided by Dr. Tim Gehrke. Words cannot express how much you have supported me during my PhD. Your enthusiasm for the helium-beam radiography project was invaluable and motivated me incredibly. Thanks for your scientific integrity, your thoroughness and responsibility. Thanks for your positivity, empathy, sensitivity and understanding. You were always there when I needed you. Thanks for providing such a great research environment for me which enabled me to grow and thrive.

Thanks to all members of the group E0406. Thanks for the lively, productive and precious discussions, the motivating lunch and coffee breaks and your support of my work. Thanks for offering a space to discuss my thoughts, my perspectives and also my struggles.

Special thanks to everyone who helped with proofreading my thesis, especially to Tim, Maria, Pamela, Rebekka, Philipp, Julian and Friderike.

Thanks to all co-authors on my papers and the people who are acknowledged in these publications. I met so many supportive, curious and helpful people who supported me. Special thanks to the colleagues at HIT, especially Stephan Brons, Friderike Longarino and Benjamin Ackermann.

I would like to thank the DKFZ International PhD program and the Heidelberger Institut für Radioonkologie (HIRO) who funded this PhD project. Additionally, I would like to thank the HGSFP (Heidelberg Graduate School For Physics) for their friendly and timely support with any matter. Also, thanks to Verein zur Förderung der Tumortherapie mit schweren Ionen e.V., the HGSFP, the DAAD, PIANOFORTE and 2024 IEEE MIC for supporting me financially with my travels.

I want to express my thanks to my close friends and family in my mother tongue.

Ein besonderes Danke an Julian Schlecker, der sich immer mit Hingabe meinen Problemen gewidmet hat, egal ob theoretischer/statistischer oder persönlicher Natur, und sich immer unglaublich viel Zeit dafür genommen hat. Danke für das emotionale Councelling, deine Geduld und dein Verständnis. Danke, dass du mich schon so lange auf meinem Weg begleitest und mich einfach so gut kennst.
Auch ein großes Danke an meine Mitbewohner, die aus der WG ein Zuhause gemacht haben. Danke für die unzähligen WG-Abende, euer Interesse, euren emotionalen Support und das gemeinsame Lachen. Danke für die Ablenkung, wenn ich sie gebraucht habe!

Danke an meine Familie. Danke, dass ihr euch so für meine Arbeit interessiert, dass ihr sogar anderen erklären könnt, an was ich eigentlich arbeite. Danke, dass ihr geduldig mit mir wart, wenn ich stressigere Phasen hatte und immer eine "Höhle" geboten habt, damit ich Homeoffice in eurer Gesellschaft machen oder einfach mal von Allem abschalten konnte. Danke für das Zuhören und eure Beratung, die unglaublich reflektierten Perspektiven auf mein Leben und für die gemeinsamen Träume und Macken.

Danke an meinen Partner Marco. Danke für dein Verständnis für mich als Person, aber auch deine wertvollen Sichtweisen. Danke, dass du meine Gesundheit im Blick hattest. Danke für deine Unterstützung, dein Interesse, deine Begeisterungsfähigkeit und deine Geduld. Danke für die Ermutigung, das Zuhören, den Rückhalt und das Auffangen.